

AD-A138 836

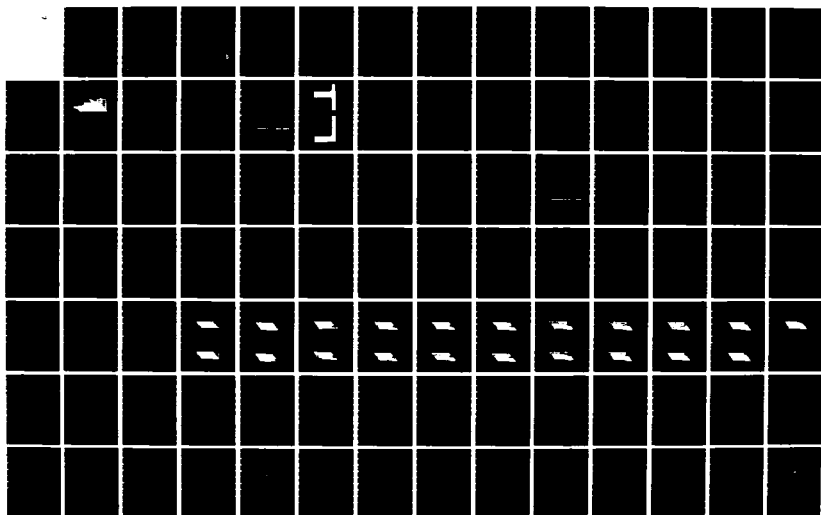
NUCLEAR AND NON-NUCLEAR AIRBLAST EFFECTS(U) SCIENCE  
APPLICATIONS INC MCLEAN VA M FRV 14 FEB 84 SAI-84/1529  
N00014-82-C-2229

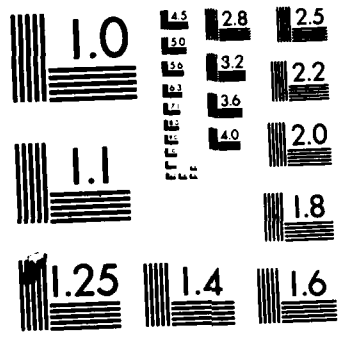
1/2

UNCLASSIFIED

F/G 19/4

NL





MICROCOPY RESOLUTION TEST CHART  
NATIONAL BUREAU OF STANDARDS-1963-A

(H)

12

ADAI 38836

NUCLEAR AND NON-NUCLEAR  
AIRBLAST EFFECTS

FINAL REPORT NO. SAI-84/1519

MARK FRY

February 14, 1984

DTIC  
ELECTE  
MAR 9 1984  
A

DTIC FILE COPY

SCIENCE APPLICATIONS, INC.

NUCLEAR AND NON-NUCLEAR AIRBLAST EFFECTS

Mark Fry

FINAL REPORT NO. SAI-84/1529

Submitted to

Laboratory for Computational Physics  
Naval Research Laboratory  
4555 Overlook Avenue, S.W.  
Washington, D.C. 20375

Prepared under:

Contract No. N00014-82-C-2229

by

Science Applications, Inc.  
1710 Goodridge Drive  
McLean, Virginia 22102

February 14, 1984



SCIENCE APPLICATIONS, INCORPORATED

1710 Goodridge Drive, McLean, VA 22102 (703) 734-5840

This document has been approved for release and sale; its contents are not to be distributed outside the United States.



TABLE OF CONTENTS

GENERAL DISCUSSION. . . . . 1  
APPENDIX A. . . . . A-1  
APPENDIX B. . . . . B-1  
APPENDIX C. . . . . C-1  
APPENDIX D. . . . . D-1  
APPENDIX E. . . . . E-1

Accession For  
RECEIVED  
DATE  
BY  
A-1

DTIC  
COPY  
RESPECTED

## GENERAL DISCUSSION

Science Applications, Inc. has utilized the family of Flux-Corrected Transport (FCT) algorithms at NRL to model the airblast produced by nuclear and non-nuclear events. The FCT algorithms combine low order numerical integration schemes which are non-dispersive with high order schemes that are non diffusive. The net effect is to significantly improve the solution of flow fields with sharp gradients.

The one-dimensional code can be configured for cylindrical, spherical or planar geometries. This code is primarily used to generate the flow field from spherical high explosive charges. The two-dimensional code is a cartesian or cylindrical code. Both codes use the same FCT algorithm. The three-dimensional code, however, employs a leap frog FCT scheme. It is not as accurate but runs a factor of two faster on a computer.

One and two-dimensional simulations of PBX 9404 were completed and comparisons made with data. Appendix A details the results. A two dimensional calculation approximating an infinite plane of explosions was completed and is reported in Appendix B. The limitations and comparisons of both nuclear and non-nuclear events are outlined in Appendix C. When blast waves occur over dusty surfaces there is significant transport of the dust.

Appendix D reports the results of research into the dust and shock interaction. Finally, an attempt was made to approximate the gas dynamic equations through power series expansions for the case where a planar shock encounters a wedge. Appendix E explains the analysis.

APPENDIX A  
ADAPTATION OF FLUX-CORRECTED TRANSPORT ALGORITHMS  
FOR MODELLING BLAST WAVES



18. Supplementary Notes (Continued)

\*Present address: Science Applications Inc., McLean, VA.

\*\*Present address: JAYCOR, Alexandria, VA.

†Present address: R&D Associates, Marina del Rey, CA.

## ADAPTATION OF FLUX-CORRECTED TRANSPORT ALGORITHMS FOR MODELLING BLAST WAVES

Blast wave phenomena include reactive and two-phase flows associated with the motion of chemical explosion products; the propagation of shocks, rarefaction waves, and contact discontinuities through a nonideal medium (real air, possibly thermally stratified and containing dust and water vapor); and the interaction of the blast waves (including boundary layer effects) with structural surfaces. Flux-Corrected Transport (FCT) represents an accurate and flexible class of methods for solving such nonsteady compressible flow problems (Boris and Book, 1976). Coupled with a nondiffusive adaptive gridding scheme (Book, *et al.*, 1980; Fry, *et al.*, 1981), it enables complex time-dependent shocks to be efficiently "captured."

In models which treat all the physical effects required for blast wave simulation, truncation errors inherent in the underlying finite-difference scheme are exacerbated by nonlinear coupling between the fluid equations and by the greater complexity of the phenomena being simulated. Typical of these errors are the "terraces" which develop under some circumstances on the flanks of sloping profiles when the growth of ripples due to phase errors at short length scales is terminated by the action of the flux limiter. Two approaches are possible toward eliminating them: improving the short-wavelength phase and amplitude properties of the underlying algorithm, and switching on additional diffusion locally. The latter approach folds information about the shape of the profile and the nature of the physical process taking place (e.g., rarefaction) into the switch criterion, thus changing the FCT technique from a "convective equation solver" to a "fluid system solver." In doing this, care must be taken to avoid losing the accuracy, robustness and problem-independence which constitute valuable attributes of FCT algorithms (Book, *et al.*, 1981).

Tests carried out on scalar advection of simple density profiles by a uniform flow field show that terracing does not require either diverging velocities or discontinuities in the profile, but appears typically (for  $v > 0$ ) where the first and second derivatives of density have the same sign (Fig.1). In order to improve the properties of the basic difference scheme, we propose a new algorithm for integrating generalized continuity equations over a timestep  $\delta t$ . Consider the following three-point transport scheme:

$$\tilde{\rho}_j = \rho_j^0 - \eta(\rho_{j+1}^0 - \rho_{j-1}^0) + \kappa(\rho_{j+1}^0 - 2\rho_j^0 + \rho_{j-1}^0);$$

$$\bar{\rho}_j = \tilde{\rho}_j - \theta(\rho_{j+1}^0 - \rho_{j-1}^0) + \lambda(\rho_{j+1}^0 - 2\rho_j^0 + \rho_{j-1}^0);$$

$$\rho_j^n = \bar{\rho}_j - \mu(\phi_{j+1/2} - \phi_{j-1/2}),$$

where

$$\phi_{j+1/2} = \tilde{\rho}_{j+1} - \tilde{\rho}_j.$$

The arrays  $\{\rho_j^o\}$  and  $\{\rho_j^n\}$  are the old and new densities,  $\tilde{\rho}_j$  and  $\bar{\rho}_j$  are temporary intermediate densities, and  $\eta$ ,  $\theta$ ,  $\kappa$ ,  $\lambda$ , and  $\mu$  are velocity-dependent coefficients. Here  $\kappa$  and  $\lambda$  are diffusion coefficients, and  $\mu$  is the antidiffusion coefficient. In the actual algorithm,  $\phi_{j+1/2}^c$  is corrected (hence the name FCT) to a value  $\phi_{j+1/2}^n$  chosen so no extrema in  $\bar{\rho}_j$  can be enhanced or new ones introduced in  $\rho_j^n$ . Previous FCT algorithms had  $\theta = 0$ ; the widely used ETBFCT and related algorithms (Boris, 1976) have in addition  $\kappa = 0$ . If we define  $\rho_j^o$  to be sinusoidal with wave number  $k$  on a mesh with uniform spacing  $\delta x$ , so that  $\rho_j^o = \exp(ij\beta)$  where  $\beta = k\delta x$ , then the new density array satisfies

$$\rho_j^n / \rho_j^o \equiv A = 1 - 2i(\eta + \theta)\sin\beta + 2(\kappa + \lambda)(\cos\beta - 1) - 2\mu(\cos\beta - 1)[1 - 2i\eta\sin\beta + 2\kappa(\cos\beta - 1)].$$

From A we can determine the amplification  $\alpha = A$  and relative phase error  $R = (1/\epsilon\beta)\tan^{-1}(-\text{Im}A/\text{Re}A) - 1$ , where  $\epsilon = v\delta t/\delta x$  is the Courant number.

Expanding in powers of  $\beta$  we find

$$\alpha = 1 + \alpha_2\beta^2 + \alpha_4\beta^4 + \alpha_6\beta^6 + \dots$$

$$R = R_0 + R_2\beta^2 + R_4\beta^4 + R_6\beta^6 + \dots$$

First-order accuracy entails making  $R_0$  vanish, which requires that  $\eta + \theta = \epsilon/2$ . Second-order accuracy ( $\alpha_2 = 0$ ) implies that  $\mu = \kappa + \lambda - \epsilon^2/2$ . Analogously, the "reduced-phase-error" property  $R_2 = 0$  (Boris and Book, 1976) determines  $\mu = (1 - \epsilon^2)/6$ , thus leaving two free parameters. One of these can be used to make  $R_4$  vanish also. The resulting phase error  $R(\beta)$  is small not only as  $\beta \rightarrow 0$ , but also for larger values of  $\beta$ , corresponding to the short wavelengths responsible for terraces (Fig. 2). The remaining parameter  $\eta$  can be chosen to relax the Courant number restriction needed to ensure positivity from  $\epsilon < 1/2$  to  $\epsilon < 1$ . When coded, these changes necessitate a small increase in the operation count of ETBFCT along with a small increase in overhead to precalculate the two new arrays of velocity-dependent transport coefficients. On advection tests, the new algorithm completely eliminated terraces (Fig. 3). When applied to the coupled systems of gas dynamic equations, it produced profiles which closely approximate the Riemann solution of the exploding diaphragm problem (Fig. 4).

The second approach uses a rarefaction flux limiter (RFL) to eliminate numerical ripples in strong rarefaction waves. This approach is physically motivated. Raw anti-diffusive fluxes  $\phi_{j+1/2}$  are limited so that the slope of local flow field profiles decays with time in a rarefaction wave. In effect, additional diffusion is left in the field to maintain monotonicity of local slopes. For multi-material calculations a "contact surface sensor" is needed to detect physical discontinuities and shut off the RFL locally.

In addition we found that some care was required when applying generalized continuity equation solvers to a system of equations. Truncation errors of the various equations can interact, causing undershoots or overshoots in nonconvective quantities such as pressure. We found that it was necessary to monotonize derived quantities (pressure, velocity) before using them in minimal-diffusion transport algorithms.

The above methodology has been applied to a series of test problems initiated by a spherical high-explosive (HE) detonation in air. An ideal Chapman-Jouguet detonation was used to specify the initial conditions; afterburning was neglected. In the absence of reflecting surfaces, spherical symmetry is maintained and the calculation remains one-dimensional. A nonuniform radial grid was used with extremely fine zoning near the shock front. The grid was moved so that the shock remained approximately fixed with respect to the mesh. The original version of the FCT algorithm gave rise to pronounced terraces in the rarefaction region. This would have rendered any two-dimensional calculation involving shock diffraction or nonideal effects dubious. The techniques described here improved the blast wave results considerably. The decrease in phase error reduced terracing dramatically.

Next, a two-dimensional (2D) numerical calculation was performed to simulate one of Carpenter's (1974) height-of-burst experiments which used spherical 8-lb. charges of PBX 9404 at 51.6 cm. The previous fine-zoned 1D calculation was used to initialize the problem. It was mapped onto the 2D grid just prior to the onset of reflection. The solution was then advanced in time, with pressure being calculated from a real-air equation of state and a JWL equation of state for the combustion products. The front of the blast wave was captured in a finely gridded region which moved outward horizontally. Special care was taken to ensure that the grid moved smoothly. The resulting solution, particularly the curve of peak overpressure vs. range, was consistent with Carpenter's experimental data (Fig. 8). Although this calculation represents a reasonable accurate simulation of the double-Mach-stem region, no doubt improvements can and will be made to numerically model such phenomena.

#### References

Book, D., Boris, J., Kuhl, A., Oran, E., Picone, M., and Zalesak, S., Seventh International Conf. on Num. Methods in Fluid Dynamics, Stanford (1980). W. C. Reynolds and R. W. MacCormack, eds. p. 84.

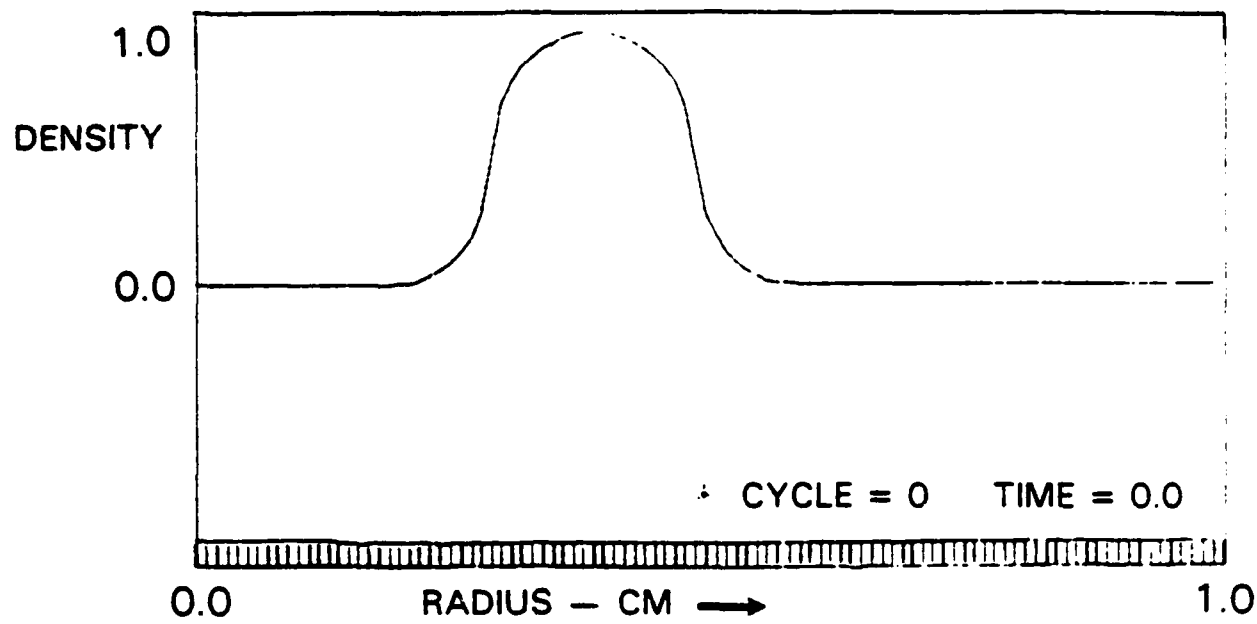
Book, D., Boris, J., and Zalesak, S., in Finite-Difference Techniques for Vectorized Fluid Dynamics Calculations, D. Book, Ed. (Springer-Verlag, New York, 1981).

Boris, J., "Flux-Corrected Transport Modules for Solving Generalized Continuity Equations," NRL Memorandum Report 3237 (1976).

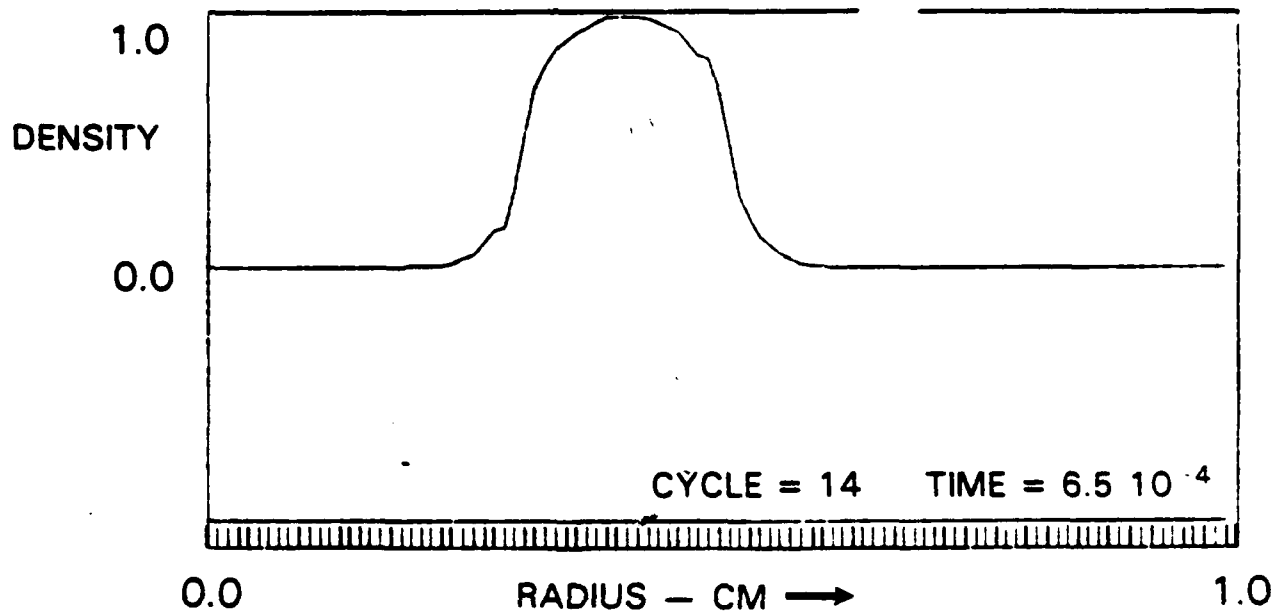
Boris, J.P., and Book, D.L., in Methods in Computational Physics, J. Killeen, Ed., (Academic Press, New York, 1976) Vol. 16, p. 85.

Carpenter, H.J., Proc. Fourth International Symp. on Military Applications of Blast Simulation (1974).

Fry, M., Tittsworth, J., Kuhl, A., Book, D., Boris, J., and Picone, M., "Shock Capturing Using Flux-Corrected Transport Algorithms with Adaptive Gridding," NRL Memorandum Report 4629 (1981).



(a)



(b)

Fig. 1 — Rounded half circle used in passive scalar advection tests (a) initially, and (b) after propagation for 14 cycles using JPBFACT. Note that terraces form even, as here, in the absence of corners in the profile. Tick marks indicate computational zones ( $N = 100$ ).

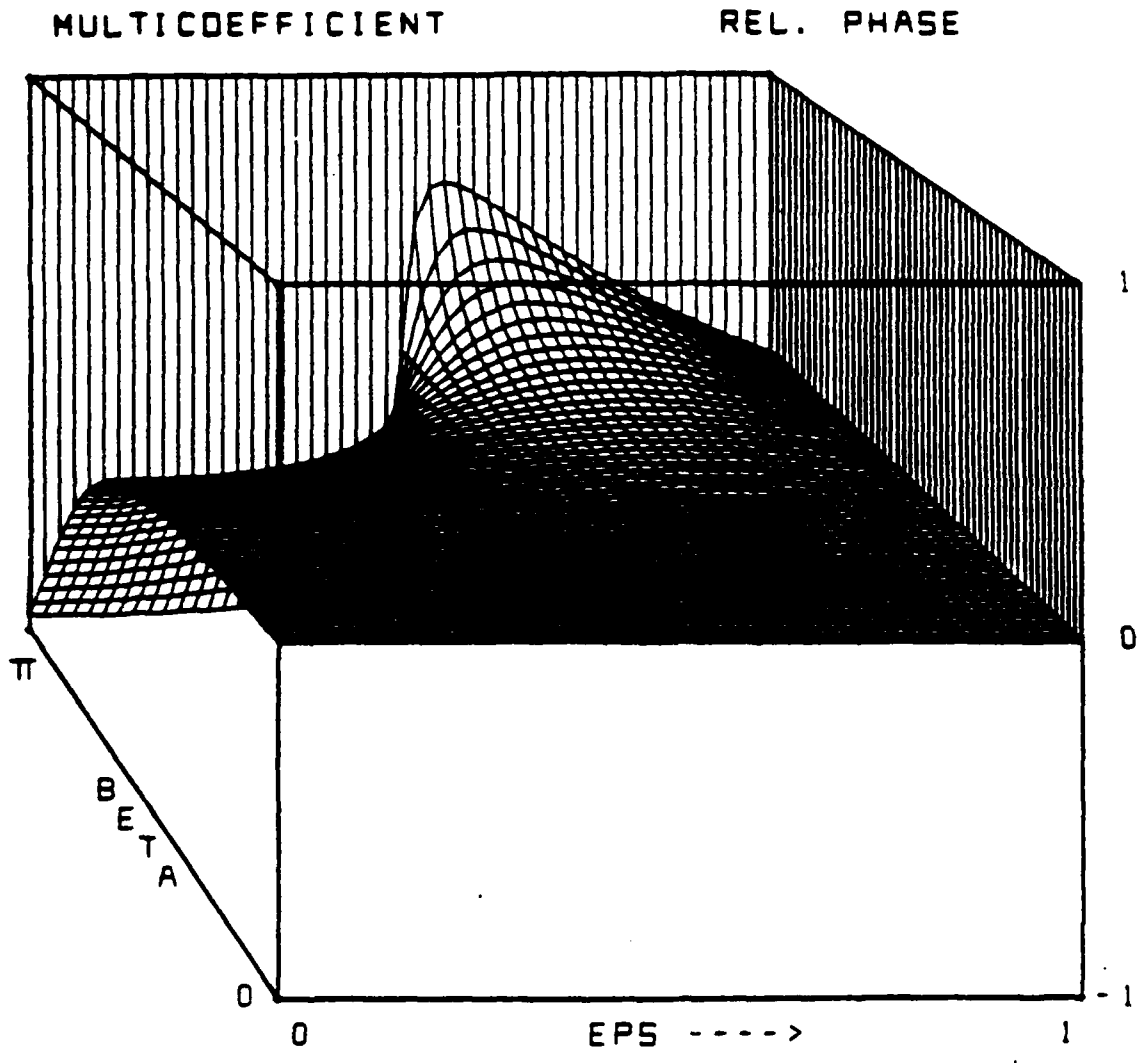


Fig. 2— Contour plot of  $R(\beta, \epsilon)$  for new multicoefficient FCT algorithm. Note  $R \approx 0$  except for  $\beta \geq 3\pi/2$ . The relative phase error vanishes exactly for  $\epsilon = 1/2$  and  $\epsilon = 1$ .

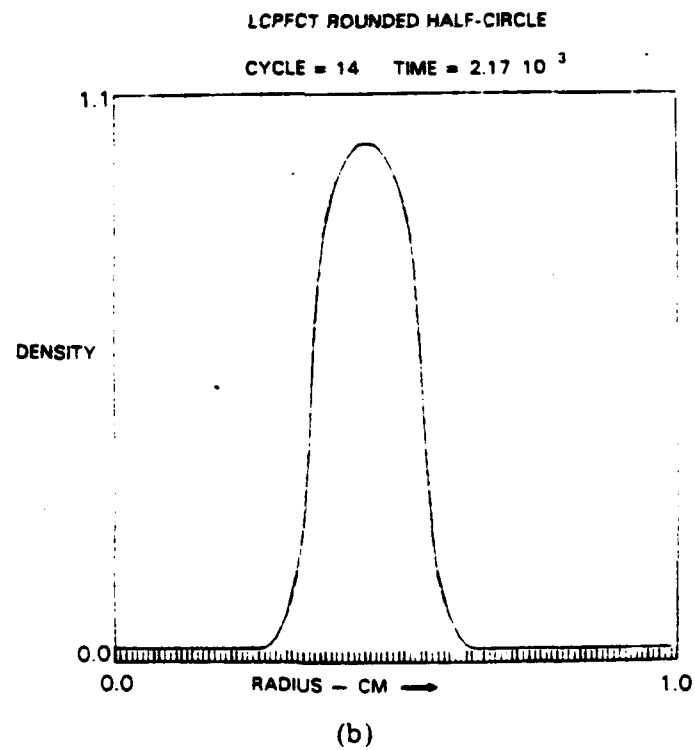
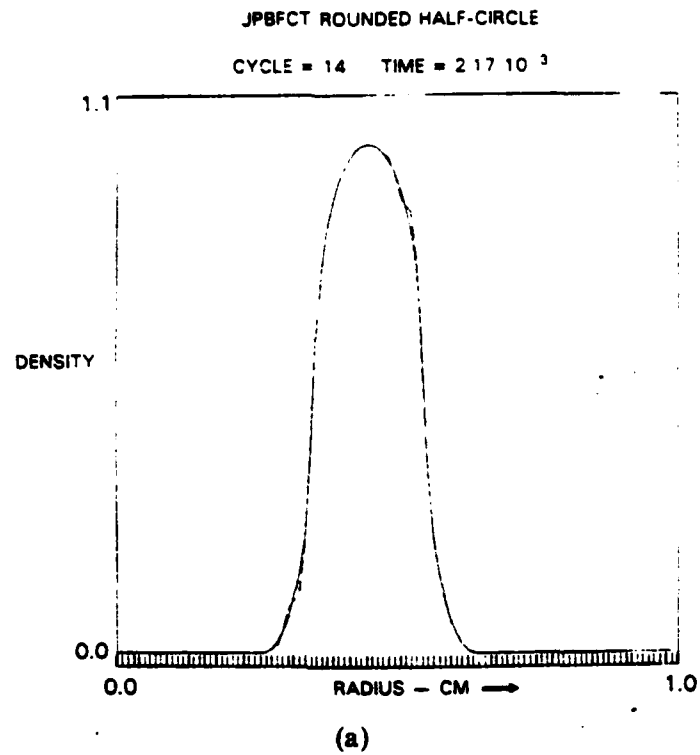
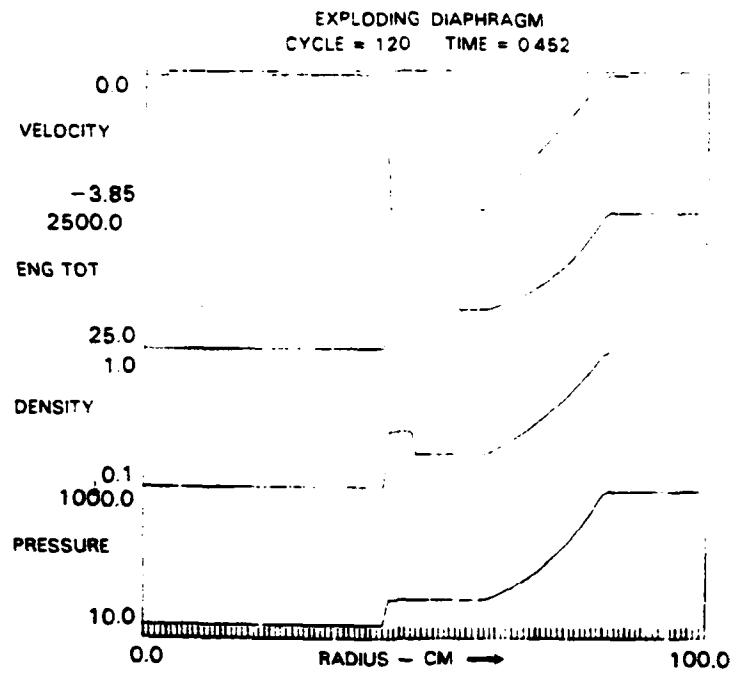
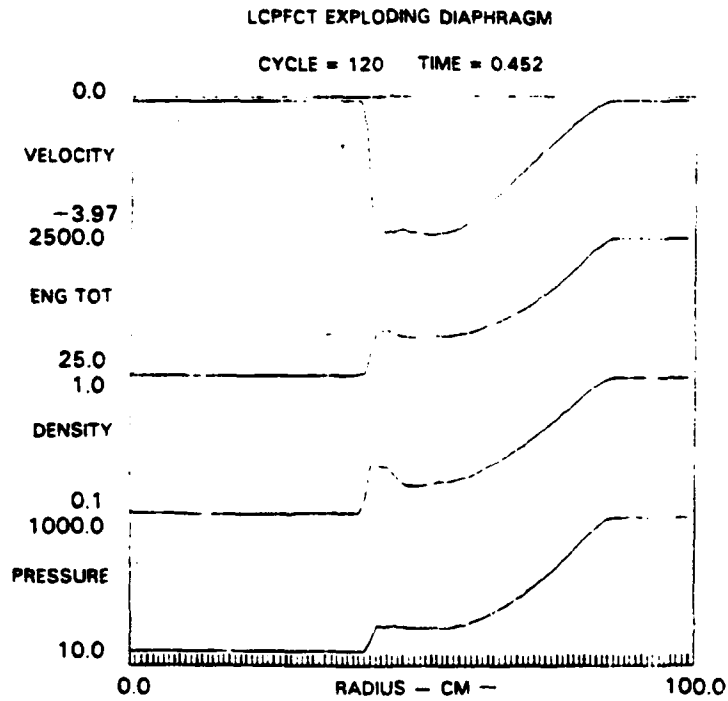


Fig. 3 — (a) Blowup of Fig. 1(a) (dashed line) compared with (b) same profile as computed using new sixth order-phase-accurate FCT algorithm. Solid traces are exact solutions.



(a)



(b)

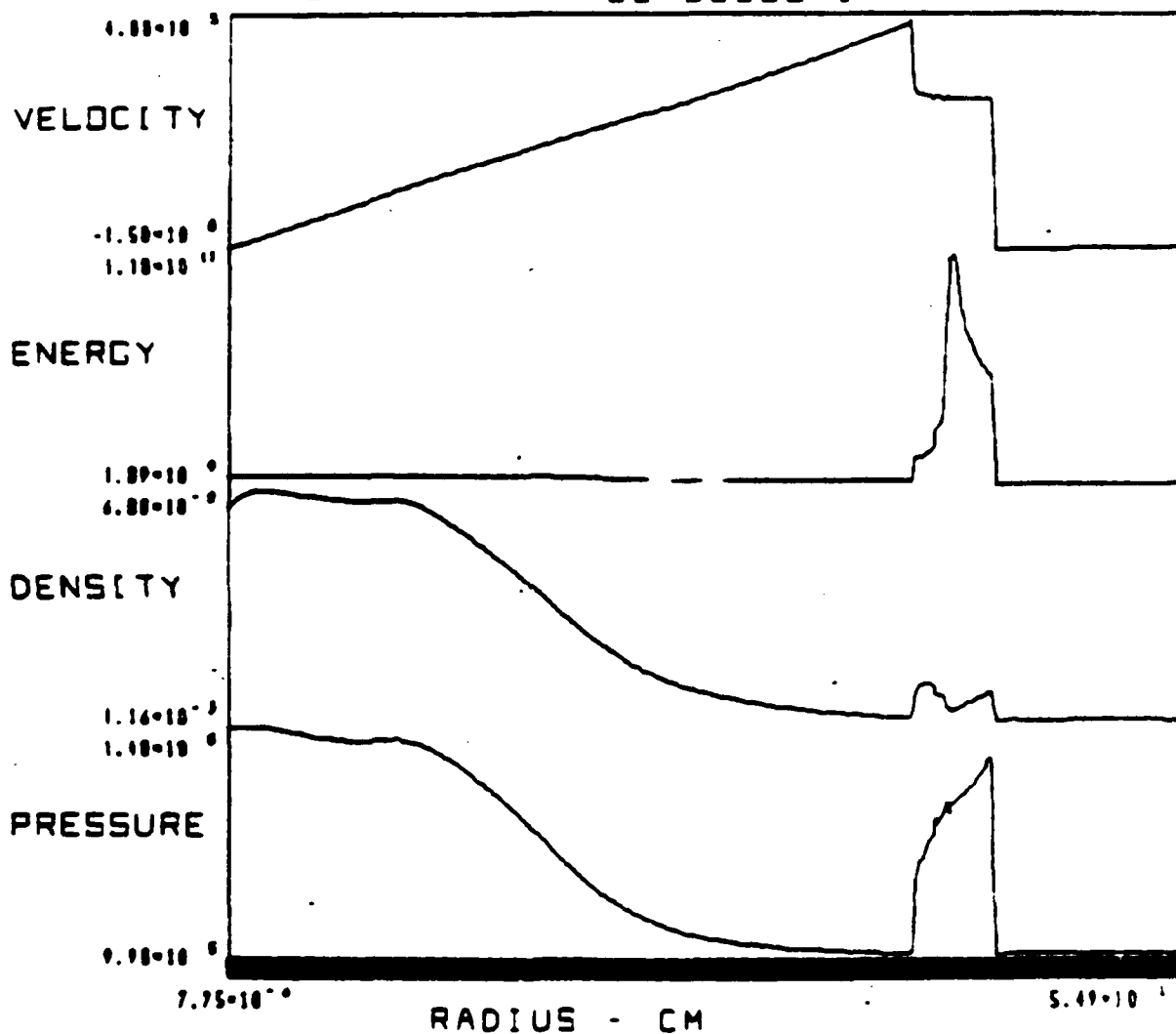
Fig. 4 — (a) Exact and (b) computed solution of exploding diaphragm problem  
(10-to-1 initial density jump, 100-to-1 initial pressure jump)

SHOCK ONE DEE CODE

CYCLE =  $1.00 \cdot 10^3$

TIME =  $6.97 \cdot 10^{-5}$

$5.00 \cdot 10^2$



RADIUS - CM

HE-AIR P-R FIXED GRID

Fig. 5 — One-dimensional solution of expanding HE products and air calculated with the new algorithm using 500 equally spaced zones. Note contact surface separating HE products from air.

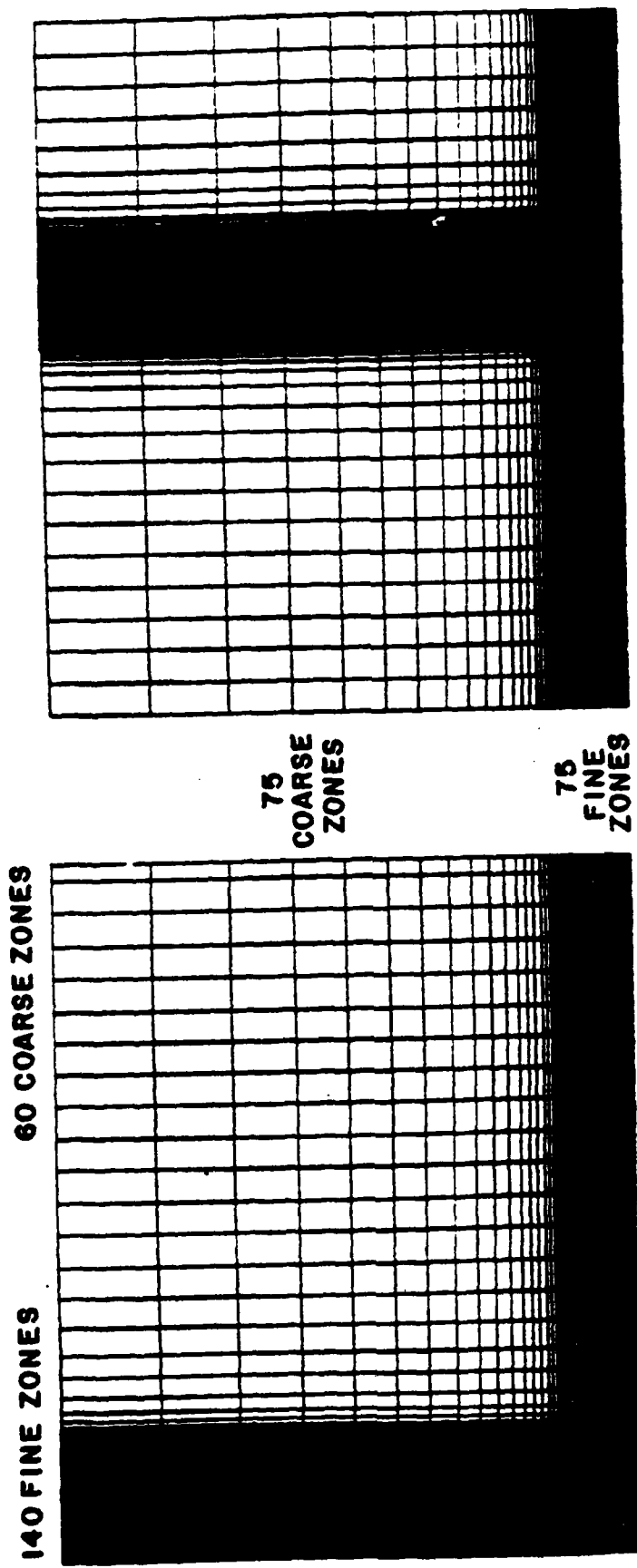


Fig. 6 — Adaptive grid for height-of-burst problem shown (a) initially and (b) at time when transition to Mach reflection occurs

HE - AIR JPBFACT

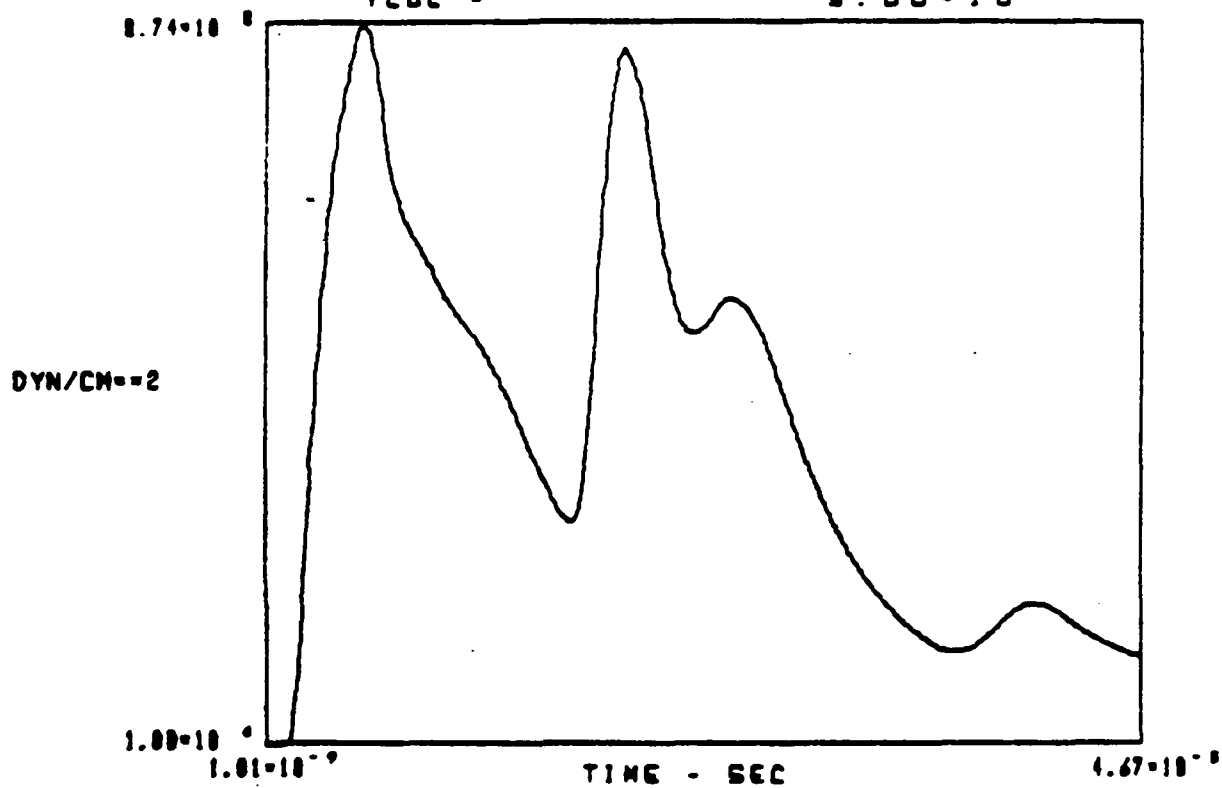
ST = 1.00 = 10<sup>0</sup>

XLOC =

10.00 = 10<sup>-2</sup>

YLDC =

5.00 = 10<sup>-2</sup>



P<sub>MAX</sub> = 8.74 × 10<sup>0</sup>

TIME = 5.21 × 10<sup>-6</sup>

### PRESSURE VS TIME

Fig. 7 — Pressure-time histories directly beneath burst site. Note second peak, associated with interaction between shock reflected from ground and following contact surface.

HE - AIR JPBFACT

ST = 3.60 \* 10<sup>2</sup>

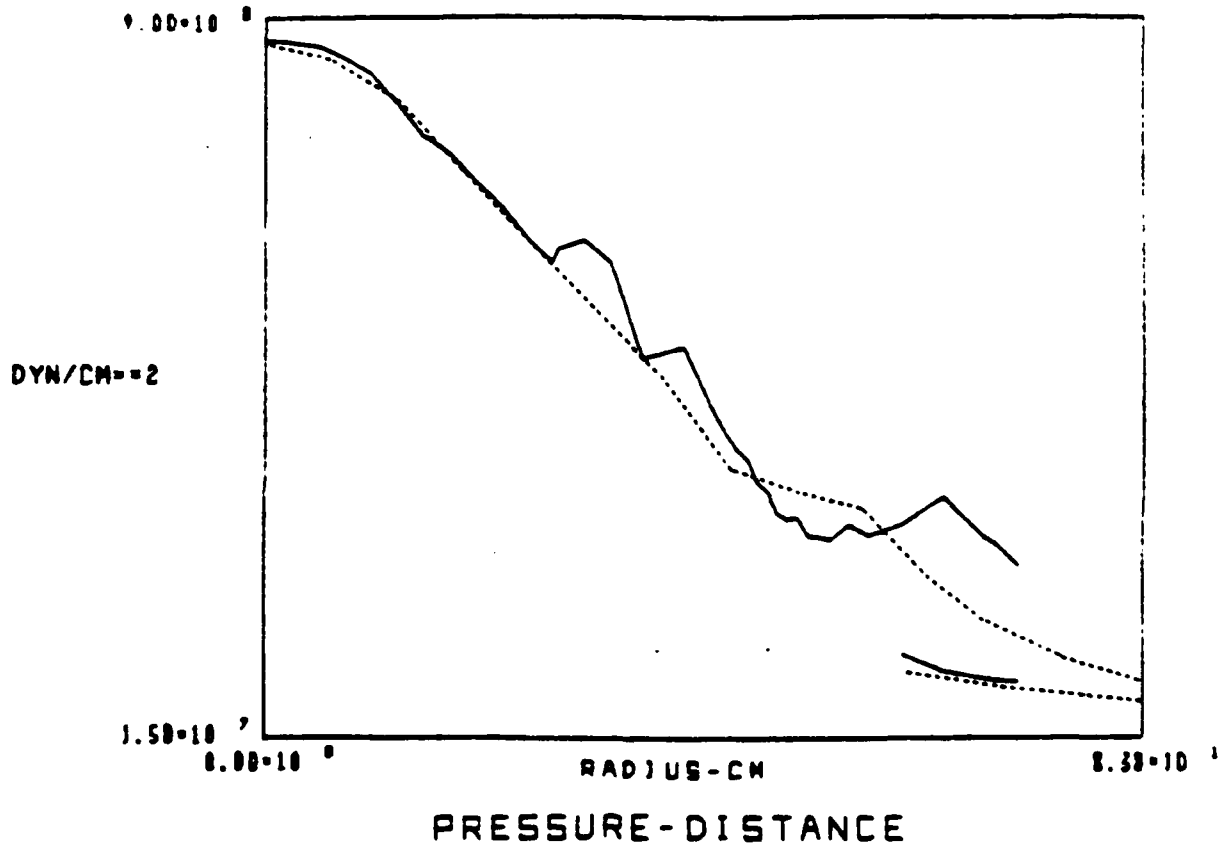


Fig. 8 - Computed peak overpressure vs distance along ground surface.  
Broken curve represents Carpenter's (1974) data.

APPENDIX B  
CONVERSION OF A CYLINDRICALLY CONFINED SURFACE  
EXPLOSION INTO A ONE-DIMENSIONAL BLAST WAVE



CONTENTS

1. INTRODUCTION .....	1
2. TWO DIMENSIONAL CALCULATION .....	4
3. CONCLUSIONS .....	9
REFERENCES .....	54

## CONVERSION OF A CYLINDRICALLY CONFINED SURFACE EXPLOSION INTO A ONE-DIMENSIONAL BLAST WAVE

### I. INTRODUCTION

In connection with the Dense Pack (Close-Spaced Basing) scheme, it has been pointed out by Latter that surface environments following a multiburst attack could be considerably more difficult to survive than those resulting from single bursts. Detonation simultaneously over all the shelters of a closely spaced array surrounds the vicinity of an individual shelter with high pressures, allowing the explosion to vent only in the upward direction. Hence, at least in the interior of the array, extremely high pressures are maintained for longer times, with the result that total impulses applied to ground structures are much greater than for a solitary explosion.

Latter proposed considering the following idealized situation: identical explosions are initiated simultaneously in an infinite regular hexagonal array at (or near) a uniform level plane surface (Fig. 1). Construct a vertical plane transverse to the line connecting every pair of neighboring centers, at the midpoint of the line. By symmetry, the six planes surrounding an explosion represent perfectly reflecting surfaces and together form a hexagonal parallelepiped (a cylinder having hexagonal cross section) with a vertical axis. This in turn can be approximated as a right circular cylinder with the same axis and cross sectional area. A two-dimensional  $r$ - $z$  code can be used to solve this idealized problem for surface and air bursts. It is clear, however, that asymptotically the flow becomes one-dimensional, evolving into a shock tube solution. In the limit where this asymptotic state has been

---

Manuscript approved November 9, 1982.

reached and where many weapon masses of air have been swept over, the one-dimensional form of the Sedov point blast solution should apply. The pressure on the ground as a function of time  $t$  is given by

$$p = k \rho_0 \frac{W}{\rho_0 A t}^{2/3}, \quad (1)$$

where  $\rho_0$  is the air density,  $W$  is the weapon yield,  $A$  is the cylinder area, and  $k$  is the function of the adiabatic index  $\gamma$  which is  $\leq 1$ . This is to be compared with the corresponding result for the case of a spherical free-field expansion, which is of the form

$$p = k' \rho_0 \left( \frac{W}{\rho_0 t^3} \right)^{2/5}. \quad (2)$$

As may be seen, the pressure given by Eq. (1) decreases in time more slowly than that of Eq. (2). Although the idea behind this so-called "bomb-in-a-can" model is simple and transparent, it leaves several important questions unanswered. First, how long (how many shock reflections) does it take to reach the asymptotic state, i.e., when does Eq. (1) become a good approximation? Second, to what extent is the prediction (1) dependent on idealizations of the model, e.g., perfect symmetry, perfect simultaneity, neglect of scouring and entraining of dust, etc? Finally, what are the long-term tactical consequences in this model of a multiburst scenario-- specifically, what can be said about the shape of the plume produced, how much dust is raised up and where does it go, what sort of turbulence is established and what are the consequences for radar transmission, etc?

In this report we describe a calculation which was carried out to investigate the first question, regarding the approach to the one-dimensional solution. We have used a version of the DNA one kiloton (1-kton) standard to

initialize a surface burst equivalent to 18 scaled megatons (Mton) in a cylinder of radius 900 feet. We find that the flow is close to one-dimensional after ~20 ms (the time required for the blast to reflect from the cylindrical wall and return to the origin, considerably less than might have been expected).

In the following section we describe in detail the calculations and the results obtained, and conclude with a brief discussion of what we intend to do in follow-on work.

## 2. TWO DIMENSIONAL CALCULATION

The development of the explosion can be viewed in terms of four stages. These are (1) the spherical free-field expansion prior to reflection at the outer boundary; (2) multiple distinct reflections off both boundaries, during which the transition to one-dimensional flow takes place; (3) approximately one dimensional expansion after reflecting gas-dynamic discontinuities are no longer discernible; (4) a gradual transition to three-dimensional flow as the finite extent of the array communicates itself to the interior. Stage (1) is not contained in our model; since the weapon mass greatly exceeds the mass of air contained within the initial explosion radius, the nature of the weapon and its constituents ought to be important in this stage, but no attempt has been made to improve on the realism of the 1-kton standard. Likewise, stage (4) is absent from the model (but see remarks in our concluding section below). Instead, we attempted to model stages (2) and (3).

The calculation was performed with 100 zones, each 10.2 cm in width in the radial direction, and 100 zones in the axial direction, 90 of which were 20.4 cm in length and the final 10 of which geometrically increased by increments of 11% (Fig. 2a). The final grid size was 10.2 m by 22.4 m. An equivalent 18 Mton surface burst was achieved by inserting values of density, energy, and momentum scaled from the 1 kton standard. Since values of the 1 kton standard were only available from 10 meters (an 18 Mton surface burst scales to about eight meters after we double the yield to account for surface reflection), we created initial profiles by increasing the density, internal energy, and momentum by a factor of 1.4. As a result the initial energy was

$3.1 \times 10^{19}$  ergs and the mass was  $8.2 \times 10^6$  g, deposited into a hemisphere of 10 m radius. The effect of this scaling was to simulate the initiation of an event with the appropriate yield and weapon mass, but with profiles (as a function of distance from the burst site) which were not correct in detail. During the early phases of the problem they must give rise to discrepant behavior, but at later times this presumably becomes insignificant.

The numerical simulation was performed using the NRL FAST2D code which utilizes the latest version of Flux Corrected Transport (FCT). The code was essentially the same configuration used previously for 104-ft and 50-ft 1-kton HOB calculations. A reflection condition was imposed on the left and bottom boundaries, as before, and on the right-hand boundary as well. In addition to the diagnostics employed previously, we introduced several devised specifically for this problem.

Figure 2b shows plots of the initial profiles of the mass density, velocity, pressure and energy density. Note that all of these variables achieve their maxima at the leading shock. To convert these profiles into their counterparts for the 18 Mton case, it is necessary to dilate by a factor of  $(900 \text{ ft}/10 \text{ m})^{1/3} = 27.4$ . Likewise, the time scale has to be expanded by the same factor.

The reflection of this initial blast wave from the outer radius of the can and the subsequent evolution of the system are depicted in Fig. 3. This shows pressure contours and velocity vectors plotted at intervals of 100 cycles (approximately 30-50  $\mu\text{s}$ ). Although the time intervals vary because of the changing time step, these plots are in a sense equally separated in terms of the "total change" in the system, because when flow and sound speeds are

large the timestep decreases, and vice versa. Note how rapidly the reflected shock propagates to the left; almost invisible at cycle 201, it is nearly halfway across the mesh at cycle 301. It travels upward almost as rapidly, reaching an altitude of 10 m by cycle 601. By cycle 801 it appears to have overtaken the primary shock wave, which is considerably distorted after cycle 1501. On the right hand boundary the reflection, which is initially regular, gradually converts to Mach reflection. This development is of course analogous to the transition to Mach reflection observed in the HOB case<sup>3</sup>. It is hard to see exactly when transition occurs, but a Mach stem is clearly visible in the pressure plots at cycle (40) and thereafter. If we examine Carpenter's results regarding the boundary between regular and Mach reflection in real air at Mach numbers  $M \geq 10$ , we see that the angle at which transition occurs depends on  $M$  only weakly and is approximately equal to  $45^\circ$ . The Mach stem ought thus to have first formed around cycle 701 to 801, but the region of reflection is not sufficiently well resolved to show it.

In Fig. 4 another view of the same time sequence is shown. These surface pressure plots are particularly well suited for showing shock and rarefaction waves propagating through the system. Since the pressures are interpolated onto a regular mesh before plotting, peak values are lowered by as much as a factor of two. This reduces contrast somewhat and makes some features appear to move up and down erratically in time, but the overall morphology is very clear. We see, for example, how the shock reflected radially from the origin appears to run out of gas at about cycle 901, while a train of waves reverberates down from the top. One of these finally reaches the radially-propagated ground shock at about cycle 1801 and begins to push it along. Throughout this time the pressures in the lower right corner of the system

remain low. Meanwhile, the shock front rising toward the top of the system, which is madly churning around at cycle 1201, becomes smoother as shocks propagate back down from it.

Figure 5 shows the pressure recorded at a series of sensors located across the bottom of the can, ranging from the burst center (a) to the outer edge (l). Note that, although the initial profiles have a sharp (one-zone) discontinuity at the leading edge, the pressure peak at sensor l takes about 70  $\mu$ s to build up to the maximum. This is about a hundred times as long as it takes the shock to propagate across one zone. It is, however, not out of line with the time required for the air behind the shock (velocity  $1.5 \times 10^6$  cm/s) to cross a zone, about 7  $\mu$ s. The density (and other fluid variables) can build up to their post-reflection values when the air from  $(\gamma+1)/(\gamma-1) \approx 10$  cells has been compressed into the cell closest to the wall. Using Carpenter's<sup>4</sup> reflection factors for normally incident shocks, we calculate that the free-field pressure, initially 3.5 kbar, should reflect up to about 40 kbar, which is to be compared with the value of 25 kbar we actually obtained. If we look at sensors closer to the burst site, we see that the pressure peaks get continuously sharper, finally turning into an almost discontinuous spike at the origin, as the imploding shock attempts to develop into a singularity.

The information in these pressure histories is capsulized in Fig. 6, which shows the maximum pressure recorded during the course of the calculation as a function of sensor location. Note that the peak at  $r = 0$  is nearly as high as that at the periphery, in contrast with results reported by Pyatt<sup>5</sup>. This may be attributable to the lower resolution he used, or to the greater numerical dissipation in the HULL code. Only one peak was detected at each

sensor location. Our calculation was run for less than 1 ms, or (scaled to 18 Mton) rather less than the 30 ms Pyatt required to see a second peak at the periphery when the re-reflected shock impinges there; the two calculations are thus not inconsistent in this regard.

The approach to one-dimensional motion may be inferred from the contour plots of Fig. 4, where it is seen that the leading edge of the upward-propagating blast wave becomes more and more horizontal, and from the velocity vector plots of Fig. 3, which show that the flow becomes increasingly vertical and that velocities well behind the upper front tend to die away. A more quantitative comparison is possible if we compute the average pressure on the bottom,

$$\bar{p} = \frac{2\pi \int_0^R p(r,0)rdr}{2\pi \int_0^R r dr} \quad (3)$$

as a function of time. The result is shown as the solid line in Fig. 7. For comparison, formula (1) has been added (broken line), using yield  $W = 1.4$  kton and area  $A = 100\pi \text{ m}^2$ , with  $\gamma = 1.2$ . The agreement between the two is striking, particularly since we expect to observe it only asymptotically. It is clear that the one-dimensional approximation becomes valid very early, probably because the reverberating shocks behind the leading front of the blast propagate so rapidly in the hot medium.

### 3. CONCLUSIONS

We have successfully modelled the "bomb-in-a can" using FAST2D, a general-purpose code which required no special modification for this problem.

Although we only ran the calculation out to an altitude of about 20 m (twice the system radius), the sliding grid (continuous adaptive rezone) capability of FAST2D allows us to continue the run as long as desired by stretching the mesh in the vertical direction.

Our results show that the asymptotic one-dimensional state is approached very rapidly, apparently because the multiply reflected shocks propagate much faster than the original blast wave. Two or three reflections across the radius of the system effectively equilibrate the flow and relax it to a state of vertical expansion. The simulation reveals a complex pattern of reverberations, with reflection occurring off all the boundaries and regions where conditions are highly nonuniform.

A number of modifications are required to make these results applicable to an actual tactical situation. Perhaps the most important is the inclusion of dust scoured up from the ground and entrained in the wind fields following the blast. A realistic description would require not only that the dust mass load the air, but that air and dust be permitted to exchange momentum and energy. The bottom boundary conditions should also be changed to model the energy that goes into cratering and scouring.

If the calculation is to be continued to late times, atmospheric stratification should be included. The effects of water vapor and turbulence

should also be modelled. Also, venting of the explosion in the horizontal direction (in the case of an RV exploding near the edge of a finite-sized array of shelters, or for an explosion in the interior of the array which has begun to feel the pressure in the outer explosions drop as they vent outward) can be modelled by having the radius  $R$  increase as a function of height. Of course, airblast situations in which the explosion originates above the ground can also be investigated (in which case Mach stems could appear on the ground as well as the sides of the system).

Although some of these extensions require nontrivial code modifications, there is no reason in principal why the present results could not be augmented and refined greatly by additional calculations.

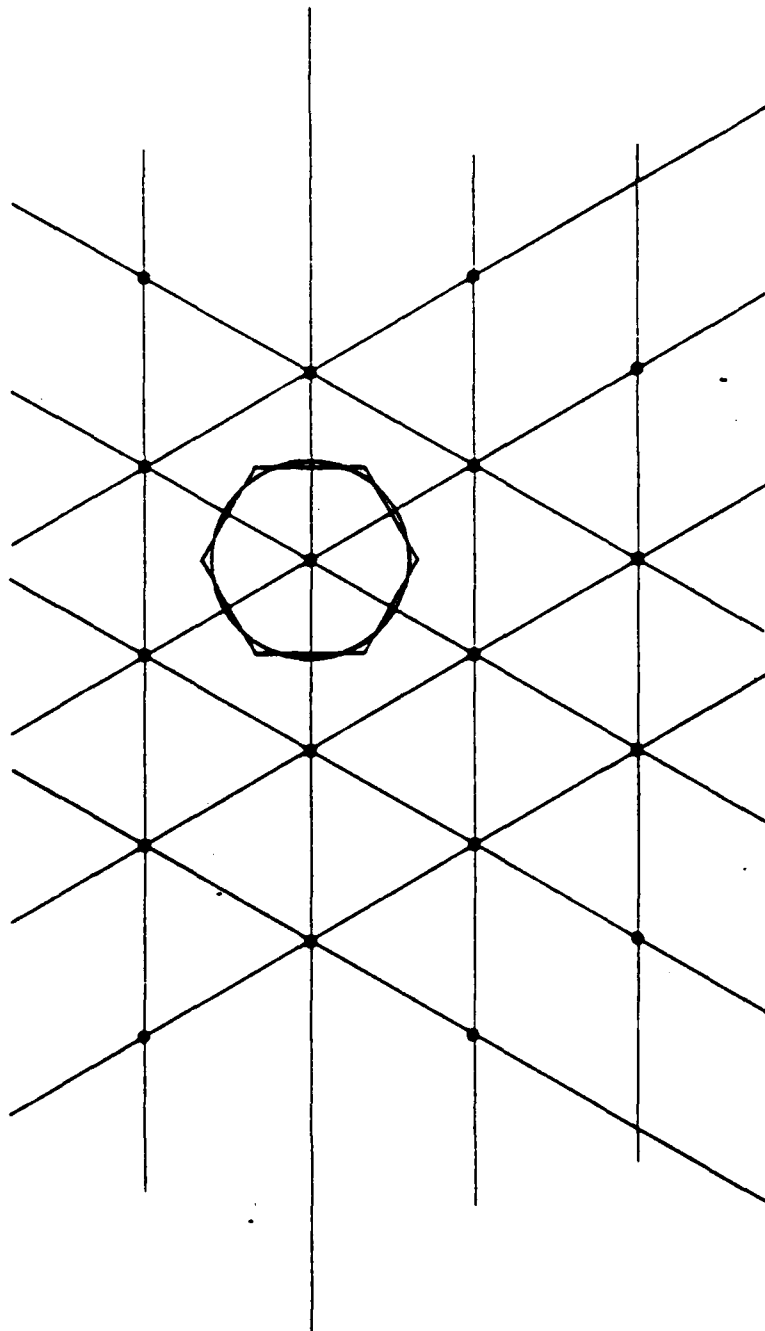


**Fig. 1 — Schematic of unbounded hexagonal array of shelters with 1800 ft separations on a perfectly reflecting plane. Shown is the cross section of the hexagonal parallelepiped formed by the planes bisecting the lines connecting a given shelter with its six nearest neighbors (reflection planes), along with the coaxial cylinder having the same cross sectional area.**

# GRID

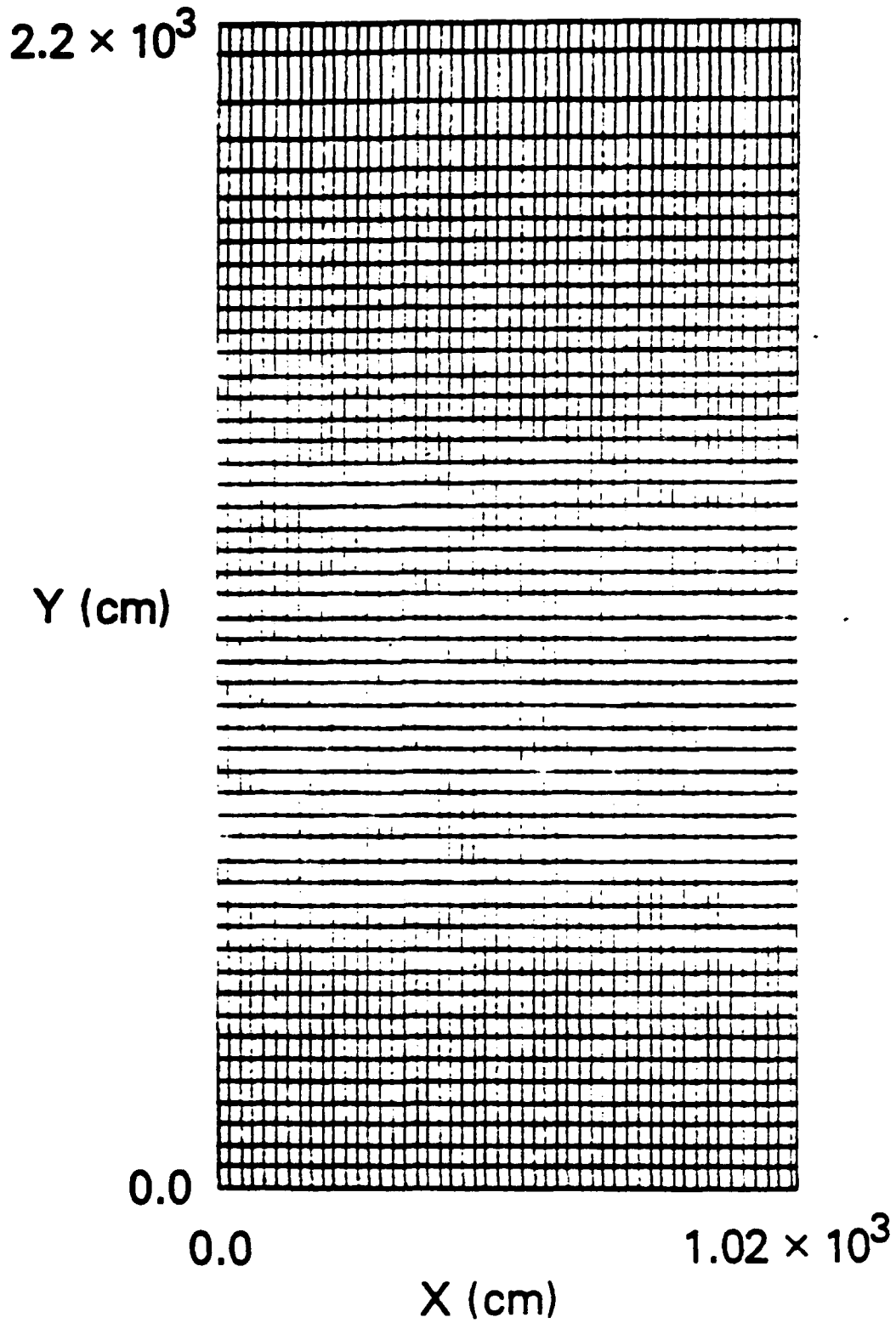


Fig. 2(a) — Mesh used in the calculation. Zones are of equal width in the radial direction, but are stretched vertically near the top of the mesh.

SHOCK ONE DEE CODE

CYCLE = 0.00 \* 10<sup>0</sup>

TIME = 0.00 \* 10<sup>0</sup>

NO ZONES = 3.00 \* 10<sup>2</sup>

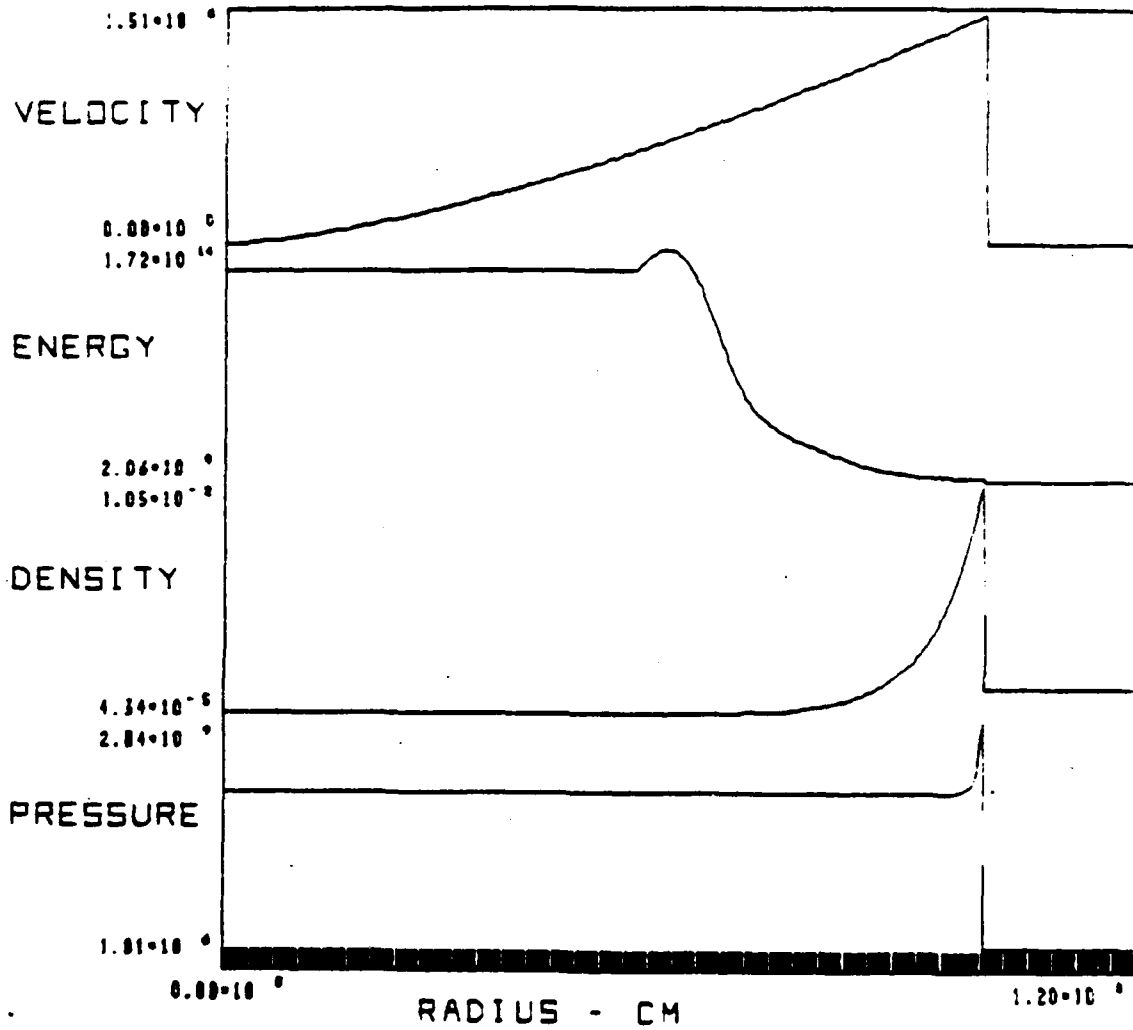


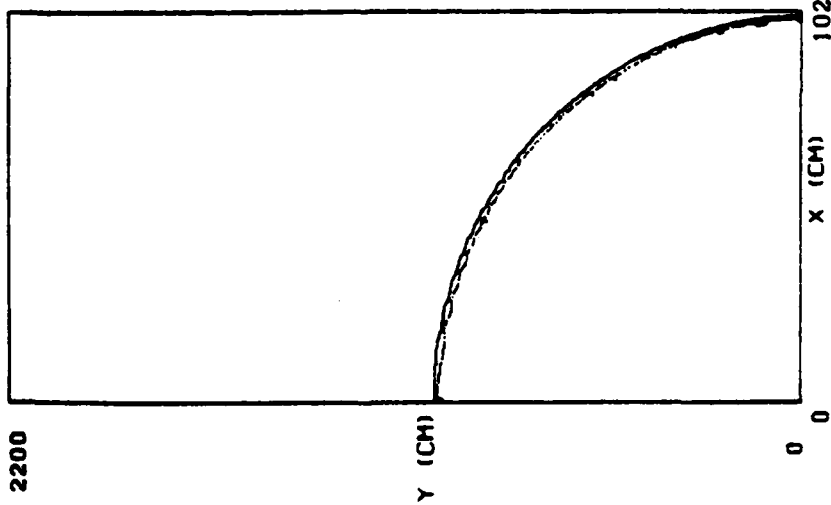
Fig. 2(b) — Profiles used to initialize calculations (modification of the 1-kton standard). Velocities are directed radially outward from burst site at origin.

PRESSURE CONTOURS

DENSEPACK 10 MEAGATONS

CYCLE = 1  
2200

TIME = 0.00 \* 10<sup>0</sup>

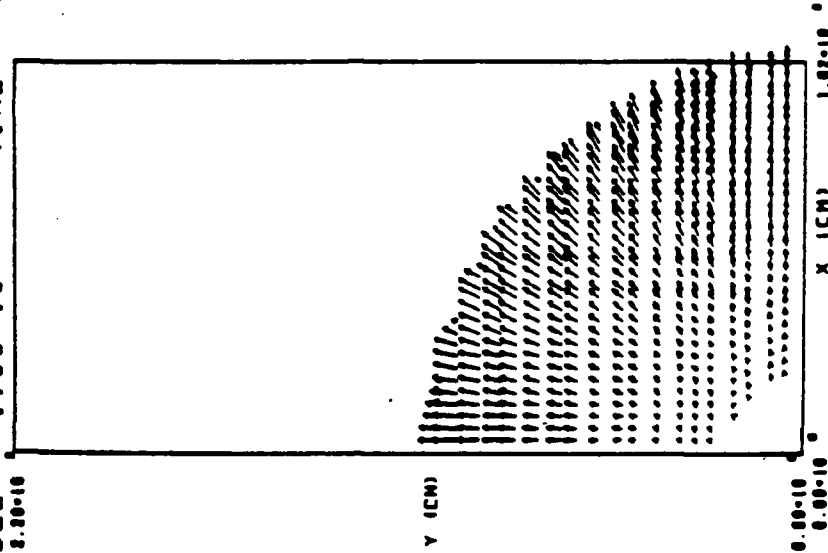


5.00 * 10 <sup>0</sup>
1.00 * 10 <sup>1</sup>
5.21 * 10 <sup>1</sup>
6.57 * 10 <sup>1</sup>
5.03 * 10 <sup>1</sup>
7.29 * 10 <sup>1</sup>
8.61 * 10 <sup>1</sup>
1.00 * 10 <sup>2</sup>

VELOCITY VECTORS

DENSEPACK 10 MEAGATONS

CYCLE = 1.00 \* 10<sup>0</sup> TIME = 0.00 \* 10<sup>0</sup>  
2.00 \* 10<sup>0</sup>

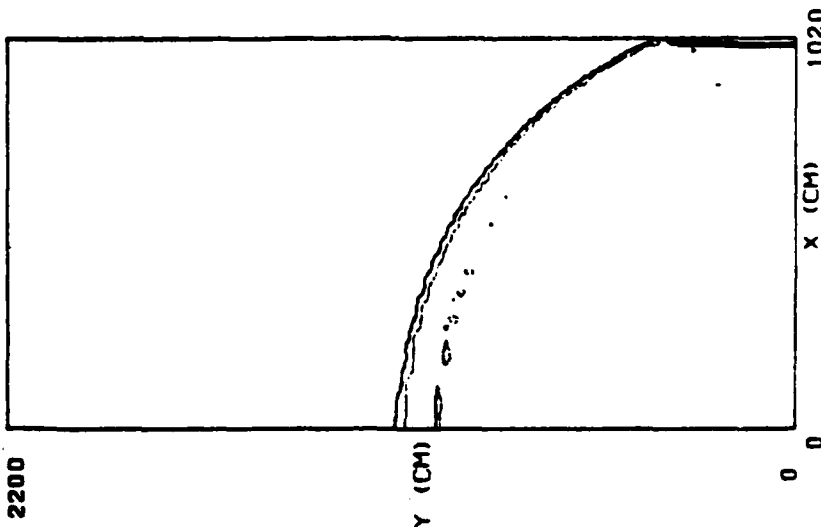


MAX VELOCITY = 1.00 \* 10<sup>4</sup>

Fig. 3a — Pressure contours and velocity vectors calculated using FAST2D, shown at intervals of 100 cycles

PRESSURE CONTOURS

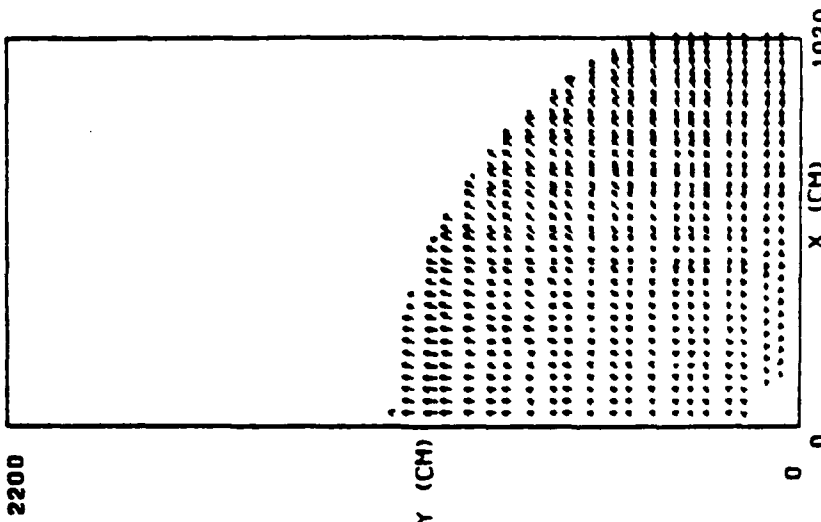
DENSEPACK 18 MEAGATONS  
 CYCLE= 101 TIME=  $5.77 \cdot 10^{-5}$   
 2200



- 5.00e-10
- 1.00e-10
- 1.21e-10
- 1.57e-10
- 5.91e-10
- 7.20e-10
- 8.40e-10
- 1.00e-10

VELOCITY VECTORS

DENSEPACK 18 MEAGATONS  
 CYCLE= 101 TIME=  $5.77 \cdot 10^{-5}$   
 2200



MAX VELOCITY =  $2.95 \cdot 10^{-4}$

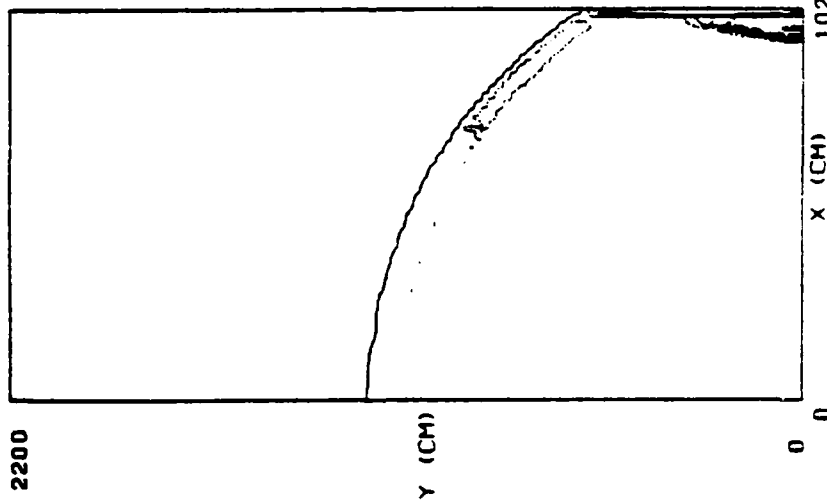
Fig. 3b -- Pressure contours and velocity vectors calculated using FAST2D, shown at intervals of 100 cycles.

PRESSURE CONTOURS

DENSEPACK 18 MEAGATONS

CYCLE - 201

TIME -  $1.21 \cdot 10^{-4}$



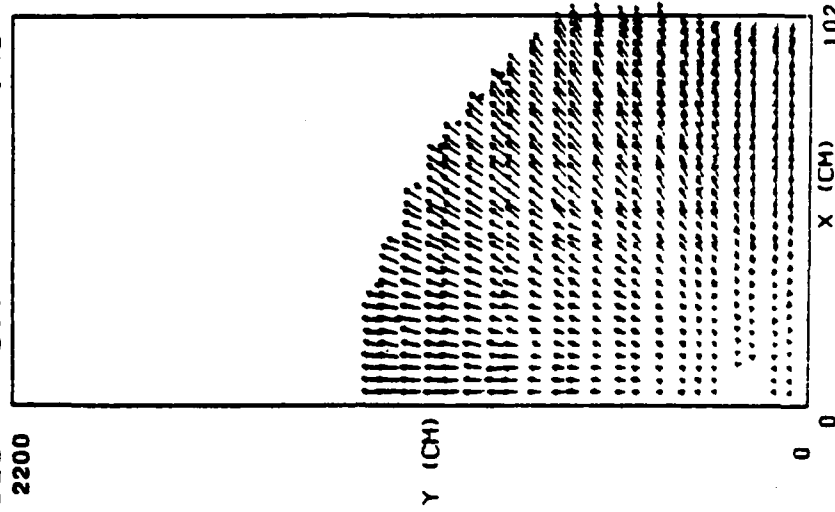
5.00	10
1.04	10
1.21	10
1.57	10
5.04	10
7.39	10
8.40	10
1.00	10

VELOCITY VECTORS

DENSEPACK 18 MEAGATONS

CYCLE - 201

TIME -  $1.21 \cdot 10^{-4}$



MAX VELOCITY =  $1.62 \cdot 10^{-4}$

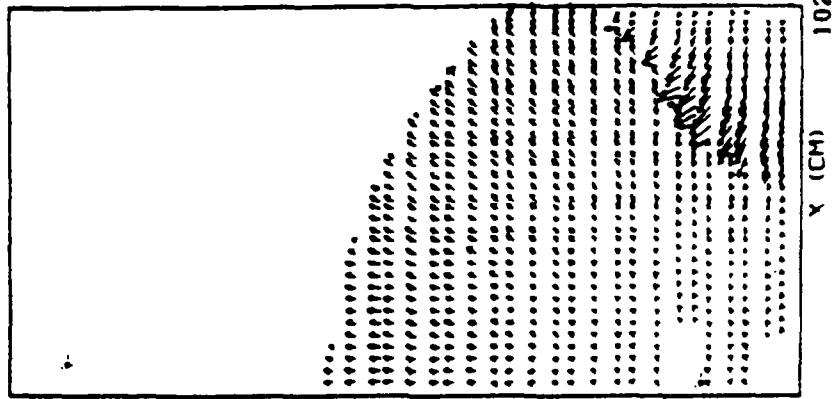
Fig. 3c — Pressure contours and velocity vectors calculated using FAST2D, shown at intervals of 100 cycles

VELOCITY VECTORS

DENSEPACK 18 MEAGATONS

CYCLE = 301

TIME =  $1.79 \cdot 10^{-4}$



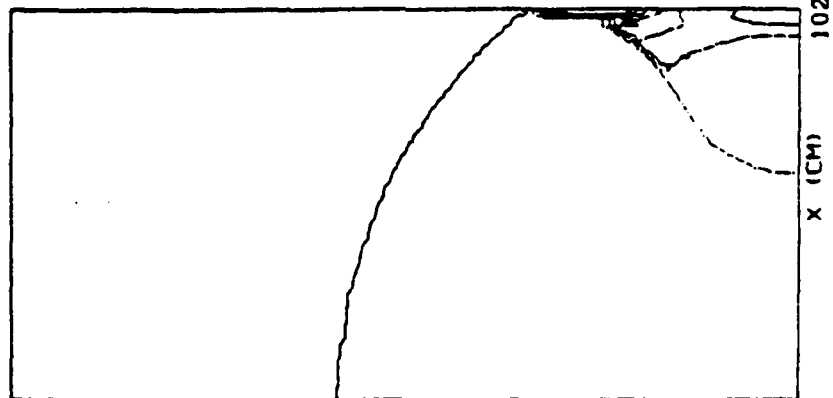
5.00	•
1.00	•
5.21	•
1.57	•
5.91	•
7.39	•
8.61	•
1.00	•

PRESSURE CONTOURS

DENSEPACK 18 MEAGATONS

CYCLE = 301

TIME =  $1.79 \cdot 10^{-4}$



MAX VELOCITY =  $3.21 \cdot 10^6$

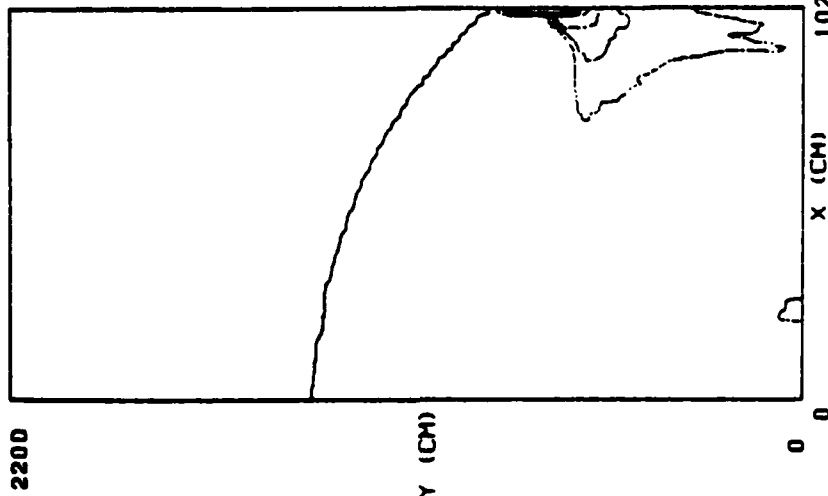
Fig. 3d — Pressure contours and velocity vectors calculated using FAST2D, shown at intervals of 100 cycles

PRESSURE CONTOURS

DENSEPACK 18 MEAGATONS

CYCLE 401

TIME  $2.29 \cdot 10^{-4}$



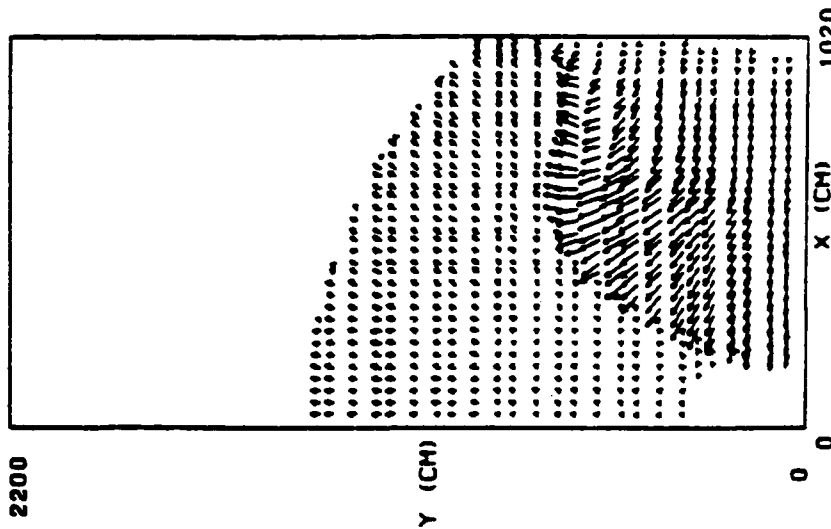
- 5.00 · 10<sup>6</sup>
- 1.00 · 10<sup>7</sup>
- 1.21 · 10<sup>7</sup>
- 1.57 · 10<sup>7</sup>
- 5.93 · 10<sup>7</sup>
- 7.29 · 10<sup>7</sup>
- 8.65 · 10<sup>7</sup>
- 1.00 · 10<sup>8</sup>

VELOCITY VECTORS

DENSEPACK 18 MEAGATONS

CYCLE 401

TIME  $2.29 \cdot 10^{-4}$

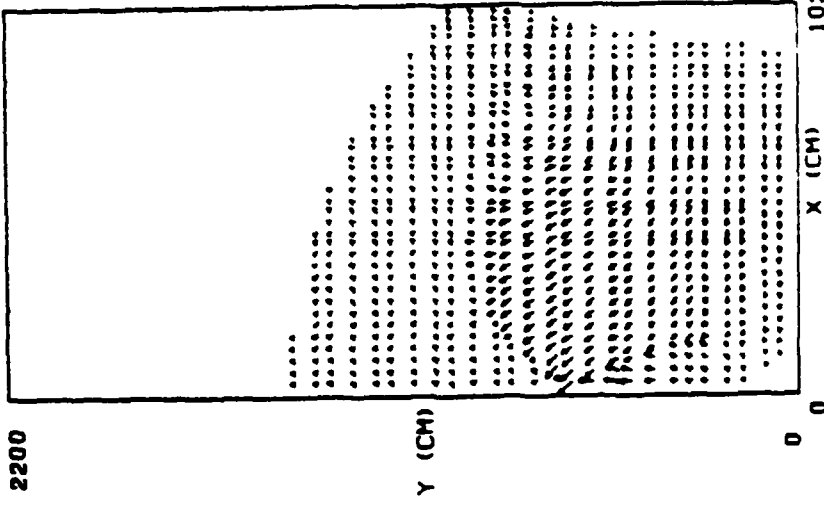


MAX VELOCITY =  $3.56 \cdot 10^4$

Fig. 3e -- Pressure contours and velocity vectors calculated using FAST2D, shown at intervals of 100 cycles

VELOCITY VECTORS

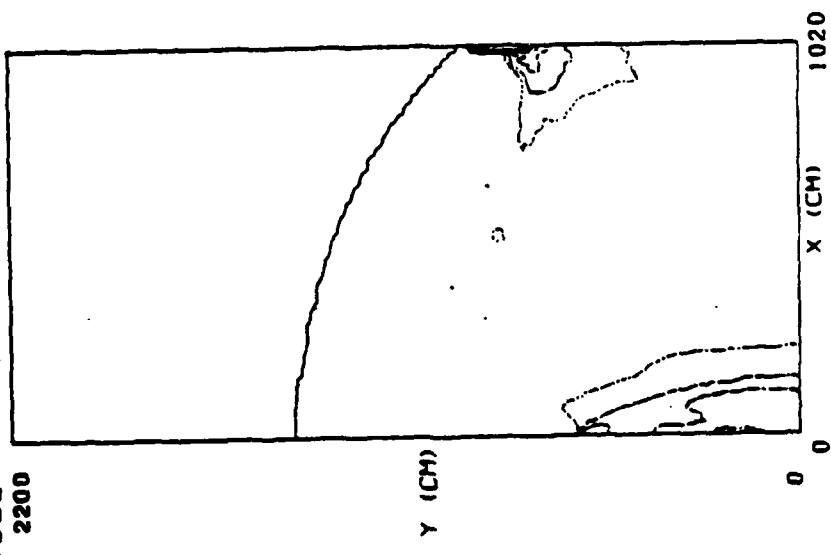
DENSEPACK 18 MEAGATONS  
 CYCLE = 501 TIME =  $2.67 \times 10^{-4}$   
 2200



5.00e-10
1.00e-10
1.21e-10
4.57e-10
5.05e-10
7.39e-10
0.60e-10
1.00e-10

PRESSURE CONTOURS

DENSEPACK 18 MEAGATONS  
 CYCLE = 501 TIME =  $2.67 \times 10^{-4}$   
 2200



MAX VELOCITY =  $7.48 \times 10^{-6}$

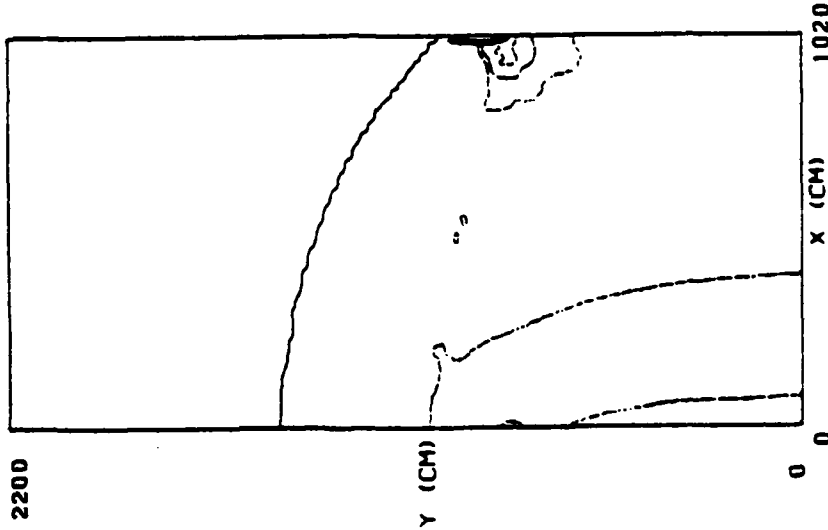
Fig. 3f — Pressure contours and velocity vectors calculated using FAST2D, shown at intervals of 100 cycles

PRESSURE CONTOURS

DENSEPACK 18 MEAGATONS

CYCLE= 601

TIME=  $2.98 \cdot 10^{-4}$



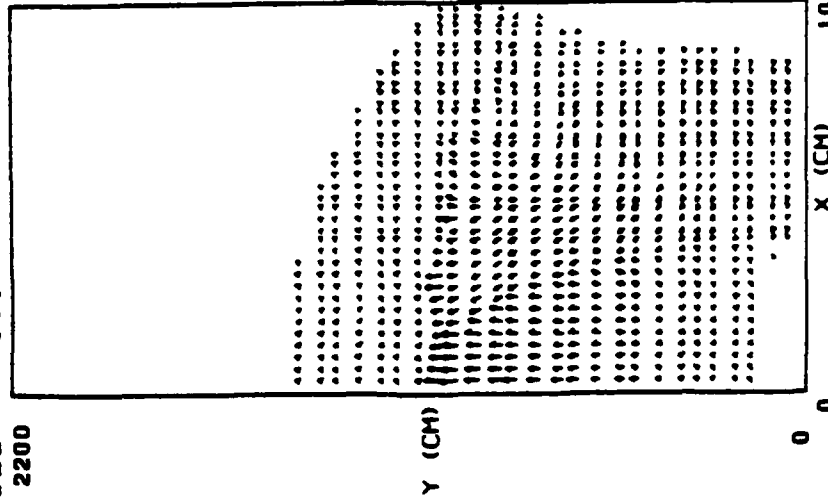
5.00	•
1.00	•
3.21	•
1.57	•
5.98	•
7.39	•
8.60	•
1.00	•

VELOCITY VECTORS

DENSEPACK 18 MEAGATONS

CYCLE= 601

TIME=  $2.98 \cdot 10^{-4}$



MAX VELOCITY =  $7.93 \cdot 10^{-4}$

Fig. 3g -- Pressure contours and velocity vectors calculated using FAST2D, shown at intervals of 100 cycles



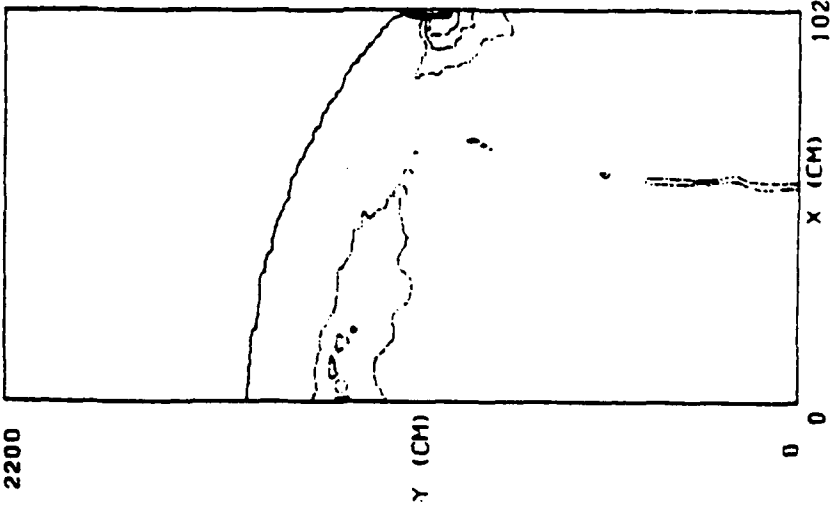
PRESSURE CONTOURS

DENSEPACK 18 MEAGATONS

CYCLE = 801  
2200

TIME =  $3.62 \cdot 10^{-4}$

5.00	•
1.00	•
5.21	•
1.57	•
5.93	•
7.29	•
8.64	•
1.00	•

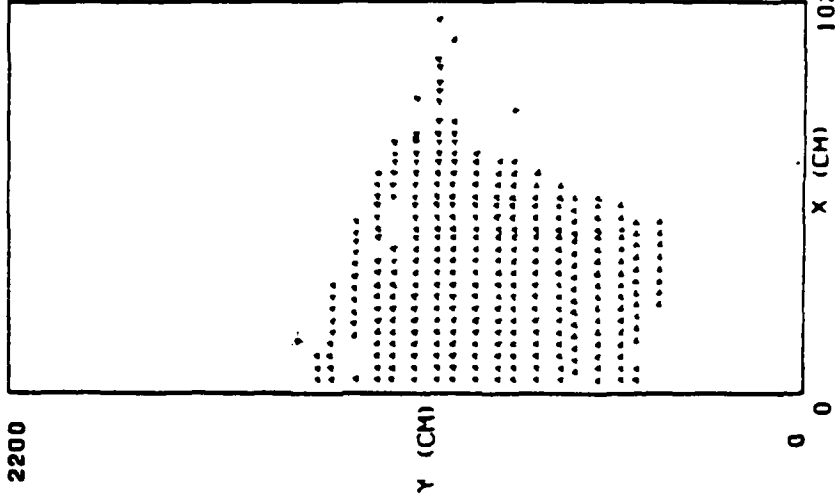


VELOCITY VECTORS

DENSEPACK 18 MEAGATONS

CYCLE = 801  
2200

TIME =  $3.62 \cdot 10^{-4}$



MAX VELOCITY =  $1.78 \cdot 10^7$

Fig. 31 --- Pressure contours and velocity vectors calculated using FAST2D, shown at intervals of 100 cycles

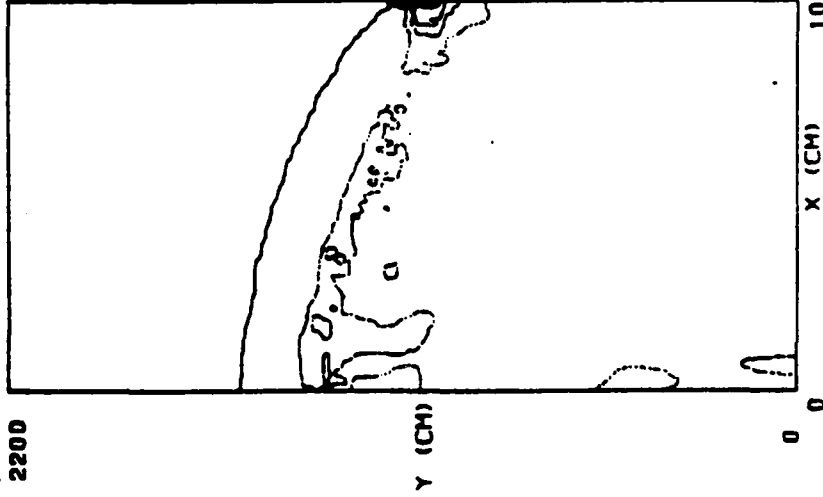
PRESSURE CONTOURS

DENSEPACK 18 MEAGATONS

CYCLE = 901

TIME =

$3.83 \cdot 10^{-4}$



5.88 · 10 <sup>-4</sup>
1.88 · 10 <sup>-4</sup>
1.21 · 10 <sup>-4</sup>
1.57 · 10 <sup>-4</sup>
5.93 · 10 <sup>-5</sup>
7.39 · 10 <sup>-5</sup>
9.65 · 10 <sup>-5</sup>
1.88 · 10 <sup>-4</sup>

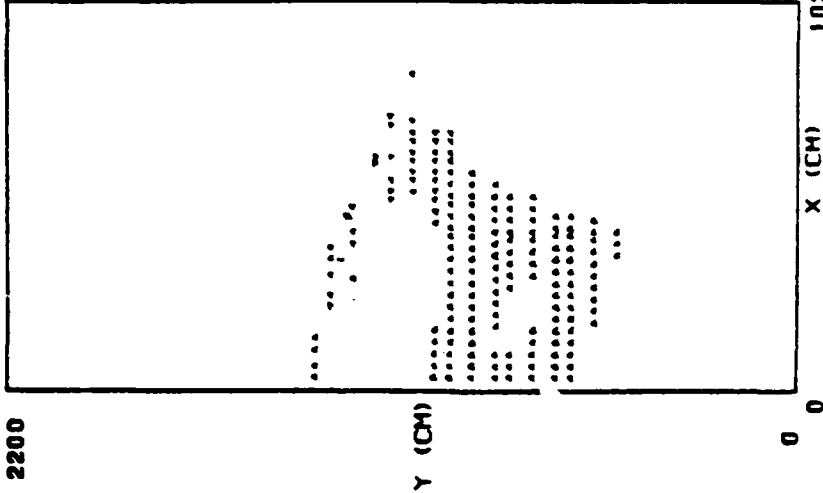
VELOCITY VECTORS

DENSEPACK 18 MEAGATONS

CYCLE = 901

TIME =

$3.83 \cdot 10^{-4}$

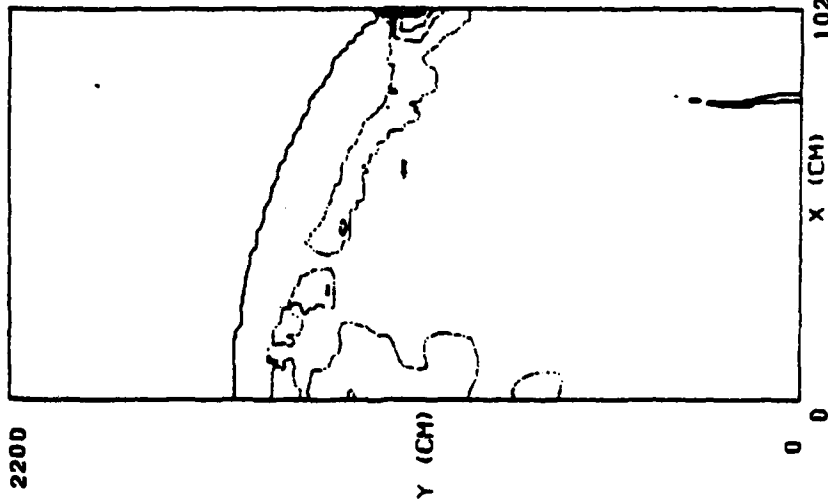


MAX VELOCITY =  $2.26 \cdot 10^{-7}$

Fig. 3j — Pressure contours and velocity vectors calculated using FAST2D, shown at intervals of 100 cycles

PRESSURE CONTOURS

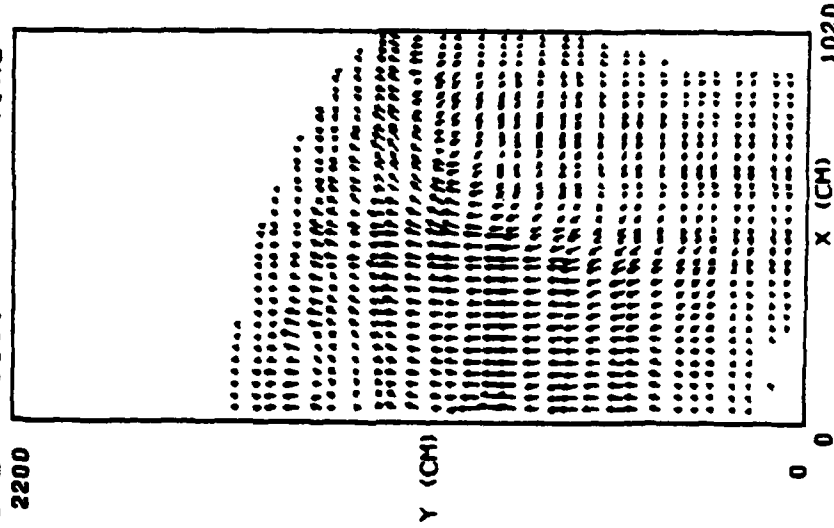
DENSEPACK 18 MEAGATONS  
CYCLE = 1001 TIME =  $4.06 \cdot 10^{-4}$



5.00 · 10	9
1.00 · 10	9
2.21 · 10	9
1.57 · 10	9
5.91 · 10	9
7.20 · 10	9
8.49 · 10	9
1.00 · 10	10

VELOCITY VECTORS

DENSEPACK 18 MEAGATONS  
CYCLE = 1001 TIME =  $4.06 \cdot 10^{-4}$



MAX VELOCITY =  $3.70 \cdot 10^{-4}$

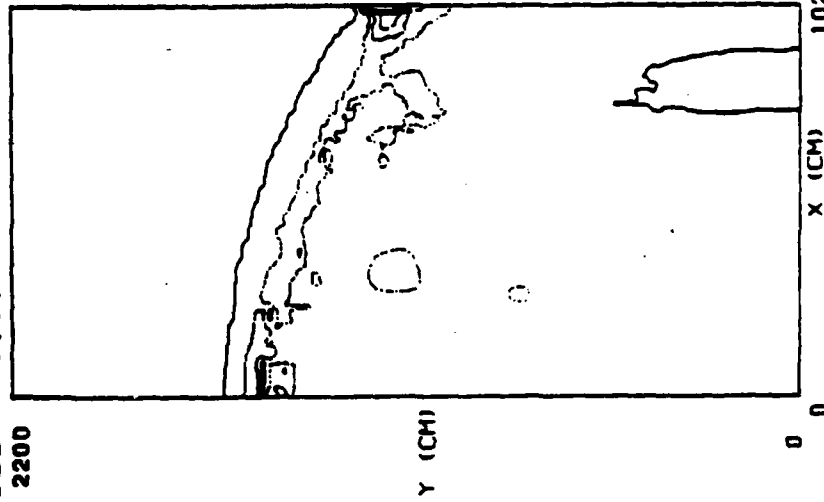
Fig. 3k - Pressure contours and velocity vectors calculated using FAST2D, shown at intervals of 100 cycles

**PRESSURE CONTOURS**

DENSEPACK 18 MEAGATONS

CYCLE= 1101

TIME=  $4.39 \times 10^{-4}$



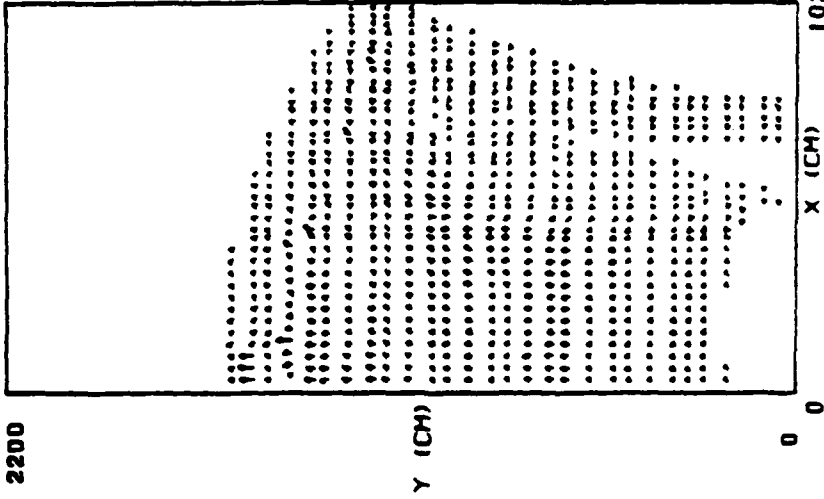
5.00E+10
1.06E+10
3.21E+09
9.57E+08
5.95E+08
7.29E+08
8.64E+08
1.00E+09

**VELOCITY VECTORS**

DENSEPACK 18 MEAGATONS

CYCLE= 1101

TIME=  $4.39 \times 10^{-4}$



MAX VELOCITY =  $7.41 \times 10^{-4}$

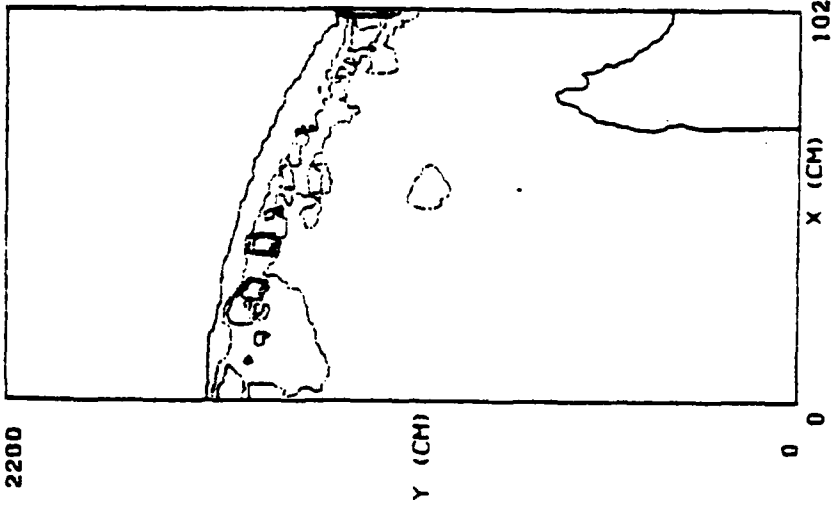
Fig. 31 — Pressure contours and velocity vectors calculated using FAST2D, shown at intervals of 100 cycles

PRESSURE CONTOURS

DENSEPACK 18 MEAGATONS.

CYCLE= 1201  
2200

TIME=  $4.66 \cdot 10^{-4}$



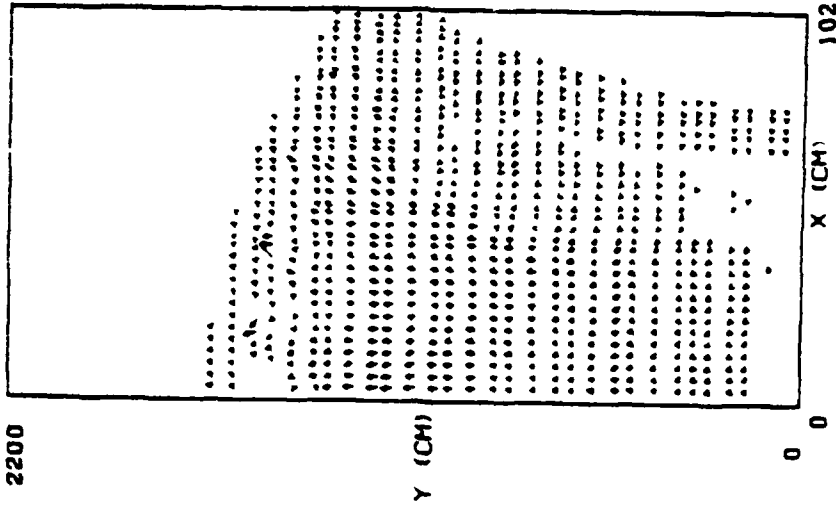
5.00	10	9
1.04	10	9
5.21	10	9
6.57	10	9
5.93	10	9
7.29	10	9
8.64	10	9
1.00	10	10

VELOCITY VECTORS

DENSEPACK 18 MEAGATONS

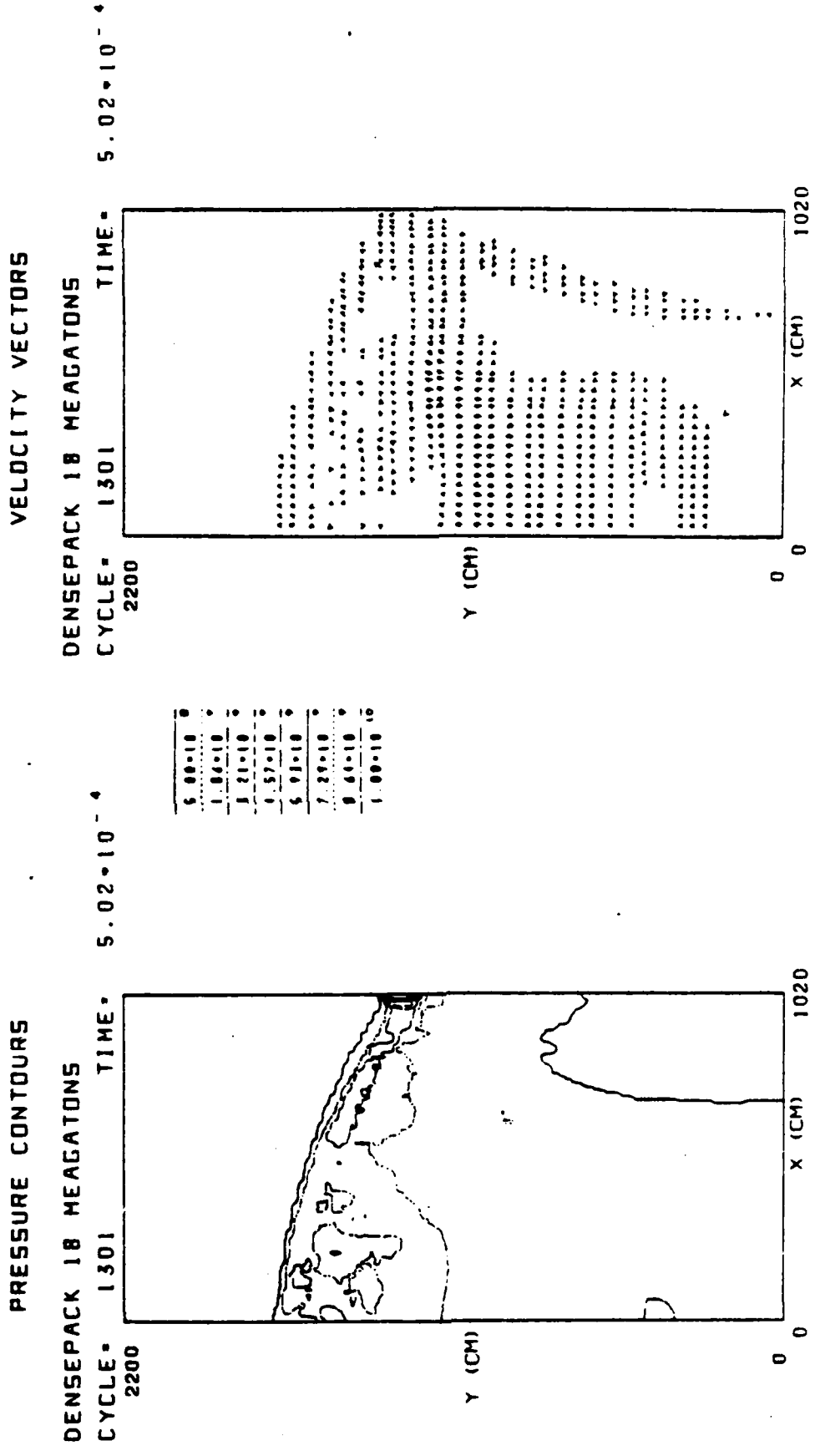
CYCLE= 1201  
2200

TIME=  $4.66 \cdot 10^{-4}$



MAX VELOCITY =  $7.64 \cdot 10^6$

Fig. 3m - Pressure contours and velocity vectors calculated using FAST2D, shown at intervals of 100 cycles

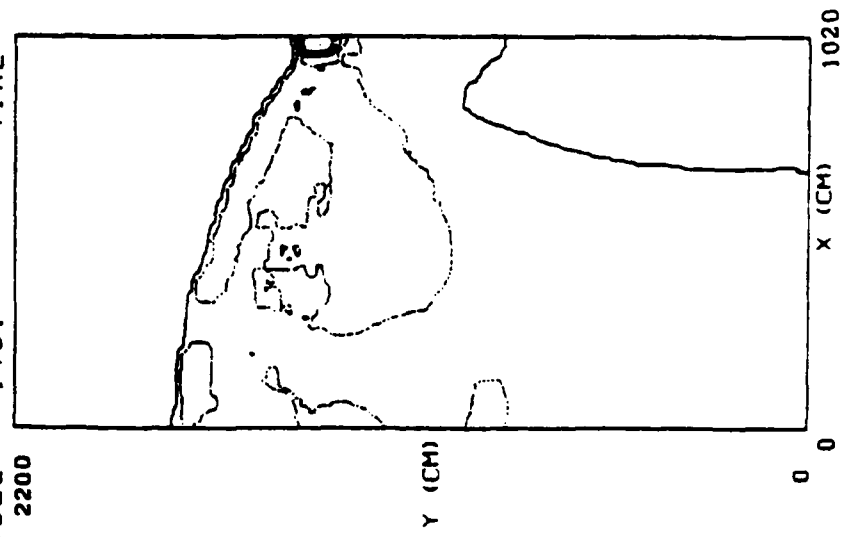


MAX VELOCITY =  $9.78 \cdot 10^{-4}$

Fig. 3h — Pressure contours and velocity vectors calculated using FAST2D, shown at intervals of 100 cycles

PRESSURE CONTOURS

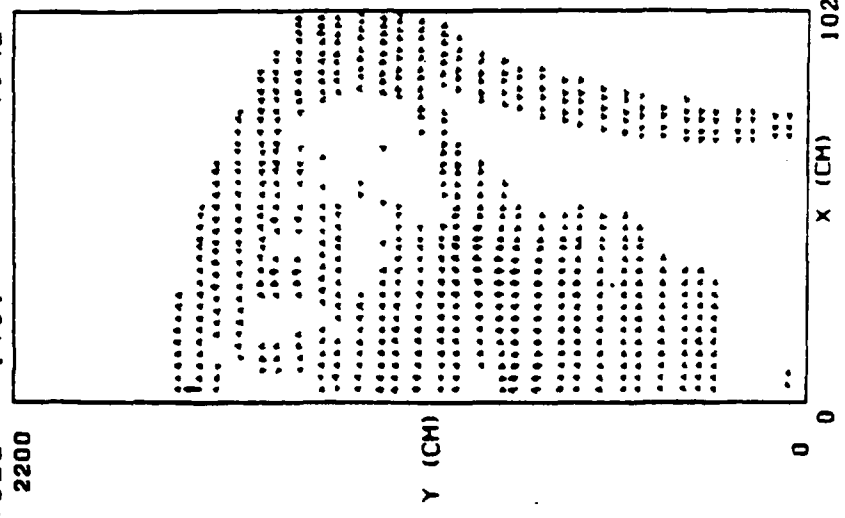
DENSEPACK 18 MEAGATONS  
 CYCLE= 1401 TIME=  $5.51 \cdot 10^{-4}$   
 2200



5.00	10
1.00	10
3.21	10
4.57	10
5.93	10
7.29	10
8.64	10
1.00	10 10

VELOCITY VECTORS

DENSEPACK 18 MEAGATONS  
 CYCLE= 1401 TIME=  $5.51 \cdot 10^{-4}$   
 2200



MAX VELOCITY =  $5.95 \cdot 10^{-4}$

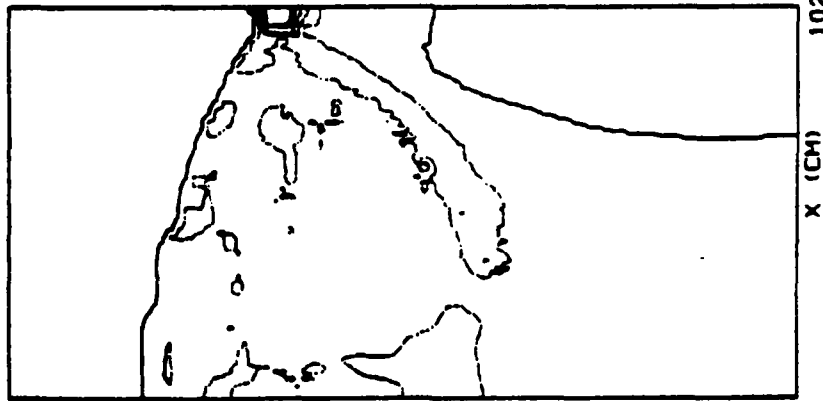
Fig. 30 - Pressure contours and velocity vectors calculated using FAST2D, shown at intervals of 100 cycles

PRESSURE CONTOURS

DENSEPACK 18 MEAGATONS

CYCLE- 1501

TIME-  $6.01 \cdot 10^{-4}$



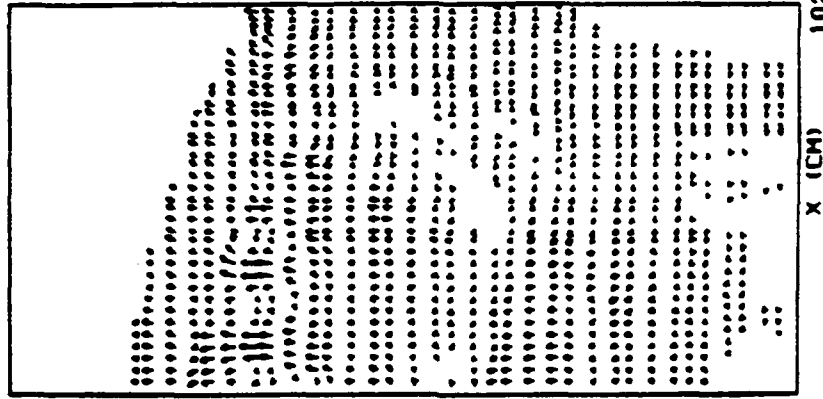
5.00-10	0
1.00-10	0
1.21-10	0
6.57-10	0
5.93-10	0
7.29-10	0
8.41-10	0
1.00-10	10

VELOCITY VECTORS

DENSEPACK 18 MEAGATONS

CYCLE- 1501

TIME-  $6.01 \cdot 10^{-4}$



MAX VELOCITY =  $3.71 \cdot 10^4$

Fig. 3p - Pressure contours and velocity vectors calculated using FAST2D, shown at intervals of 100 cycles

PRESSURE CONTOURS

DENSEPACK 18 MEAGATONS

CYCLE= 1601

2200

TIME=  $6.50 \cdot 10^{-4}$



5.00 · 10 <sup>-4</sup>
1.20 · 10 <sup>-4</sup>
3.31 · 10 <sup>-4</sup>
4.57 · 10 <sup>-4</sup>
5.95 · 10 <sup>-4</sup>
7.29 · 10 <sup>-4</sup>
8.60 · 10 <sup>-4</sup>
1.00 · 10 <sup>-3</sup>

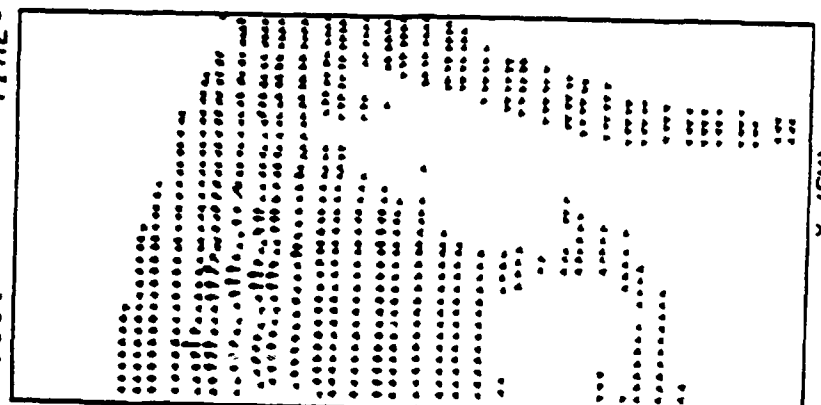
VELOCITY VECTORS

DENSEPACK 18 MEAGATONS

CYCLE= 1601

2200

TIME=  $6.50 \cdot 10^{-4}$



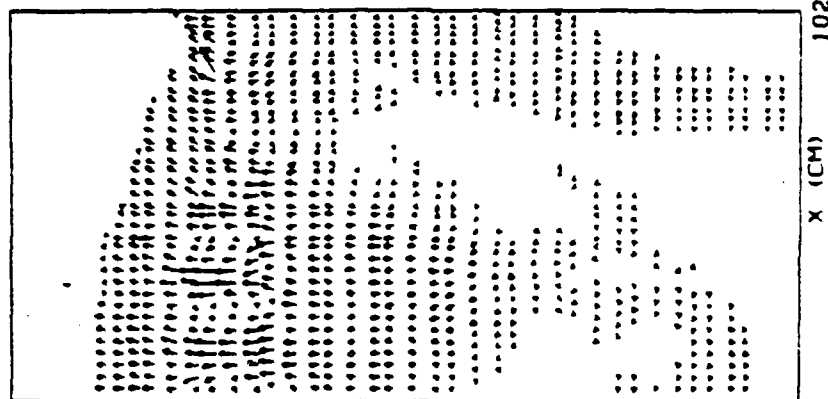
MAX VELOCITY =  $4.66 \cdot 10^{-4}$

Fig. 3q — Pressure contours and velocity vectors calculated using FAST2D, shown at intervals of 100 cycles

VELOCITY VECTORS

DENSEPACK 18 MEAGATONS

CYCLE= 1701 TIME=  $7.00 \cdot 10^{-4}$   
 2200



Y (CM)

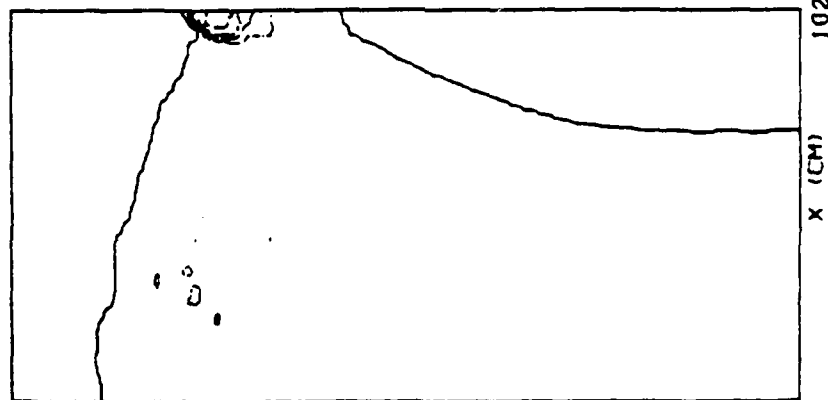
X (CM)

MAX VELOCITY =  $3.24 \cdot 10^{-4}$

PRESSURE CONTOURS

DENSEPACK 18 MEAGATONS

CYCLE= 1701 TIME=  $7.00 \cdot 10^{-4}$   
 2200



Y (CM)

X (CM)

5.00	1.00	1.21	4.57	5.93	7.29	8.65	1.00
10	10	10	10	10	10	10	10

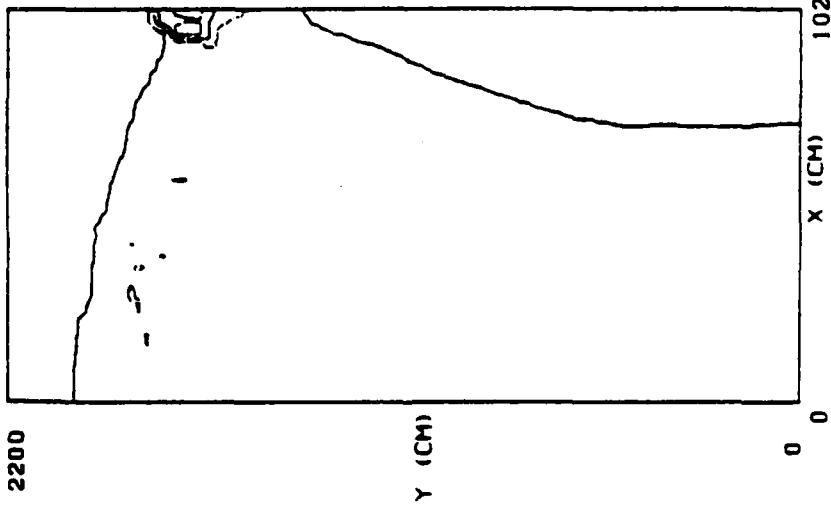
Fig. 3r -- Pressure contours and velocity vectors calculated using FAST2D, shown at intervals of 100 cycles

PRESSURE CONTOURS

DENSEPACK 18 MEAGATONS

CYCLE = 1801

TIME =  $7.47 \cdot 10^{-4}$



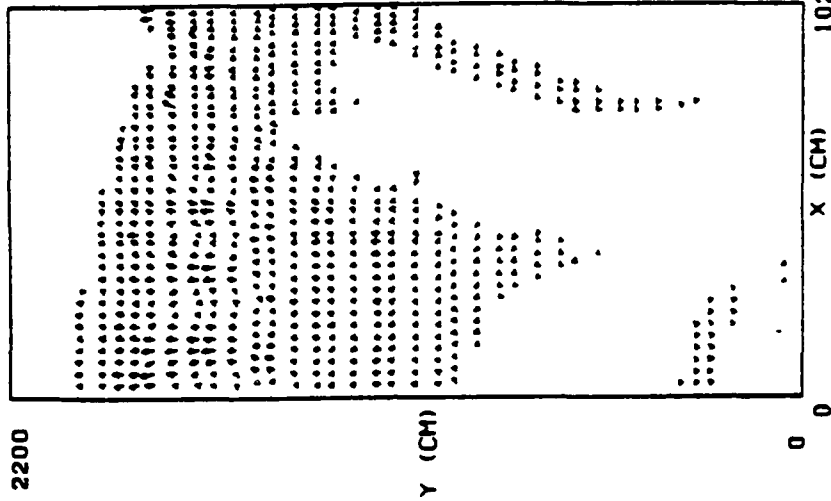
5.00e-10
1.04e-10
1.21e-10
6.57e-10
5.93e-10
7.29e-10
8.41e-10
1.00e-10

VELOCITY VECTORS

DENSEPACK 18 MEAGATONS

CYCLE = 1801

TIME =  $7.47 \cdot 10^{-4}$

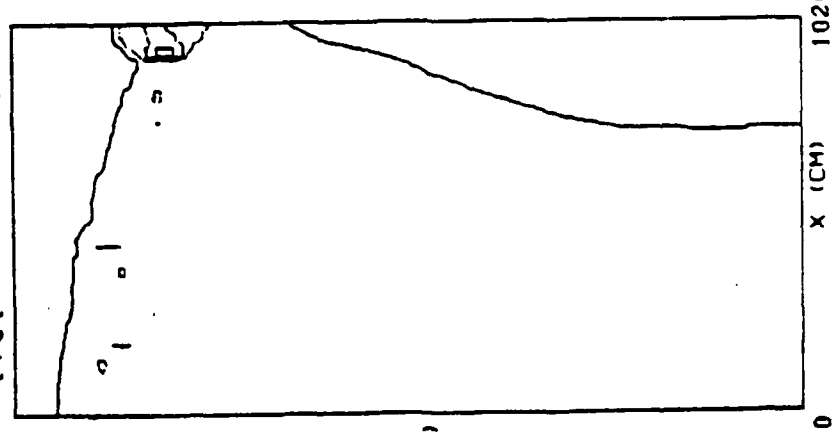


MAX VELOCITY =  $4.53 \cdot 10^{-6}$

Fig. 3s - Pressure contours and velocity vectors calculated using FAST2D, shown at intervals of 100 cycles

**PRESSURE CONTOURS**

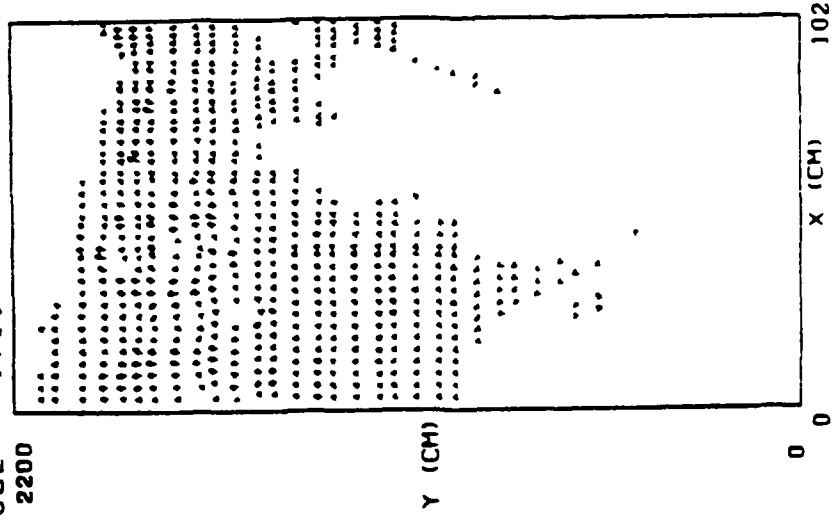
DENSEPACK 18 MEAGATONS  
 CYCLE= 1901 TIME=  $8.05 \cdot 10^{-4}$   
 2200



5.00E-10
1.06E-10
5.21E-10
4.57E-10
5.91E-10
7.39E-10
8.60E-10
1.00E-10

**VELOCITY VECTORS**

DENSEPACK 18 MEAGATONS  
 CYCLE= 1901 TIME=  $8.05 \cdot 10^{-4}$   
 2200



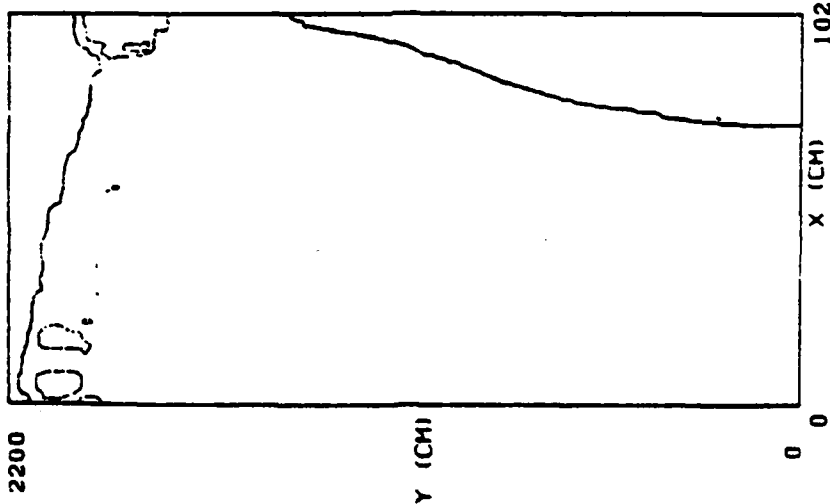
MAX VELOCITY =  $4.85 \cdot 10^{-6}$

Fig. 3t — Pressure contours and velocity vectors calculated using FAST2D, shown at intervals of 100 cycles

PRESSURE CONTOURS

DENSEPACK 18 MEAGATONS

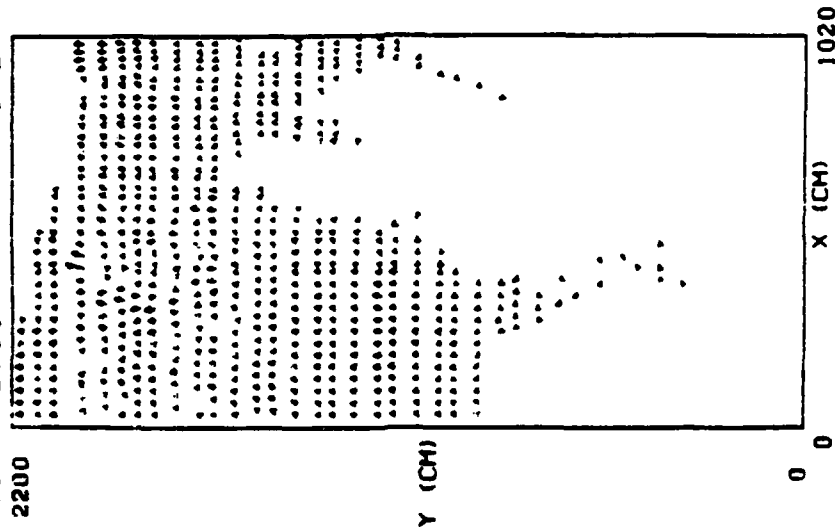
CYCLE= 2001 TIME=  $8.64 \times 10^{-4}$



VELOCITY VECTORS

DENSEPACK 18 MEAGATONS

CYCLE= 2001 TIME=  $8.64 \times 10^{-4}$



5.00*10	0
1.00*10	0
1.21*10	0
0.57*10	0
5.00*10	0
7.30*10	0
8.60*10	0
1.00*10	0

MAX VELOCITY =  $4.60 \times 10^{-4}$

Fig. 3u - Pressure contours and velocity vectors calculated using FAST2D, shown at intervals of 100 cycles

DENSEPACK 18 MEGATONS

PRESS. 3.12-10 TIME 0.00-10

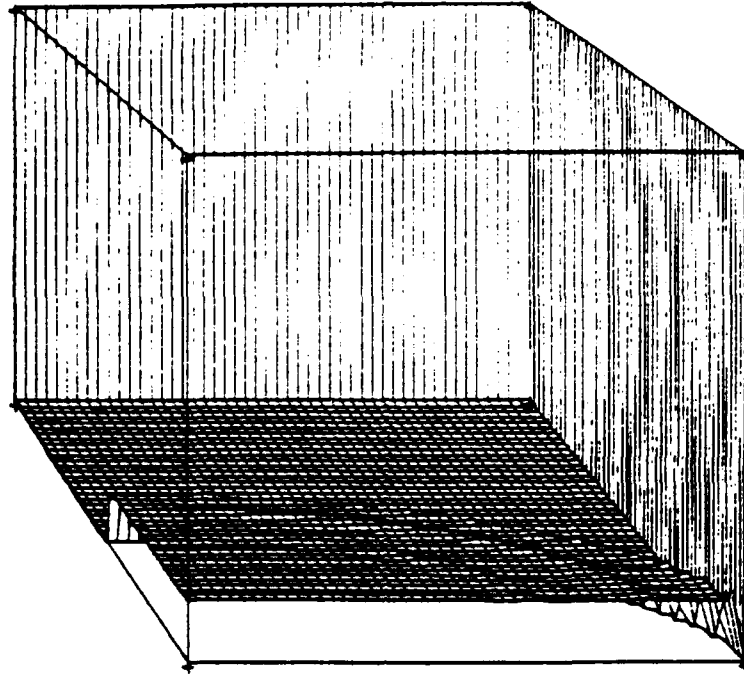


Fig. 4a — Pressure contours of Fig. 3, shown in orthographic projection.  
The pressure scale here is 22 kbar.

DENSEPACK 18 MEGATONS

PRESS. 1.63-10 TIME 5.00-10

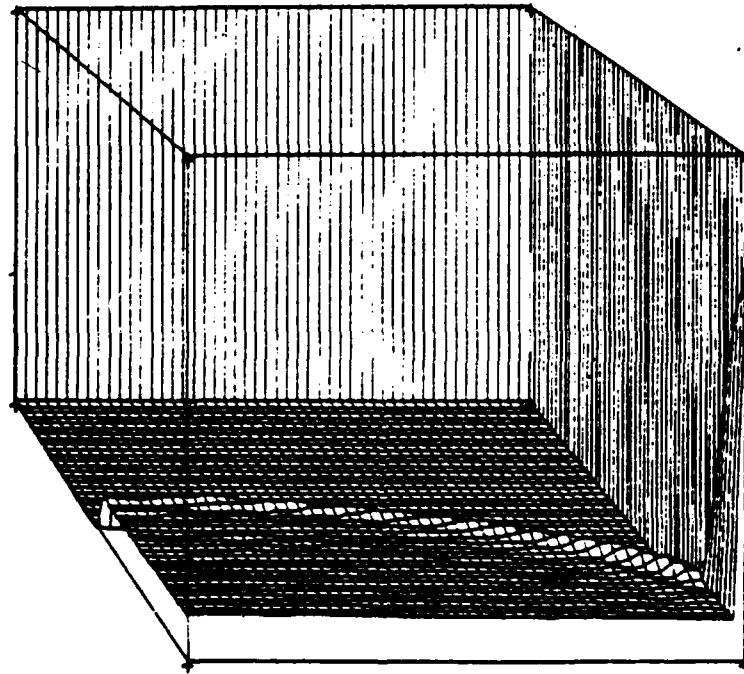


Fig. 4b — Pressure contours of Fig. 3, shown in orthographic projection.  
The pressure scale here is 22 kbar.

DENSEPACK 18 MEGATONS

PRESS.  $1.98 \cdot 10^{10}$

TIME.  $1.21 \cdot 10^{11}$

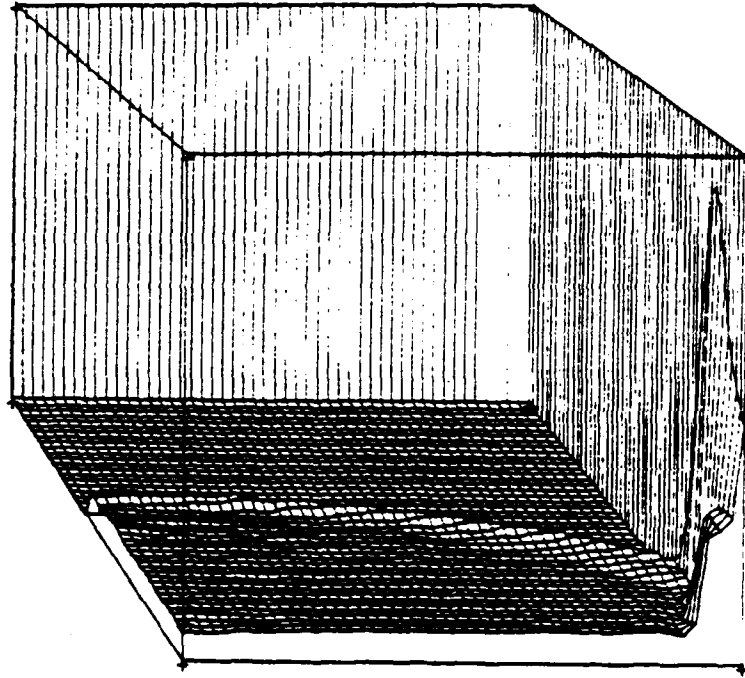


Fig. 4c — Pressure contours of Fig. 3, shown in orthographic projection.  
The pressure scale here is 22 kbar.

DENSEPACK 18 MEGATONS

PRESS.  $1.43 \cdot 10^{10}$

TIME.  $1.79 \cdot 10^{11}$

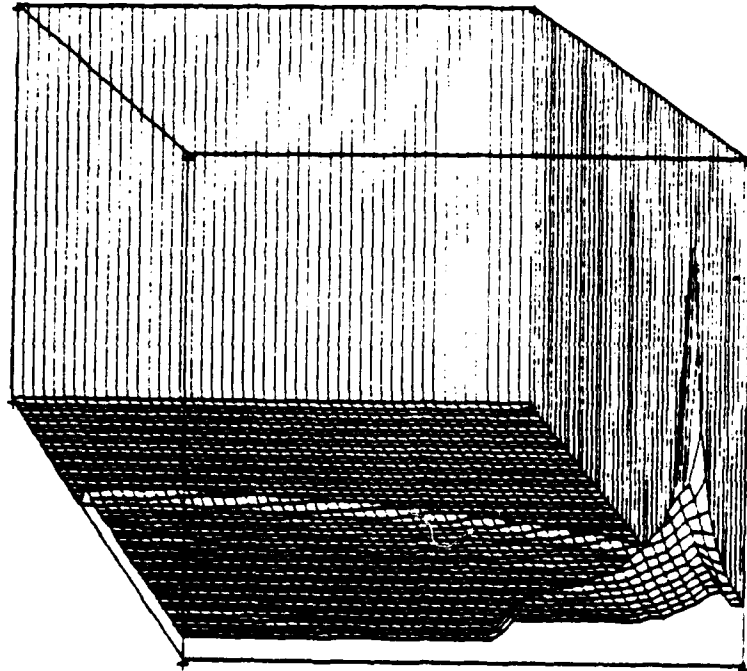


Fig. 4d — Pressure contours of Fig. 3, shown in orthographic projection.  
The pressure scale here is 22 kbar.

DENSEPACK 18 MEGATONS

PRESS.  $1.41 \times 10^{10}$

TIME

$2.29 \times 10^{-6}$

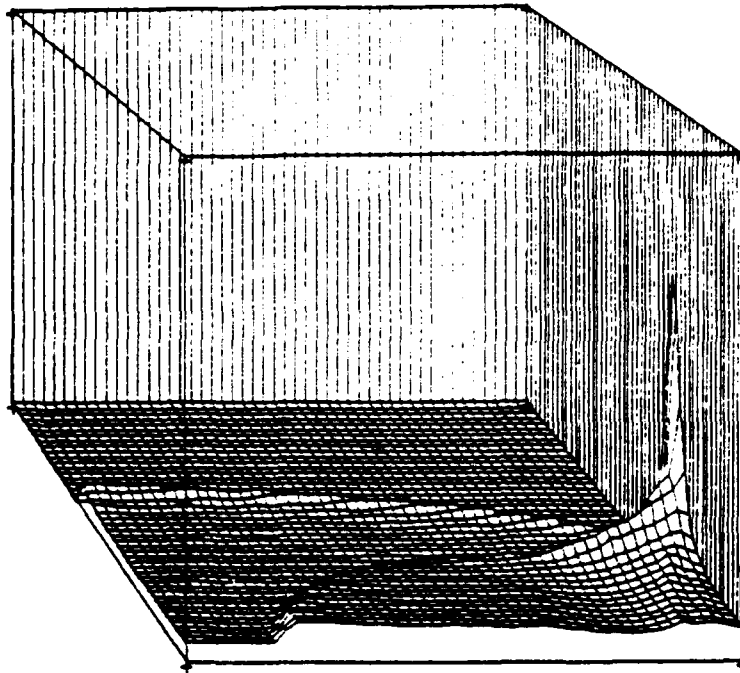


Fig. 4e — Pressure contours of Fig. 3, shown in orthographic projection.  
The pressure scale here is 22 kbar.

DENSEPACK 18 MEGATONS

PRESS.  $1.31 \times 10^{10}$

TIME

$2.67 \times 10^{-6}$

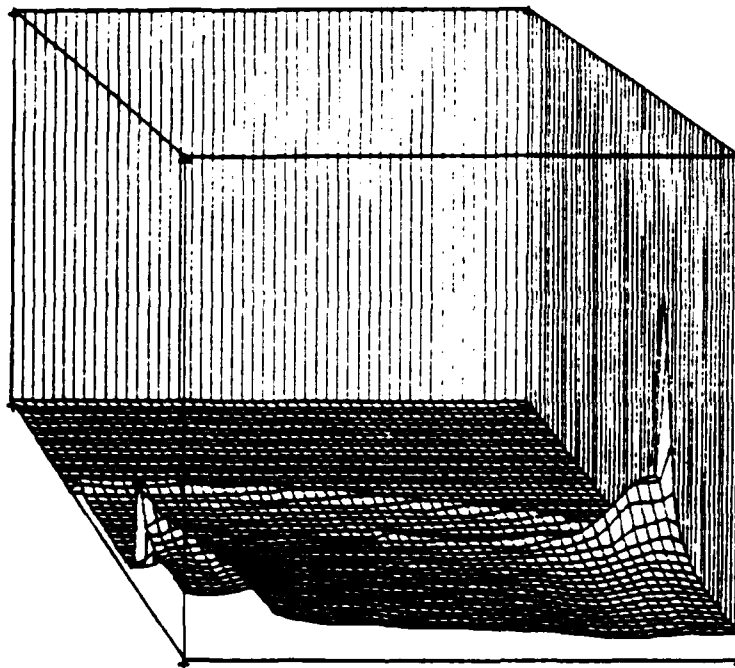


Fig. 4f — Pressure contours of Fig. 3, shown in orthographic projection.  
The pressure scale here is 22 kbar.

DENSEPACK 18 MEGATONS

PRESS.  $1.20 \cdot 10^{10}$

TIME.

$2.98 \cdot 10^{-4}$

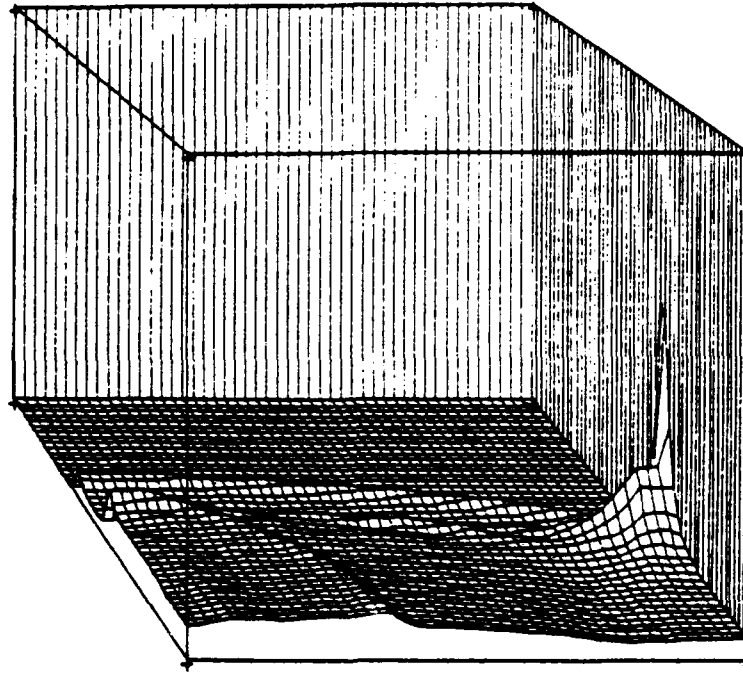


Fig. 4g — Pressure contours of Fig. 3, shown in orthographic projection.  
The pressure scale here is 22 kbar.

DENSEPACK 18 MEGATONS

PRESS.  $1.11 \cdot 10^{10}$

TIME.

$3.34 \cdot 10^{-4}$

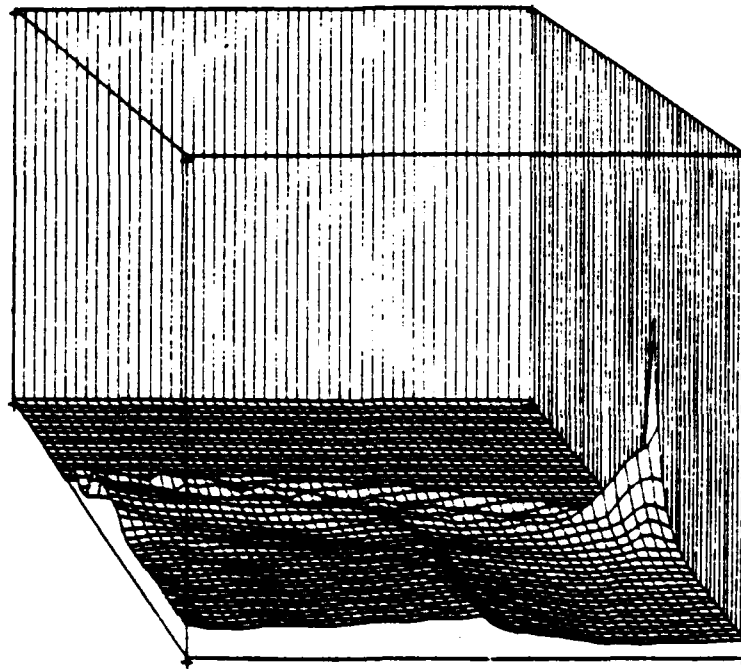


Fig. 4h — Pressure contours of Fig. 3, shown in orthographic projection.  
The pressure scale here is 22 kbar.

DENSEPACK 18 MEGATONS

PRESS. 1.00-10<sup>10</sup>

TIME. 3.62-10<sup>-7</sup>

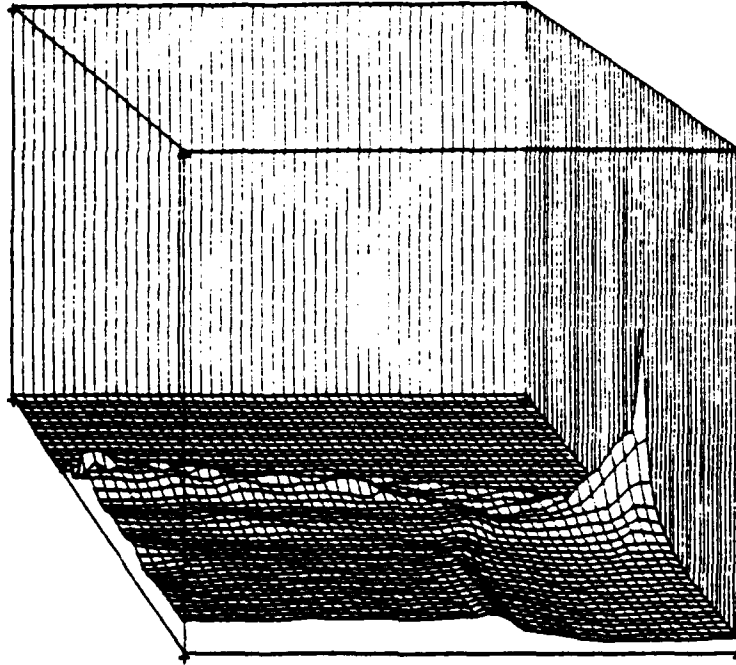


Fig. 4i — Pressure contours of Fig. 3, shown in orthographic projection.  
The pressure scale here is 22 kbar.

DENSEPACK 18 MEGATONS

PRESS. 1.01-10<sup>10</sup>

TIME. 3.83-10<sup>-7</sup>

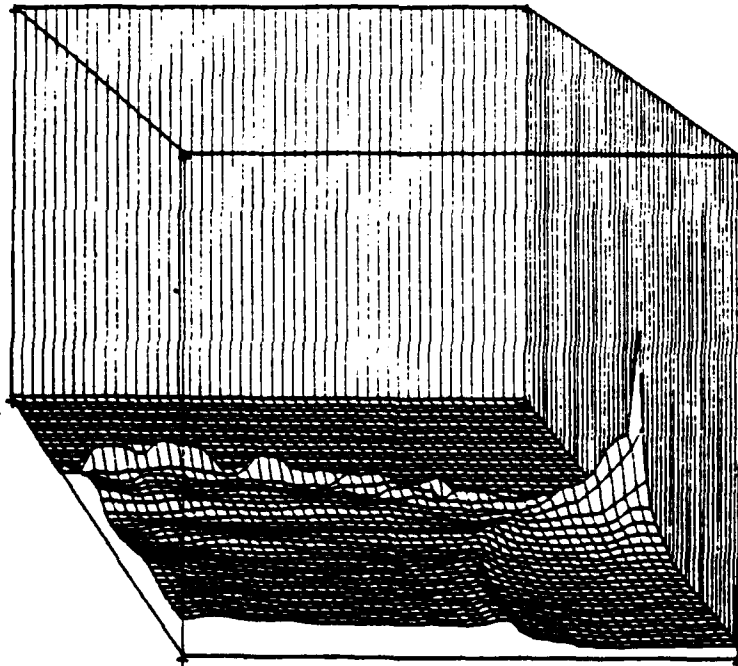


Fig. 4j — Pressure contours of Fig. 3, shown in orthographic projection.  
The pressure scale here is 22 kbar.

DENSEPACK 18 MEGATONS

PRESS•  $1.07 \cdot 10^{10}$

TIME•

$4.06 \cdot 10^{-7}$

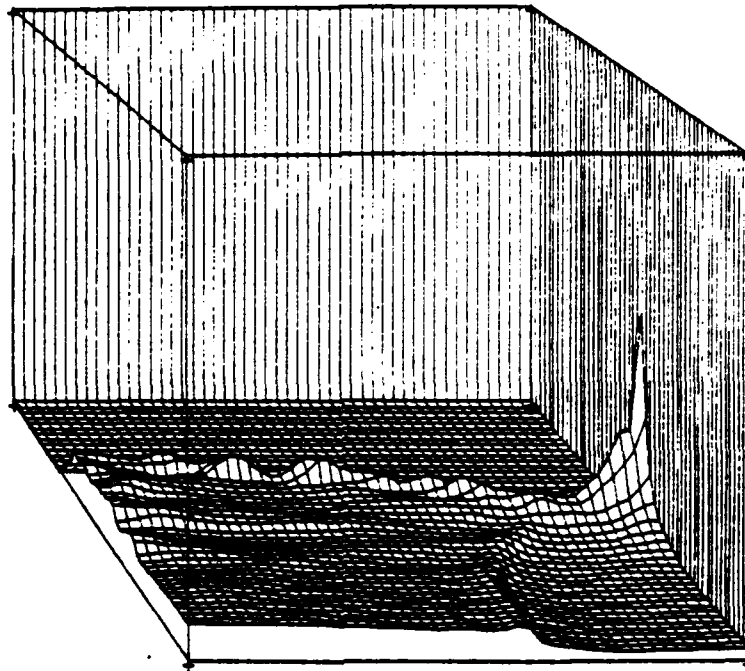


Fig. 4k — Pressure contours of Fig. 3, shown in orthographic projection.  
The pressure scale here is 22 kbar.

DENSEPACK 18 MEGATONS

PRESS•  $1.21 \cdot 10^{10}$

TIME•

$4.39 \cdot 10^{-7}$

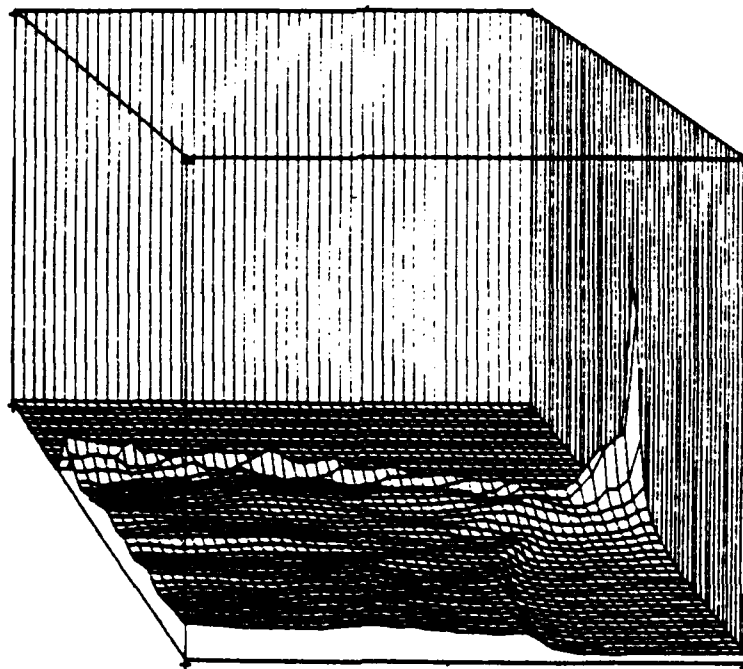


Fig. 4l — Pressure contours of Fig. 3, shown in orthographic projection.  
The pressure scale here is 22 kbar.

DENSEPACK 18 MEGATONS

PRESS.  $1.19 \cdot 10^{10}$

TIME

$4.66 \cdot 10^{-4}$

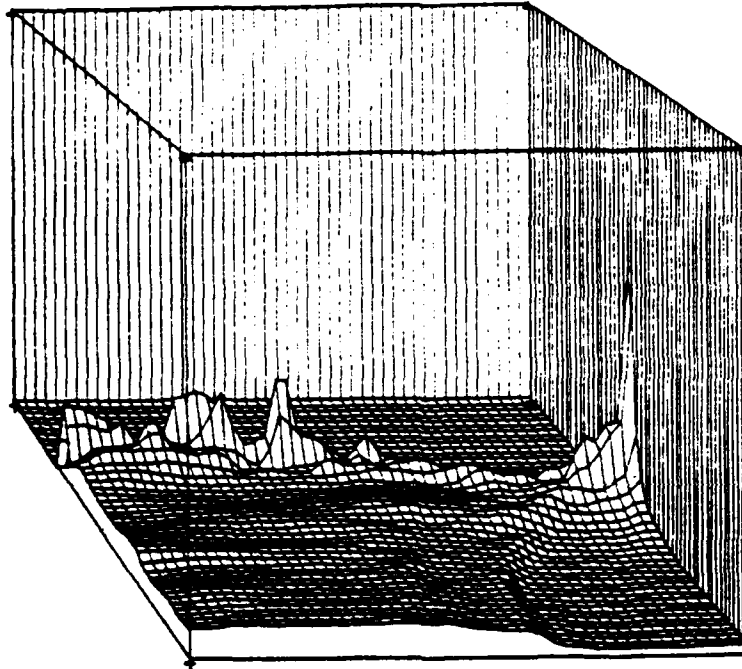


Fig. 4m — Pressure contours of Fig. 3, shown in orthographic projection.  
The pressure scale here is 22 kbar.

DENSEPACK 18 MEGATONS

PRESS.  $1.06 \cdot 10^{10}$

TIME

$5.02 \cdot 10^{-4}$

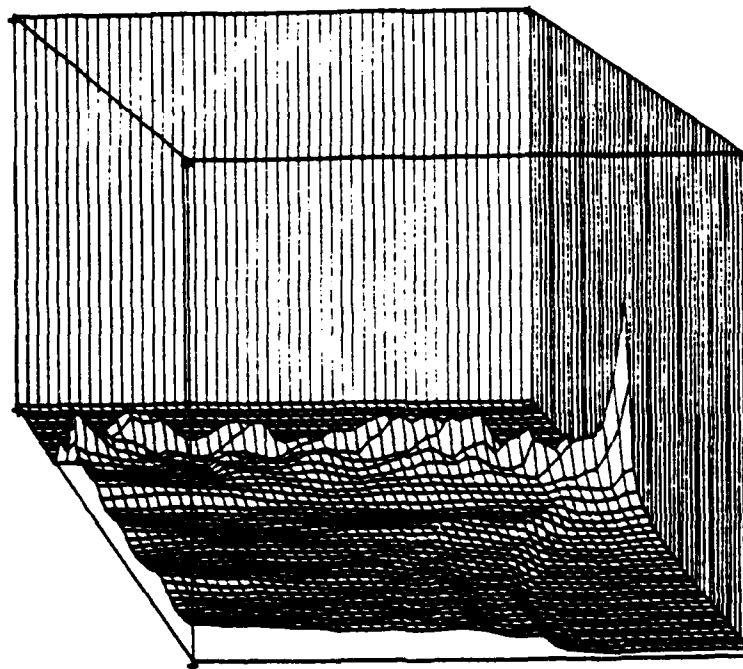


Fig. 4n — Pressure contours of Fig. 3, shown in orthographic projection.  
The pressure scale here is 22 kbar.

DENSEPACK 18 MEGATONS

PRESS. 8.56-10 °

TIME •

5.51-10<sup>-7</sup>

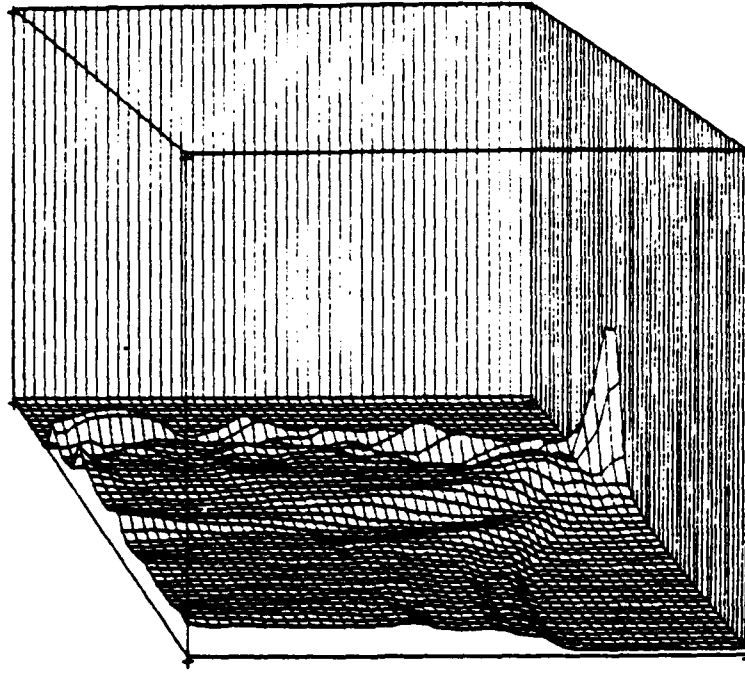


Fig. 4o — Pressure contours of Fig. 3, shown in orthographic projection.  
The pressure scale here is 22 kbar.

DENSEPACK 18 MEGATONS

PRESS. 8.25-10 °

TIME •

6.01-10<sup>-7</sup>

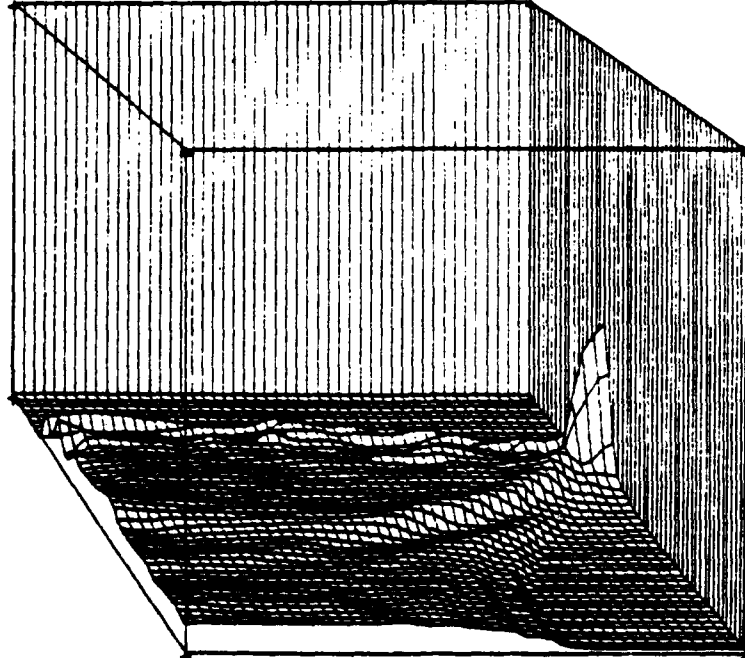


Fig. 4p — Pressure contours of Fig. 3, shown in orthographic projection.  
The pressure scale here is 22 kbar.

DENSEPACK 18 MEGATONS  
PRESS. 7.11-10 TIME. 6.50-10

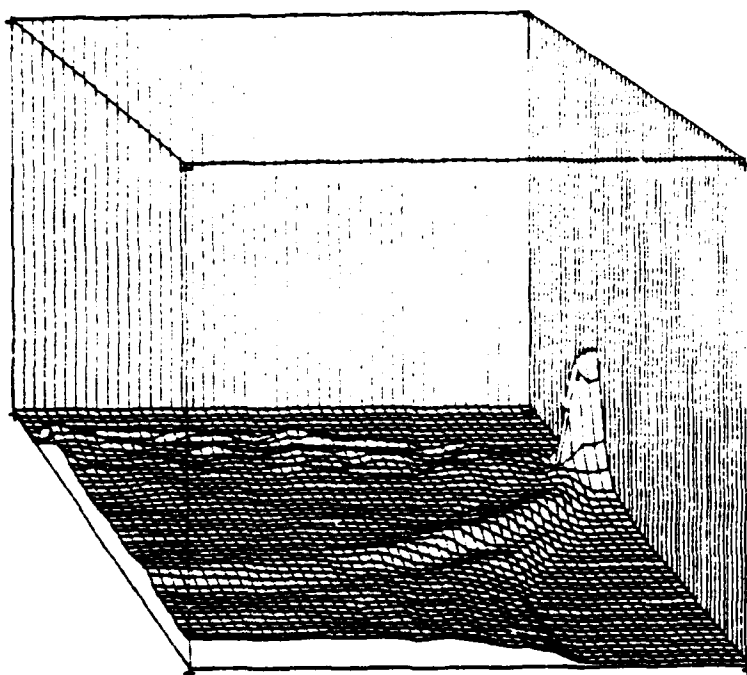


Fig. 4q — Pressure contours of Fig. 3, shown in orthographic projection.  
The pressure scale here is 22 kbar.

DENSEPACK 18 MEGATONS  
PRESS. 6.28-10 TIME. 7.00-10

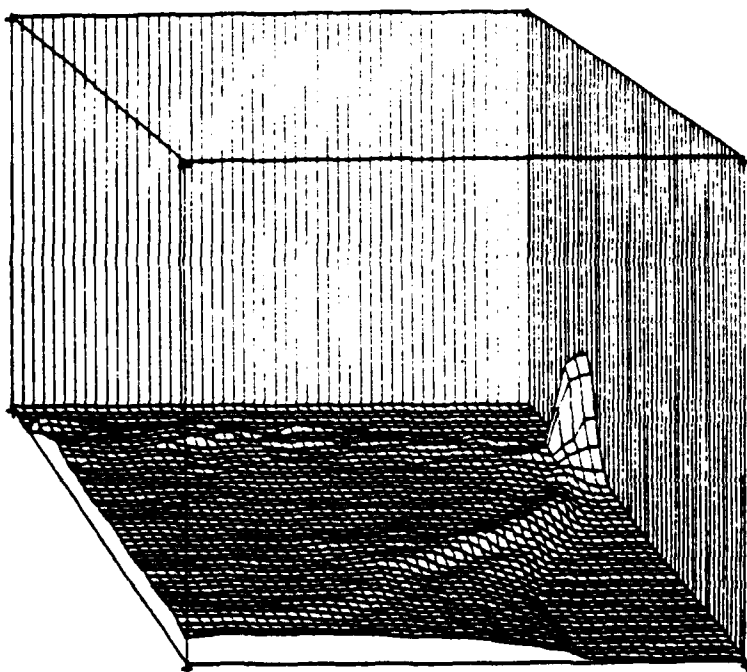


Fig. 4r — Pressure contours of Fig. 3, shown in orthographic projection.  
The pressure scale here is 22 kbar.

DENSEPACK 18 MEGATONS

PRESS.  $4.92 \cdot 10^7$  TIME  $7.47 \cdot 10^{-7}$

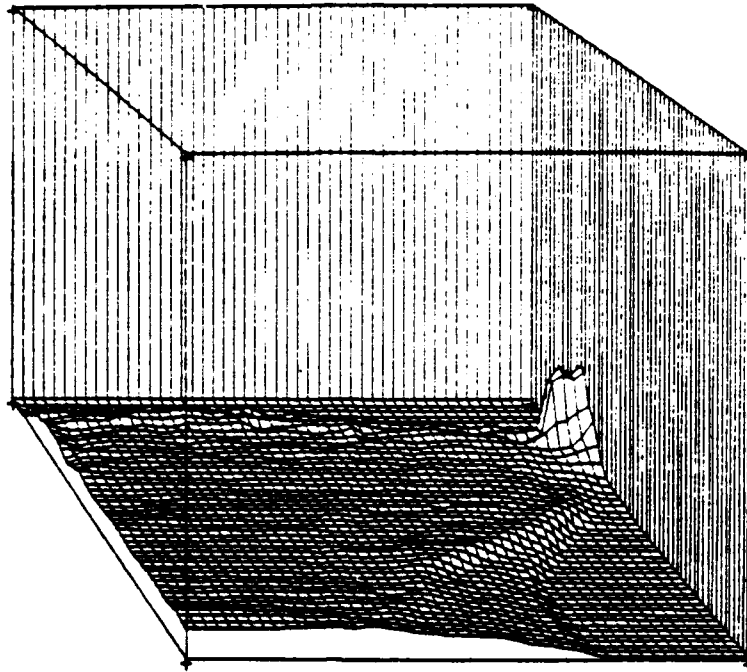


Fig. 4s — Pressure contours of Fig. 3, shown in orthographic projection. The pressure scale here is 22 kbar.

DENSEPACK 18 MEGATONS

PRESS.  $4.67 \cdot 10^7$  TIME  $8.05 \cdot 10^{-7}$

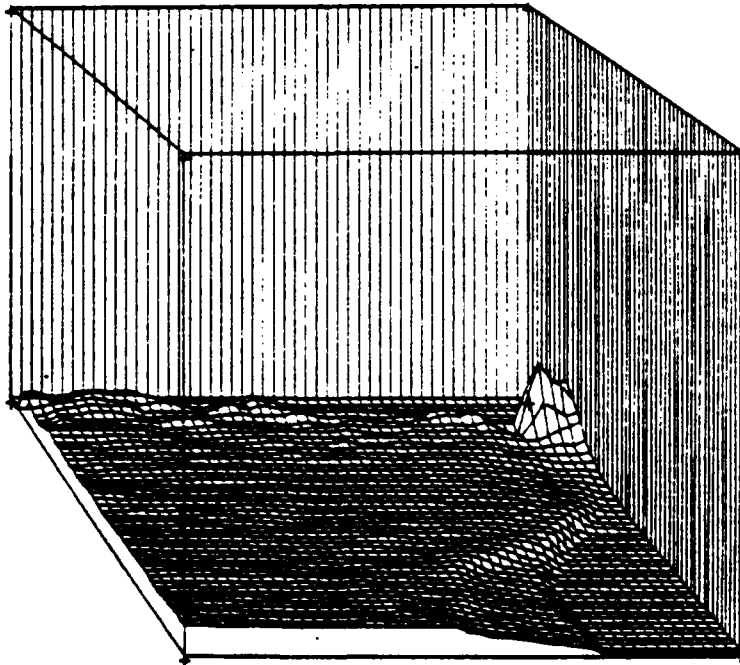


Fig. 4t — Pressure contours of Fig. 3, shown in orthographic projection. The pressure scale here is 22 kbar.

DENSEPACK 18 MEADATONS

PRESS • 3.34 • 10 •

TIME •

8.64 • 10 •

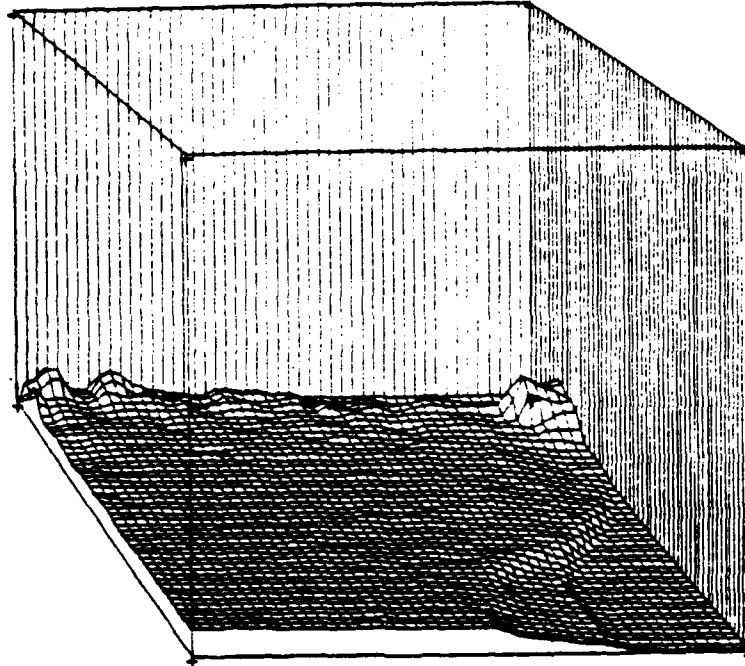


Fig. 4u — Pressure contours of Fig. 3, shown in orthographic projection.  
The pressure scale here is 22 kbar.

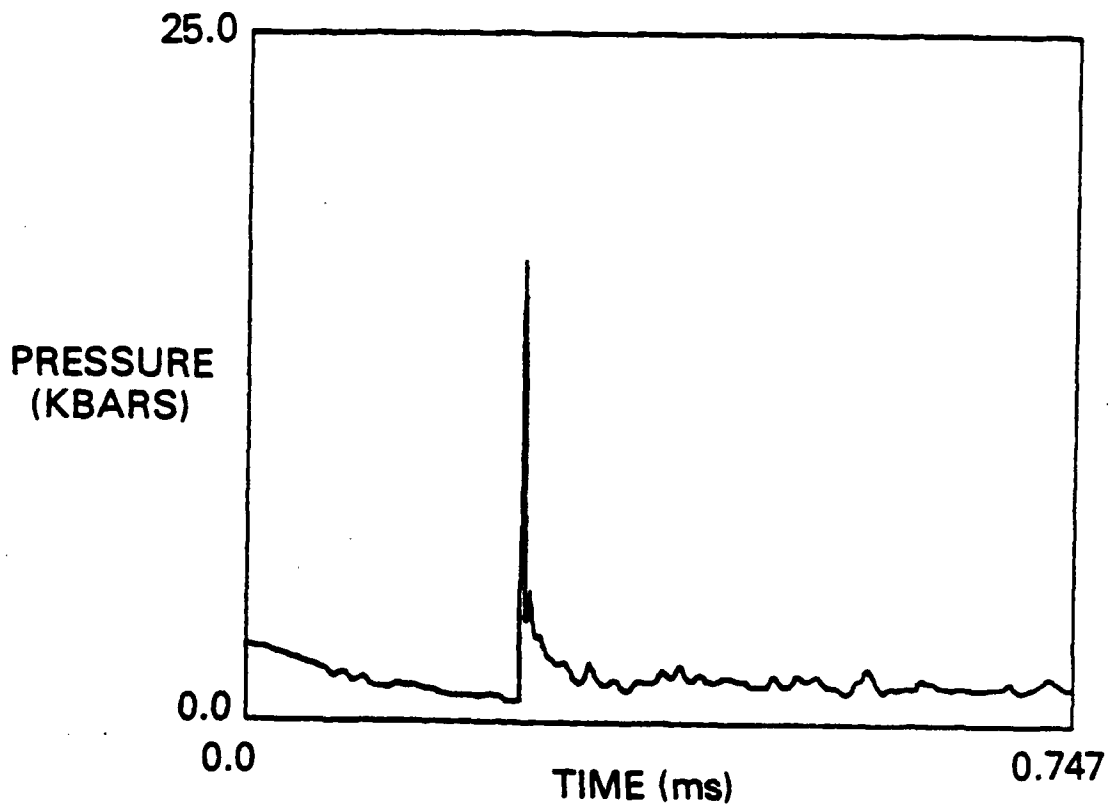


Fig. 5a — Pressure histories as measured by sensors located at radii of 0.0m

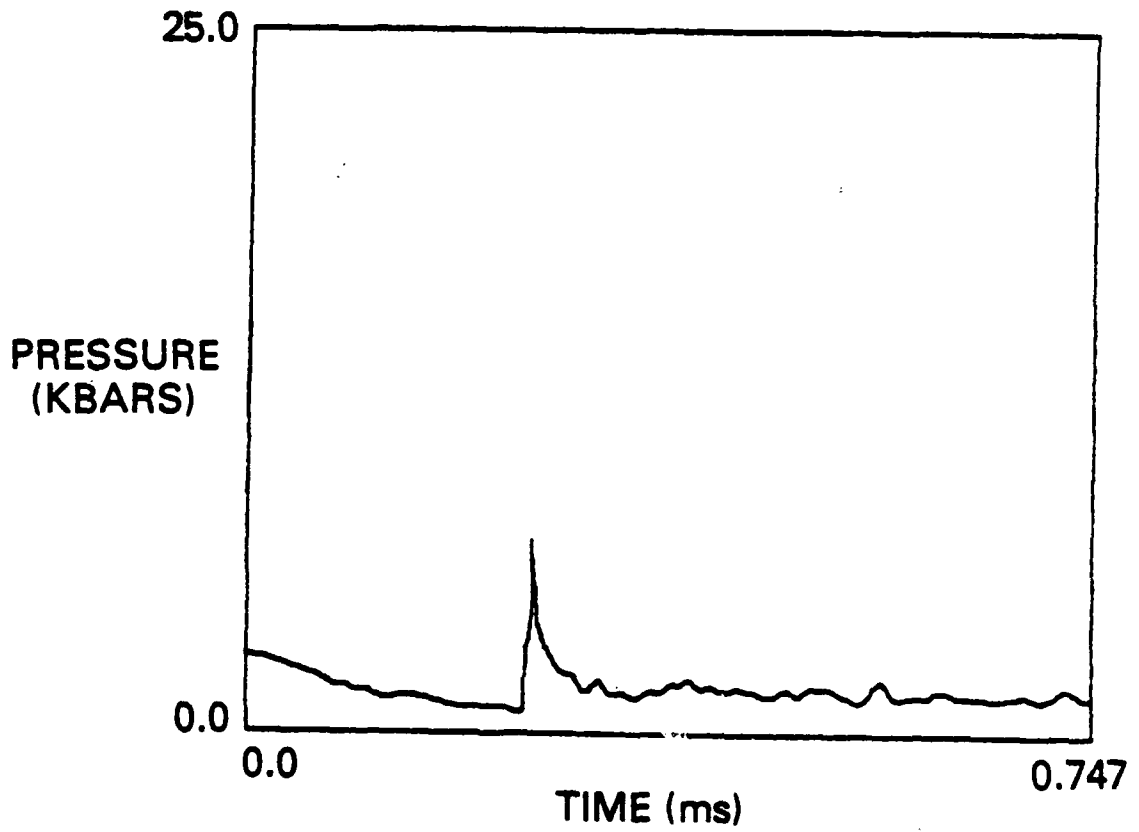


Fig. 5b — Pressure histories as measured by sensors located at radii of 0.035m

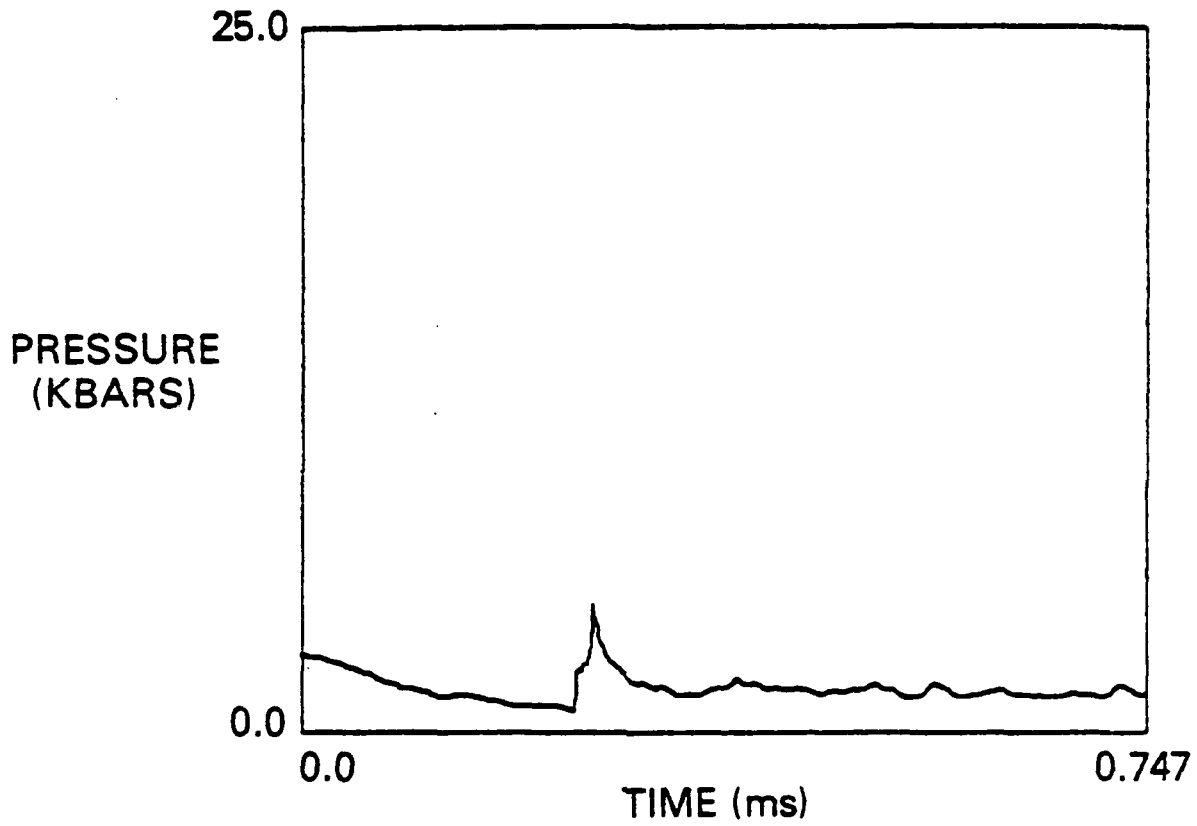


Fig. 5c — Pressure histories as measured by sensors located at radii of 0.075m

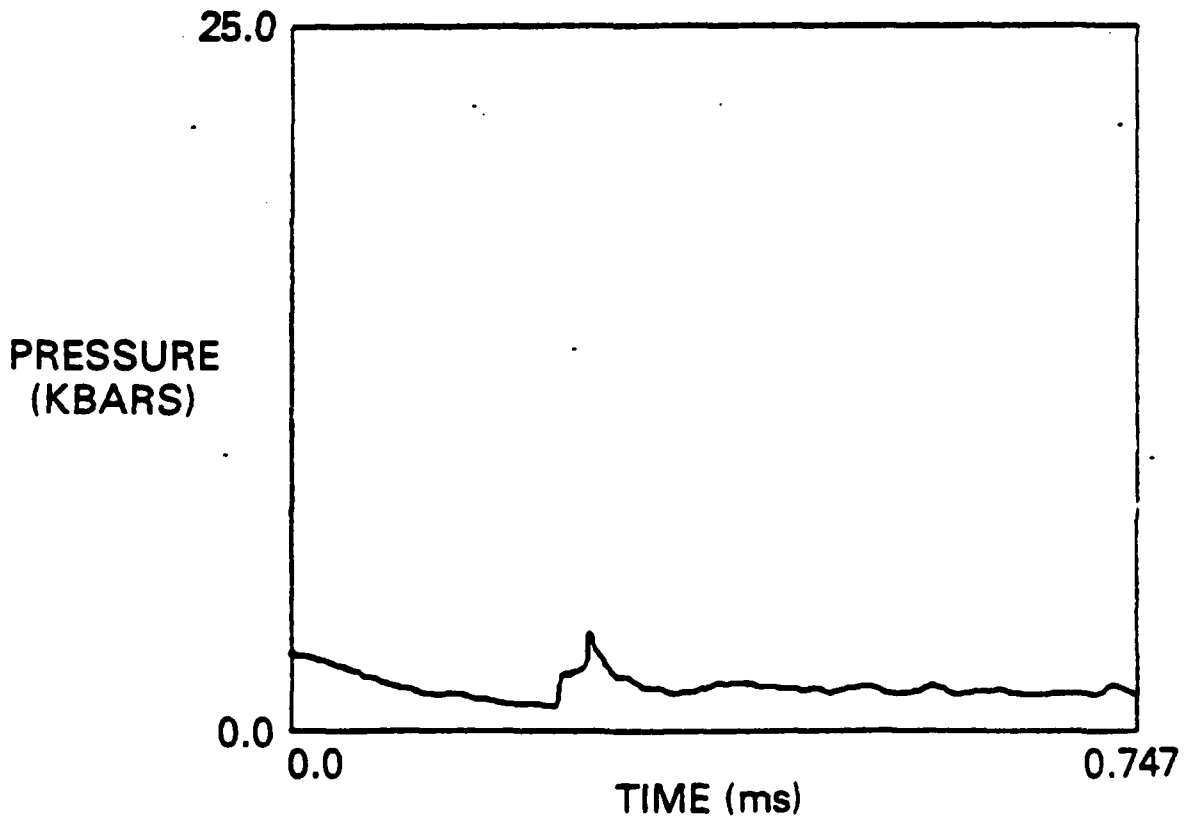


Fig. 5d — Pressure histories as measured by sensors located at radii of 1.25m

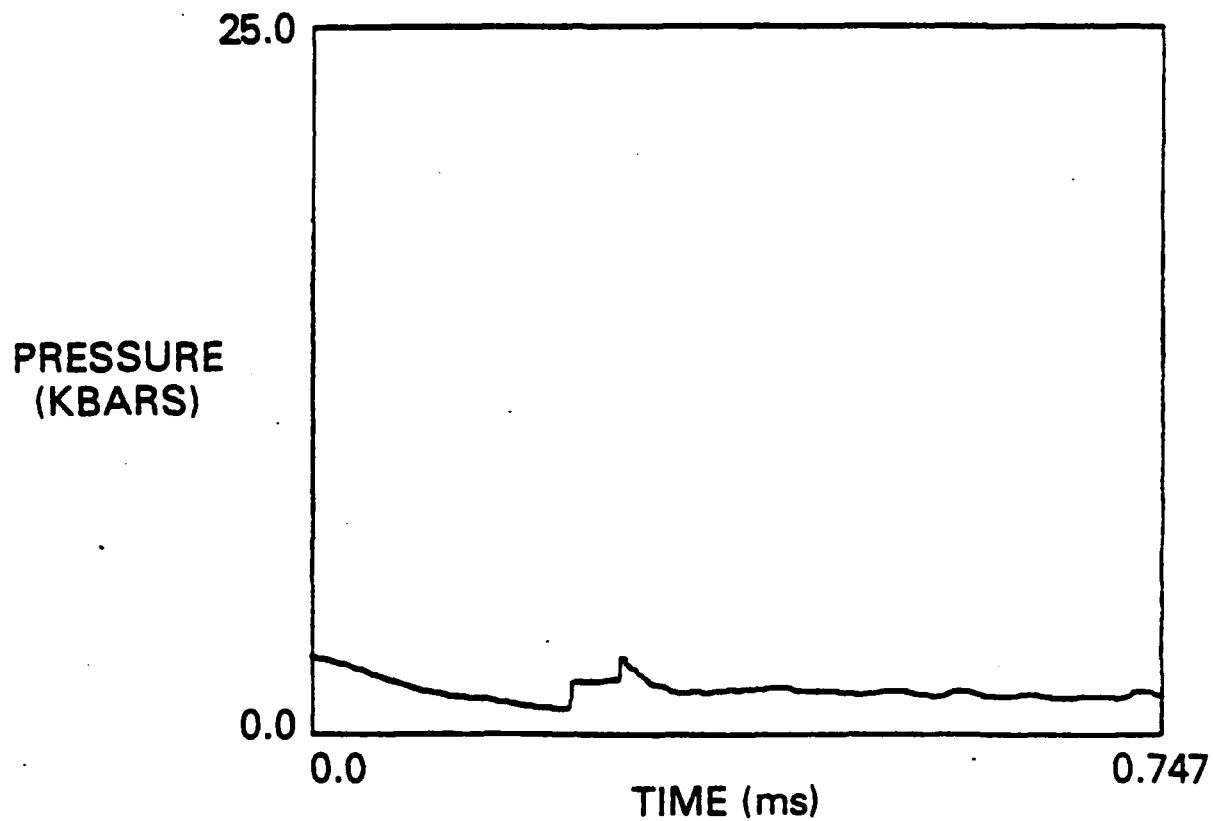


Fig. 5e - Pressure histories as measured by sensors located at radii of 2.0m

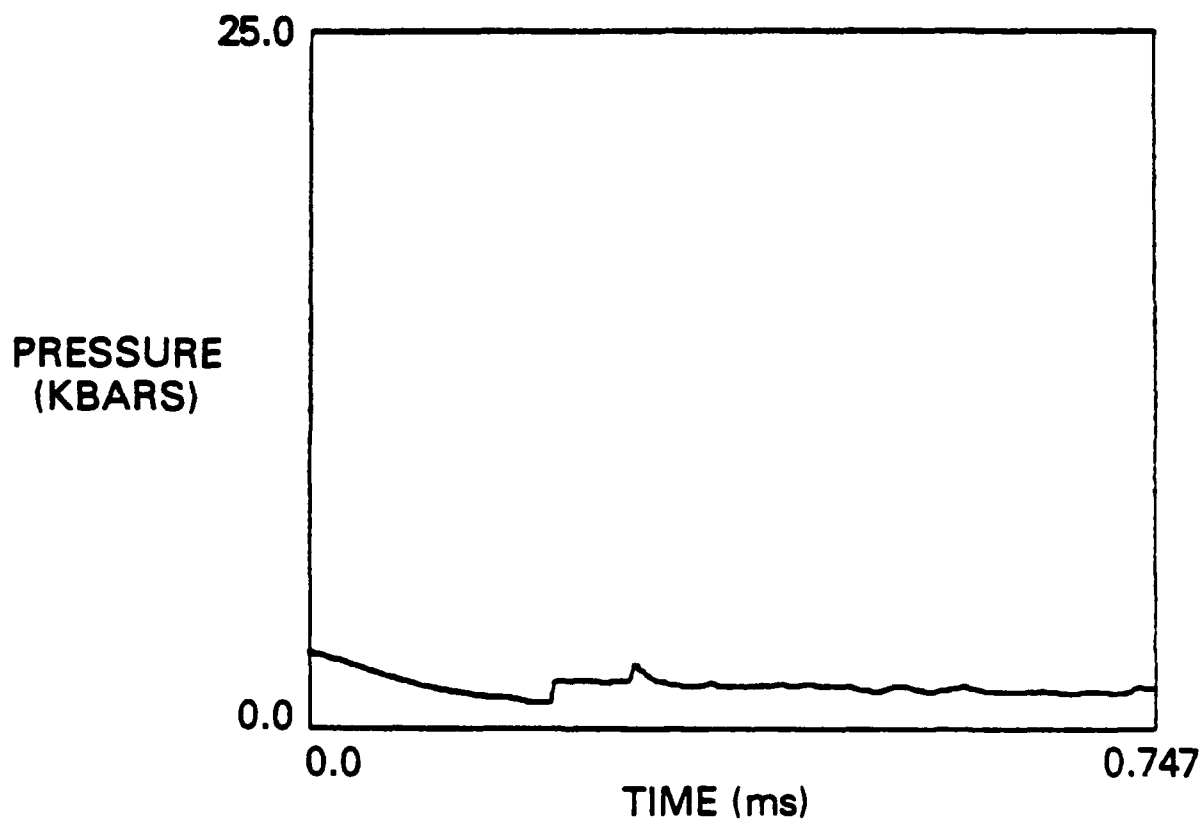


Fig. 5f - Pressure histories as measured by sensors located at radii of 3.0m

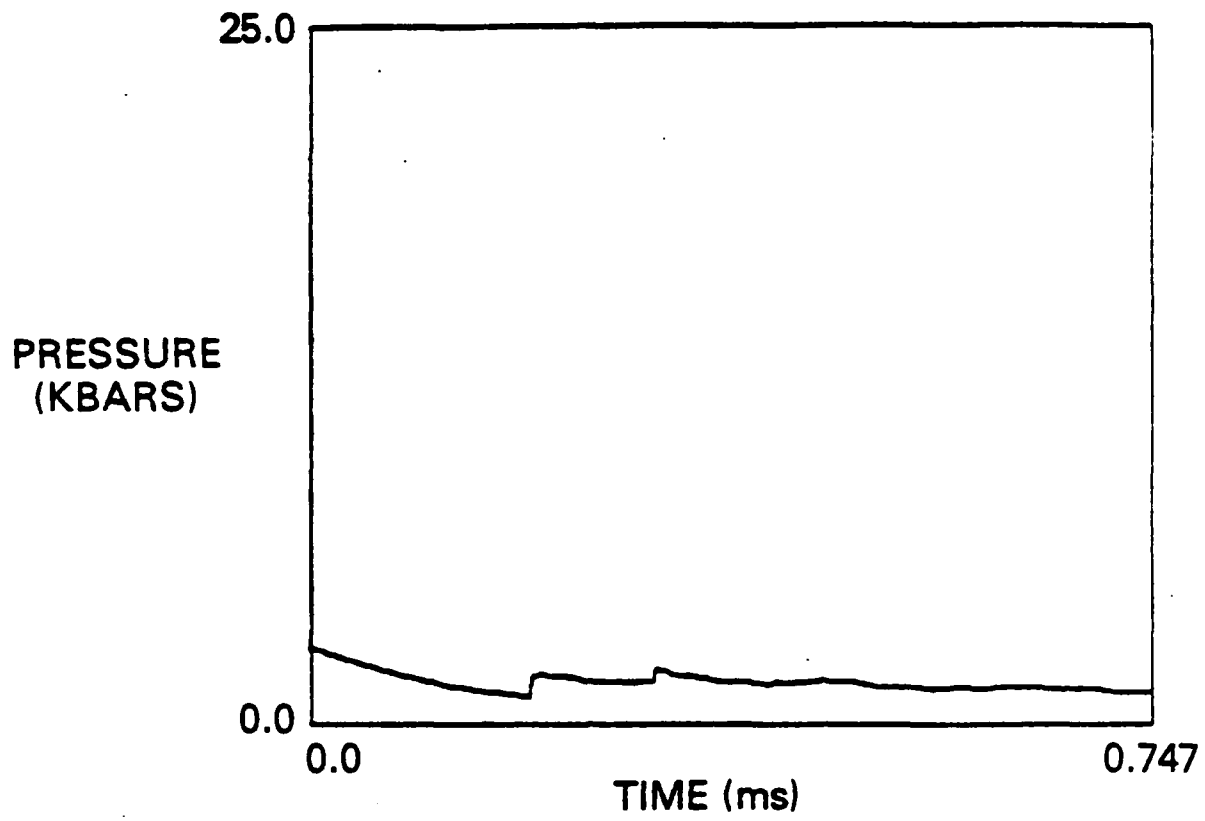


Fig. 5g — Pressure histories as measured by sensors located at radii of 4.5m

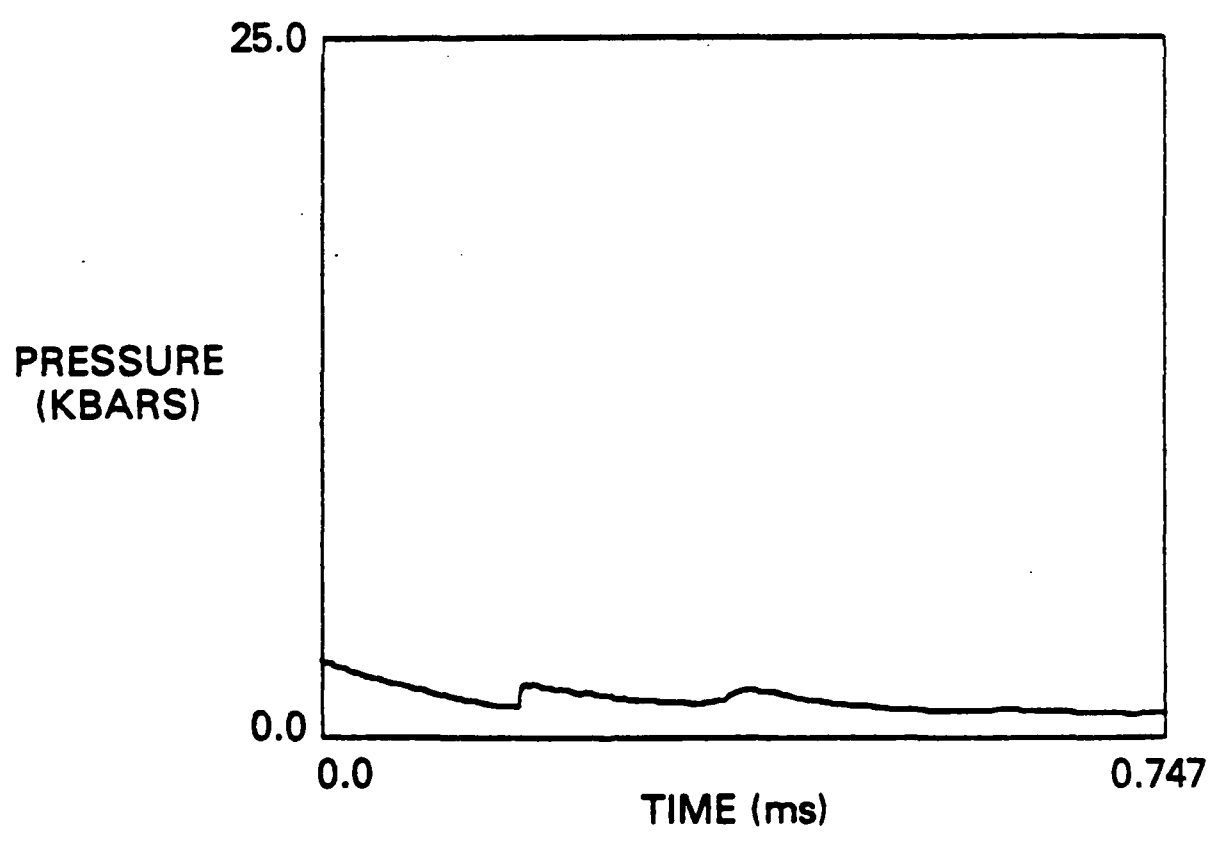


Fig. 5h — Pressure histories as measured by sensors located at radii of 6.05m

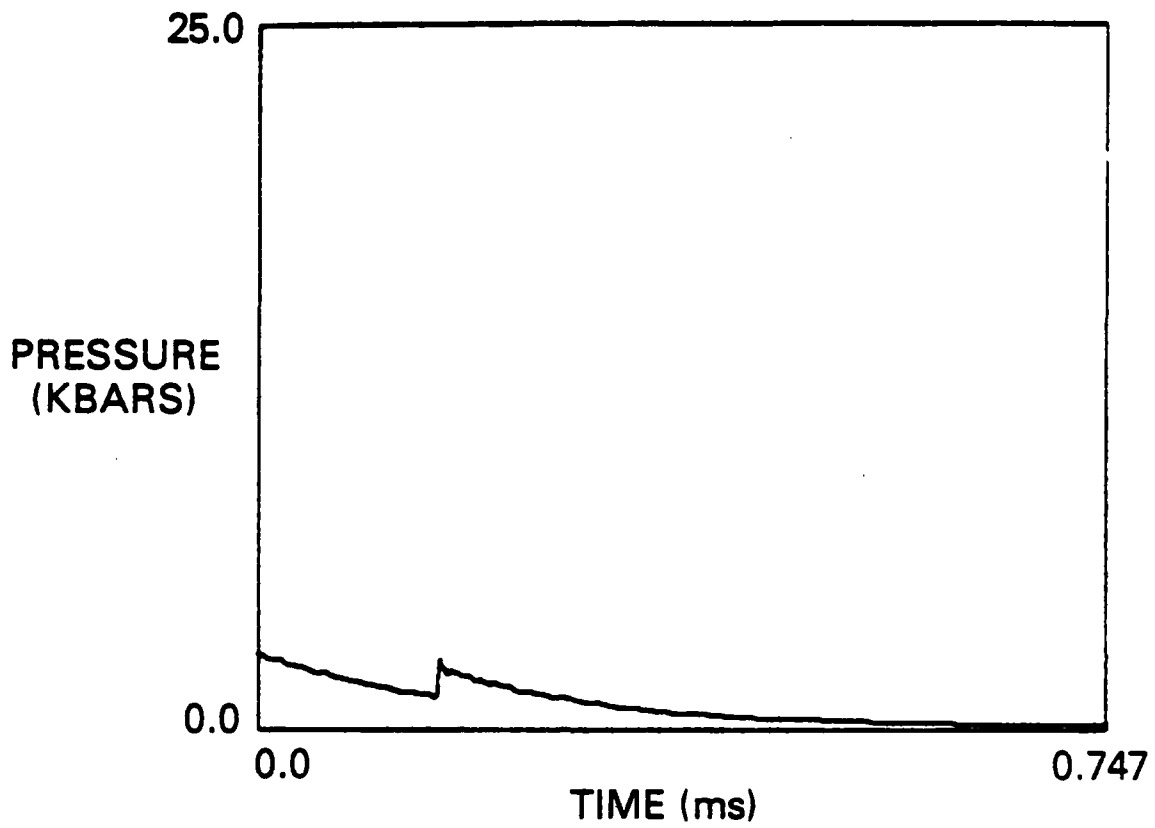


Fig. 5i — Pressure histories as measured by sensors located at radii of 7.5m

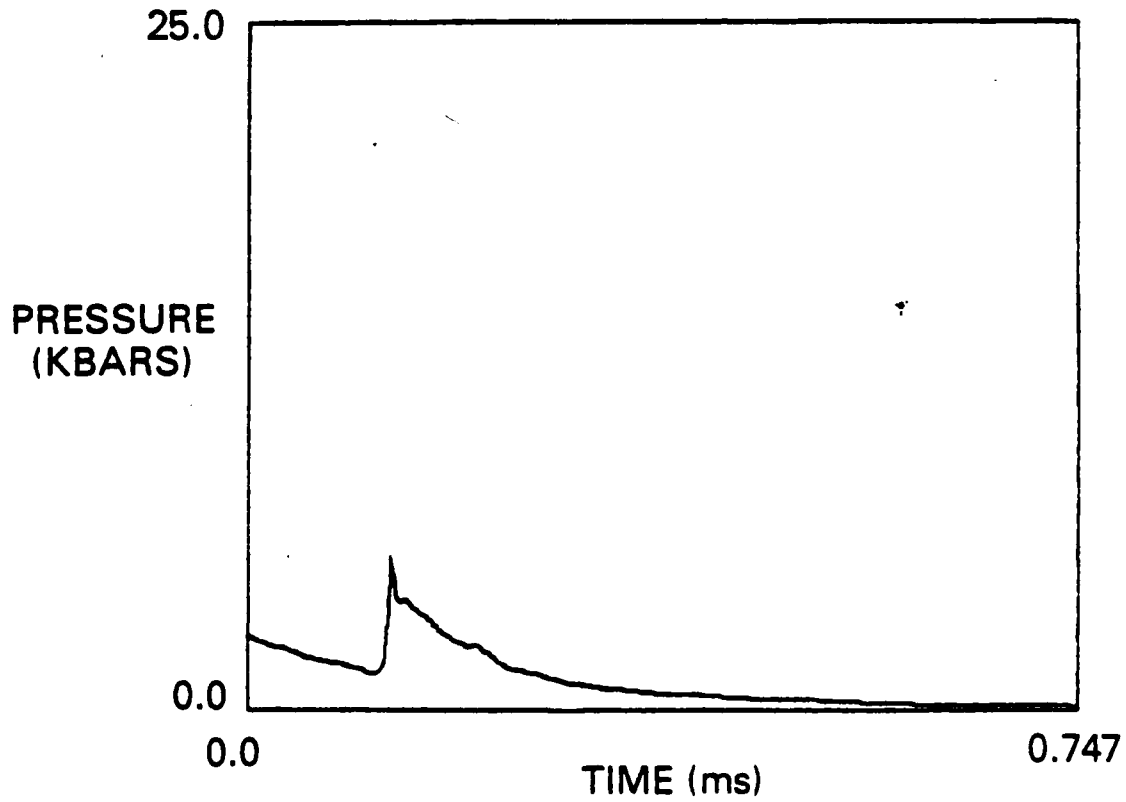


Fig. 5j — Pressure histories as measured by sensors located at radii of 9.25m

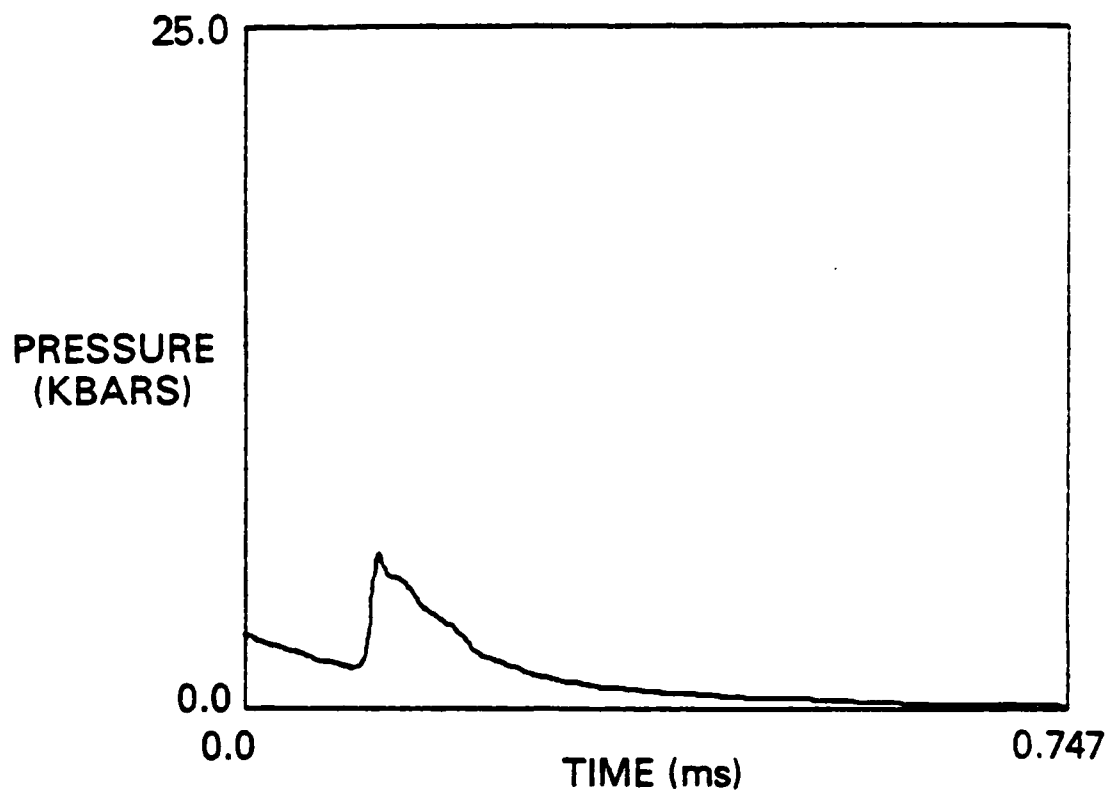


Fig. 5k - Pressure histories as measured by sensors located at radii of 9.5m

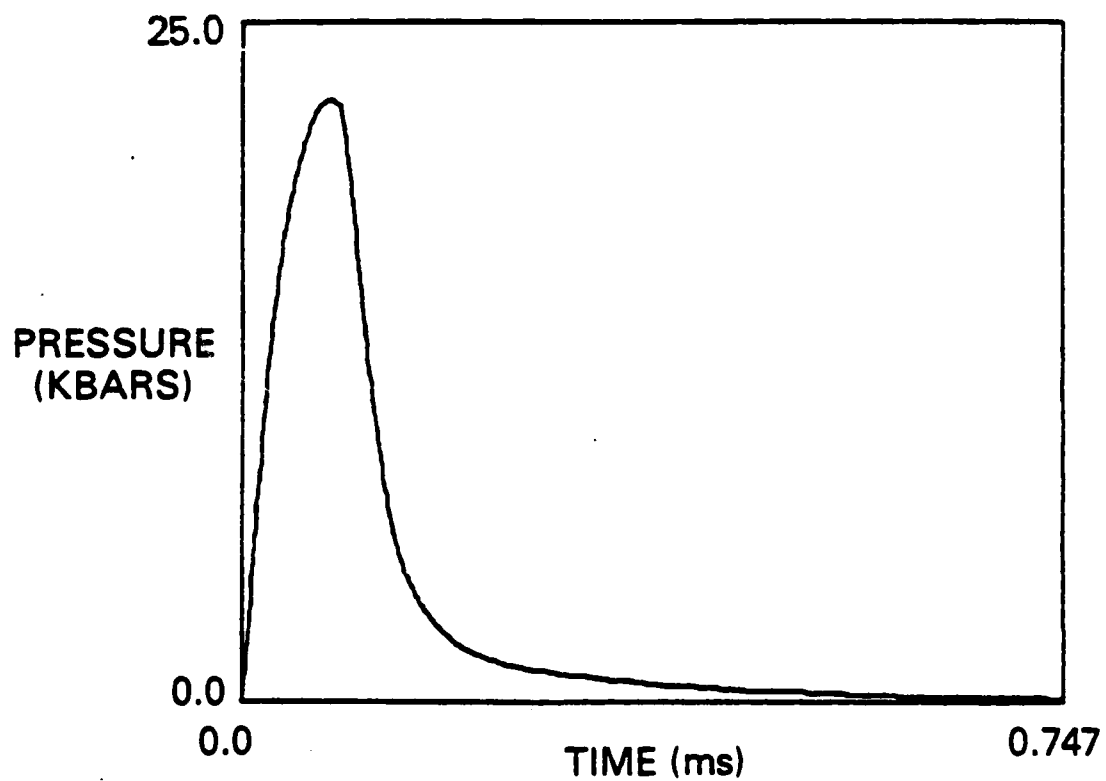


Fig. 5l - Pressure histories as measured by sensors located at radii of 10.0m

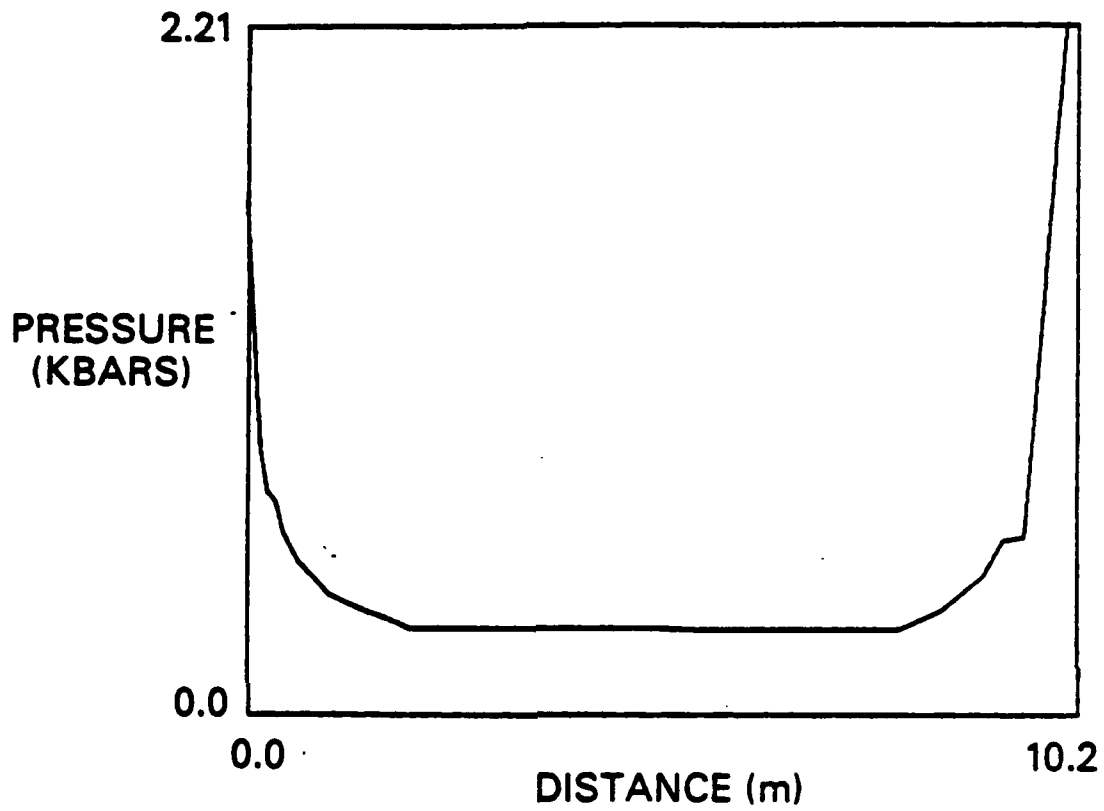


Fig. 6 — Maximum recorded station pressure in kbar as function of station radial location

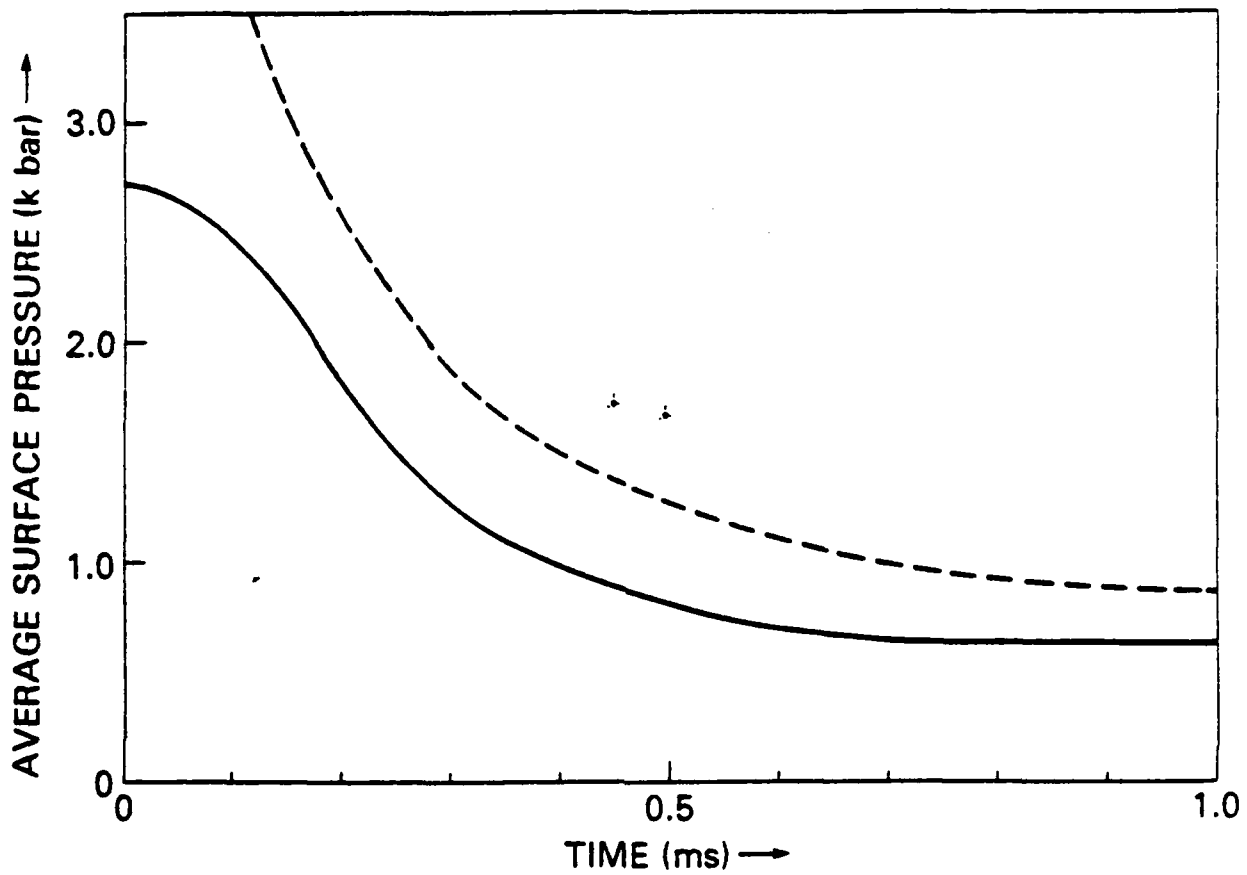


Fig. 7 — Average pressure on floor of mesh (solid curve) and pressure at origin calculated from Sedov one-dimensional self-similar solution with  $\gamma = 1.2$  (broken curve) as functions of time

## REFERENCES

1. Latter, Albert (1982, unpublished).
2. Sedov, L. I., Similarity and Dimensional Methods in Mechanics, Academic Press, New York (1959), p. 220.
3. Fry, M. A., Picone, J. M., Boris, J. P., and Book, D. B., "Transition to Double Mach Stem for Nuclear Explosion at 104FT Height of Burst", NRL Memorandum Report #4630 (1981).
4. Carpenter, H. J., "Height-of-Burst Blast at High Overpressure," 4th International Symposium on Military Applications of Blast Simulation (1974).
5. Pyatt, K., CSB Review Meeting, DNA Headquarters, October 13, 1982.

APPENDIX C  
LIMITATIONS ON THE APPLICABILITY OF HIGH-EXPLOSIVE  
CHARGES FOR SIMULATING NUCLEAR AIRBLAST



## 20. ABSTRACT (Continued)

Flux-Corrected Transport hydrocodes in one and two dimensions. The principal difference in the free-field solutions are the presence in the HE case of a contact discontinuity between air and HE products and of a backward-facing shock behind it. Temperatures in the nuclear fireball are initially three orders of magnitude higher; correspondingly, the density minimum at the center of the fireball is much broader and deeper. When the blast wave in a nuclear height-of-burst (HOB) situation undergoes regular reflections from the ground only one peak develops in the overpressure, and the reflected wave propagates upward rapidly through the hot underdense fireball. In the HE case part of the upward-moving reflected wave is reflected downward at the contact surface, producing a second pressure peak on the ground, while the shock transmitted through the contact surface propagates slowly upward. After transition to Mach reflection other differences appear. At late times following shock breakaway the nuclear fireball, unlike the HE fireball, appears to develop a Rayleigh-Taylor instability along its lower edge below the HOB. The vortices (both forward and reverse) are stronger and form earlier. This has important consequences for fireball rise and for dust entrainment and transport to high altitudes.

## CONTENTS

Section 1 — INTRODUCTION .....	2
Section 2 — NUMERICAL TREATMENT .....	4
Section 3 — FREE-FIELD SOLUTION .....	7
Section 4 — 2D SIMULATION OF AIRBLAST .....	11
Section 5 — CONCLUSIONS .....	22
REFERENCES .....	23
ACKNOWLEDGMENT .....	24

LIMITATIONS ON THE APPLICABILITY OF HIGH-EXPLOSIVE CHARGES  
FOR SIMULATING NUCLEAR AIRBLAST

D. Book, D. Fyfe, M. Picone, Naval Research Laboratory,  
Washington, D.C.

M. Fry, Science Applications, Inc., McLean, Virginia

The flow fields that result from nuclear and high explosive (HE) detonations are qualitatively alike but quantitatively different. Consequently, care must be exercised in carrying over conclusions drawn from measurements of HE tests to nuclear explosions. The usefulness of HE explosions for simulating nuclear airblast is predicated on the fact that after reaching 5-6 times the initial radius the flow field looks like that produced by a point source and produces shock overpressures similar to those in the nuclear case. Numerical simulations of airblast phenomena have been carried out using one- and two-fluid Flux-Corrected Transport hydrocodes in one and two dimensions. The principal differences in the free-field solutions are the presence in the HE case of a contact discontinuity between air and HE products and of a backward-facing shock behind it. Temperatures in the nuclear fireball are initially three orders of magnitude higher; correspondingly, the density minimum at the center of the fireball is much broader and deeper. When the blast wave in a nuclear height-of-burst (HOB) situation undergoes regular reflection from the ground only one peak develops in the overpressure, and the reflected wave propagates upward rapidly through the hot underdense fireball. In the HE case

---

Manuscript approved June 29, 1983.

part of the upward-moving reflected wave is reflected downward at the contact surface, producing a second pressure peak on the ground, while the shock transmitted through the contact surface propagates slowly upward. After transition to Mach reflection other differences appear. At late times following shock breakaway the nuclear fireball, unlike the HE fireball, appears to develop a Rayleigh-Taylor instability along its lower edge below the HOB. The vortices (both forward and reverse) are stronger and form earlier. This has important consequences for fireball rise and for dust entrainment and transport to high altitudes.

## Section 1 INTRODUCTION

In this paper we describe a series of calculations carried out as part of the ongoing NRL effort aimed at studying airblast effects. The phenomena of chief interest to us include the following: peak overpressures and pressure histories on the ground as functions of yield, range, and height of burst (HOB), both at early times (prior to and during transition to Mach reflection) and at late times (after shock breakaway, with peak pressure in the range of tens of psi); velocity fields, particularly those associated with the toruses (both forward and reverse) in the neighborhood of the rising fireball; and the distribution of dust lifted off the ground by the winds and the structure of the cloud at the time of stabilization. We are interested in comparing the nuclear and HE cases, and learning how much they differ from one another. Our motivation is to determine the extent to which HE tests can simulate events in a nuclear height-of-burst situation.

The technique we have employed for this purpose is numerical modeling. One- and two-fluid hydrocodes based on the Flux-Corrected Transport (FCT) shock-capturing techniques<sup>1</sup> have been used to simulate airblast phenomena in one and two dimensions. FCT refers to a class of state-of-the-art fluid computational algorithms developed at NRL in the course of the past ten years with supersonic gas-dynamic applications expressly in mind. Simply put, our procedure is to model a one-kton nuclear burst and its 600-ton chemical equivalent, both at a HOB of 50 m, and compare the results. In order to validate, initialize, and interpret these 2D simulations, a number of ancillary calculations (mostly 1D) were undertaken. The results are most conveniently exhibited in terms of plots of peak overpressure vs range and time, station histories, contour plots of combustion product and total density, velocity vector plots, and tracer particle trajectories. Examples of these are presented to illustrate our results and conclusions.

The plan of the paper is as follows: In the next section we discuss our numerical techniques and validation procedures. In Section 3 we discuss the free-field (1D) solution and indicate the salient differences between nuclear and HE cases. Section 4 describes the 2D HOB calculations done for the HE and nuclear cases. In Section 5 we summarize our conclusions and discuss their domain of validity. We find that simulation of nuclear explosions by HE has distinct limitations, particularly at early times, in the fireball and transition regions, and in the details of the dust scouring process.

Section 2  
NUMERICAL TREATMENT

FCT is a finite-difference technique for solving the fluid equations in problems where sharp discontinuities arise (e.g., shocks, slip surfaces and contact surfaces).<sup>1</sup> It modifies the linear properties of a second- (or higher-) order algorithm by adding a diffusion term during convective transport, and then subtracting it out "almost everywhere" in the antidiffusion phase of each time step. The residual diffusion is just large enough to prevent dispersive ripples from arising at the discontinuity, thus ensuring that all conserved quantities remain positive. FCT captures shocks accurately over a wide range of parameters. No information about the number or nature of the surfaces of discontinuity need be provided prior to initiating the calculation.

The FCT routine used in the present calculations, called JPBFACT (an advanced version of ETBFCT)<sup>2</sup>, consists of a flexible, general transport module which solves 1-D fluid equations in Cartesian, cylindrical, or spherical geometry. It provides a finite-difference approximation to conservation laws in the general form:

$$\frac{\partial}{\partial t} \int_{\delta V(t)} \phi dV = - \int_{\delta A(t)} \phi (\underline{u} - \underline{u}_g) \cdot d\underline{A} + \int_{\delta A(t)} \tau dA, \quad (1)$$

where  $\phi$  represents the mass, momentum, energy or mass species in cell  $\delta V(t)$ ,  $\underline{u}$  and  $\underline{u}_g$  represent the fluid and grid velocities, respectively, and  $\tau$  represents the pressure/work terms. This formulation allows the grid to slide with respect to the fluid without introducing any additional

numerical diffusion. Thus, knowing where the features of greatest interest are located, one can concentrate fine zones where they will resolve these features most effectively as the system evolves.

The same transport routine is employed in the 2D r-z code (called FAST2D) via coordinate splitting. A Jones-Wilkins-Lee (JWL) equation of state (EOS) was used for the detonation products and a real-air EOS was used outside the HE-air interface.<sup>3</sup> The routine was written in the form of a table lookup, using interpolation with logarithms to the base 16 computed by means of logical shifts.<sup>4</sup> By thus taking account of the architecture of the machine (in these calculations, a 32-bit-word two-pipe Texas Instruments ASC) it was possible to generate very efficient vector code, decreasing the time required for EOS calculations to a small fraction of that required for the hydro. The EOS specifies pressure as a function of density and internal energy. In mixed cells the combined pressure was calculated according to Dalton's law.

For the HE calculations the initial conditions were taken to be the self-similar flow field corresponding to a spherical Chapman-Jouguet detonation at the time the detonation wave reaches the charge radius (Fig. 1)<sup>2</sup>. This was propagated with the 1D spherical code until the detonation front attained a radius just smaller than the HOB, at which time the solution was laid down on the 2D mesh (Fig. 2). The nuclear calculation was initialized with the 1-kton standard<sup>5</sup> with the same initial radius.

The boundary conditions were chosen to enforce perfect reflection on the ground and on the axis of symmetry

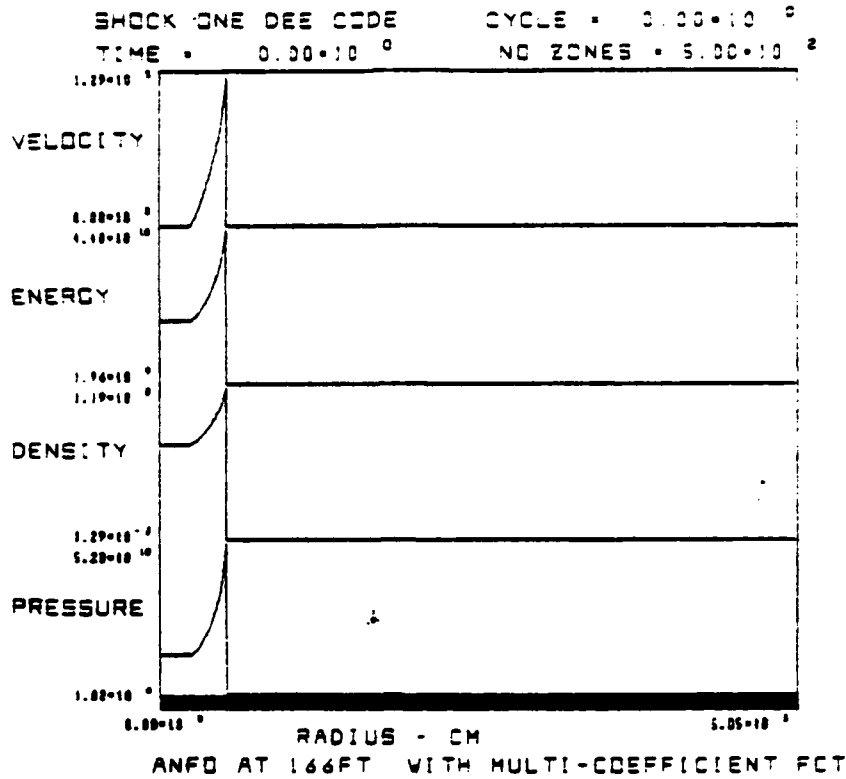


Figure 1

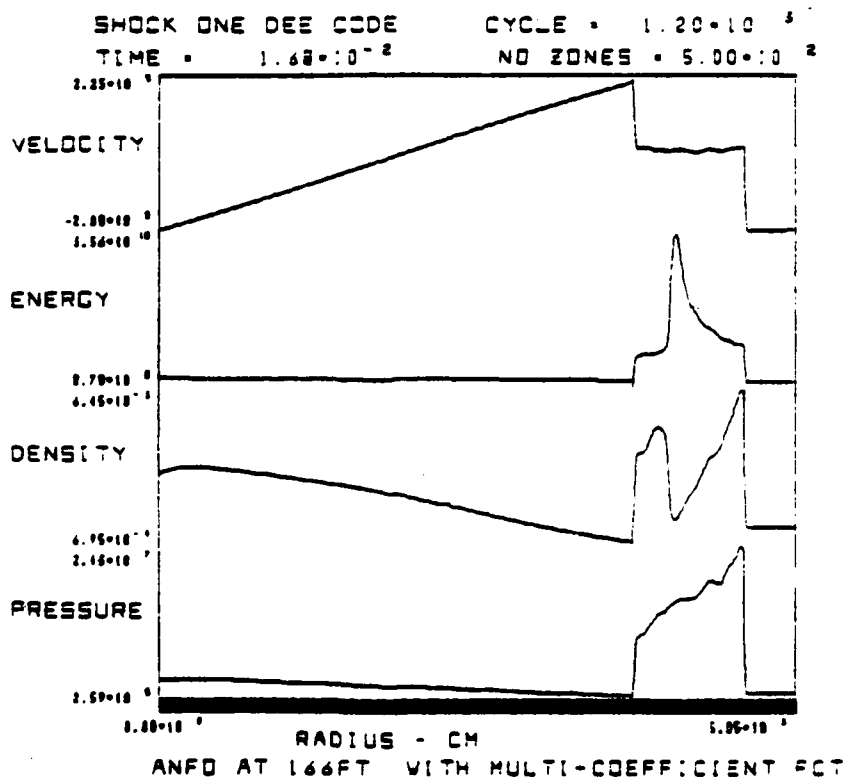


Figure 2

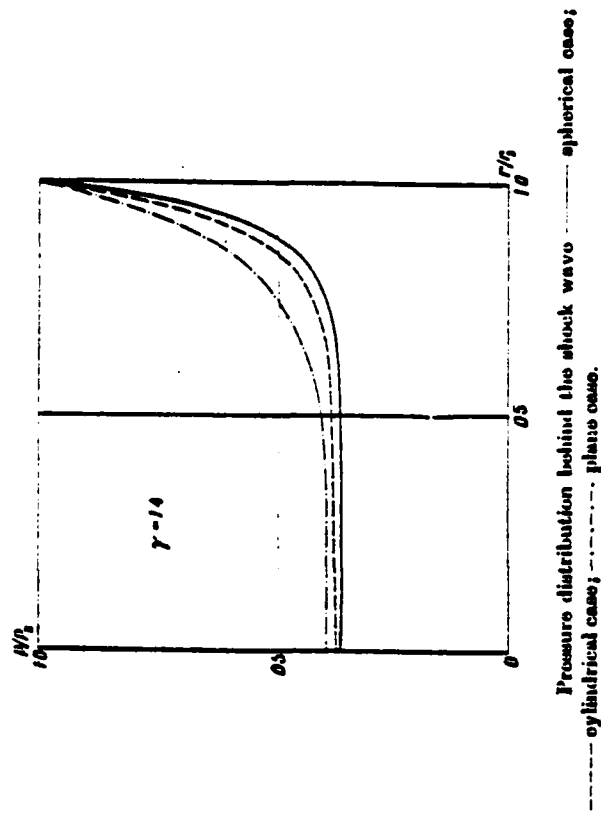
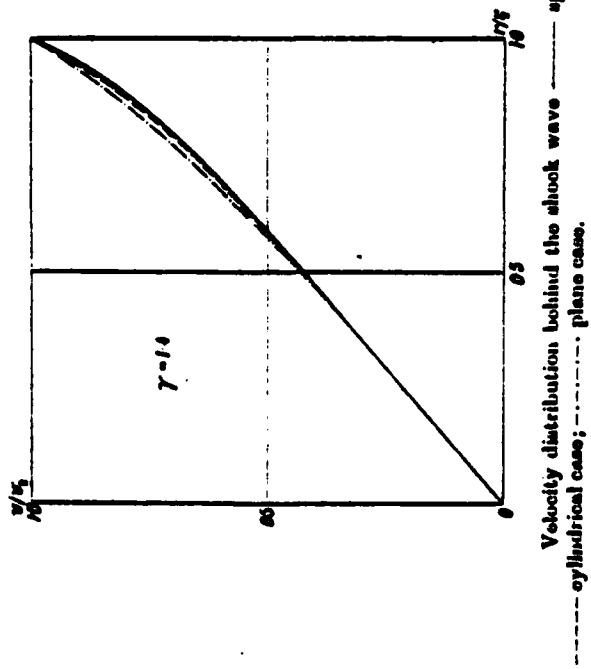
$[(d\phi/dn)_{bc} = 0, \text{ where } \phi = \rho, p, v^t, \text{ and } v_{bc}^n = 0], \text{ where "t" and "n" denote tangential and normal components, respectively, and outflow on the outer and the top boundaries } [(d\phi/dn)_{bc} = 0, \text{ where } \phi = \rho, p, v^t, v^n].$

For the 2D calculations the mesh was typically  $\sim 100 \times 100$ . Fixed gridding was used to minimize numerical errors. These zones were 2.1 m x 2.1 m. For the late time calculations, a fixed mesh with 100 zones in the radial and 200 zones in the vertical direction was used, with all cells of dimension 4.2 m x 4.2 m.

### Section 3 FREE-FIELD SOLUTION

The well-known Sedov similarity solution<sup>6</sup> for a point blast consists of a strong shock (post-shock pressure much larger than ambient pressure) followed by a rarefaction wave (Fig. 3). The density distribution is extremely concave and approaches zero at the origin. The pressure approaches a constant as  $r \rightarrow 0$ , so that the temperature diverges strongly. The profiles of the 1-kton standard solution (Fig. 4) are qualitatively similar, the temperature being essentially flat in the fireball region.

The solution used to initialize the HE problem, however, contains a number of features which are absent in the other solutions. These are most conspicuous in the density profile (Fig. 2), which exhibits a contact discontinuity between the HE products and shocked air, a secondary



00

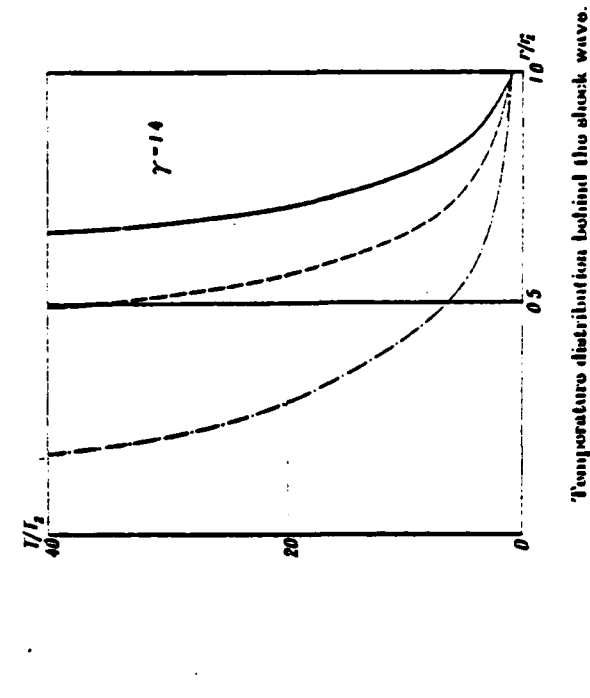
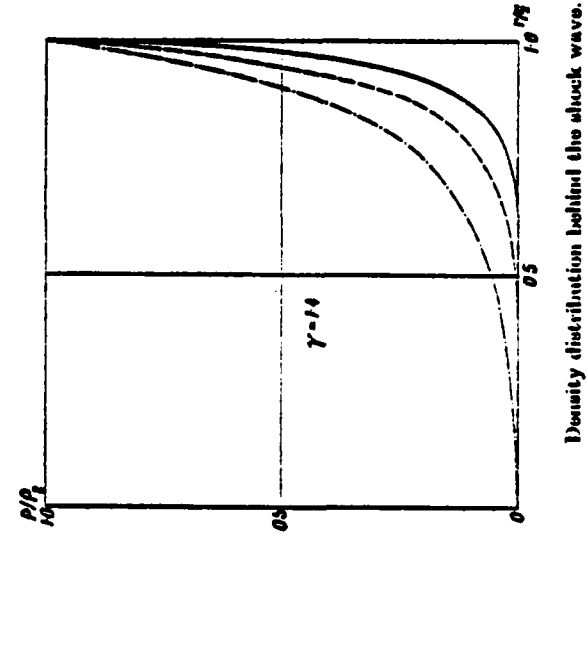


Figure 3

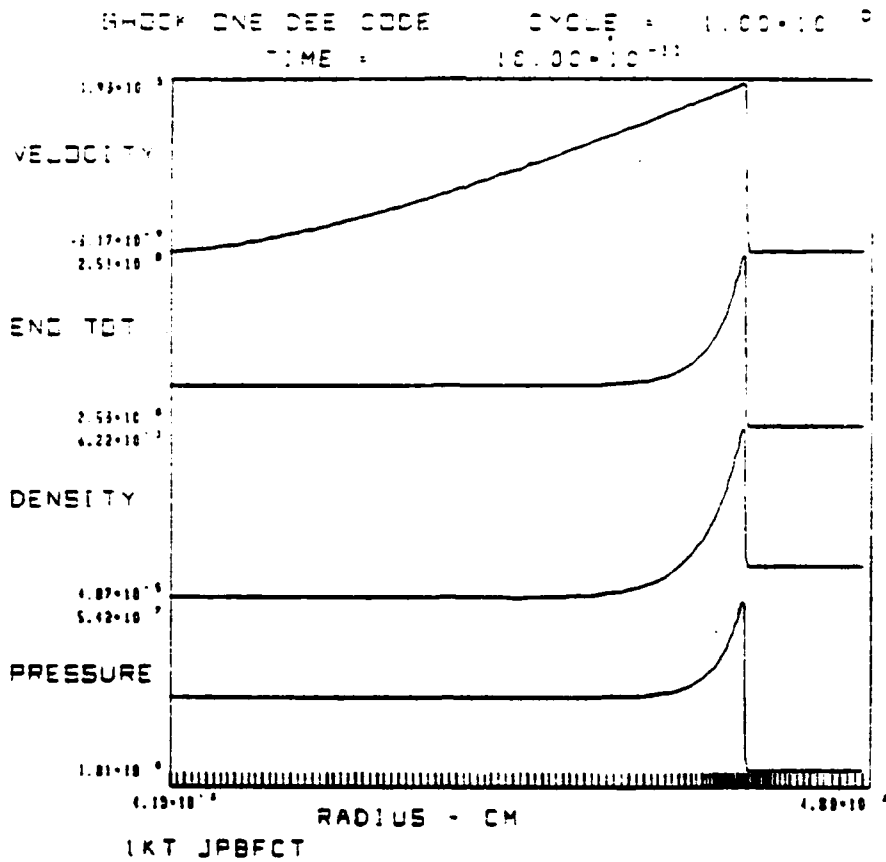


Figure 4

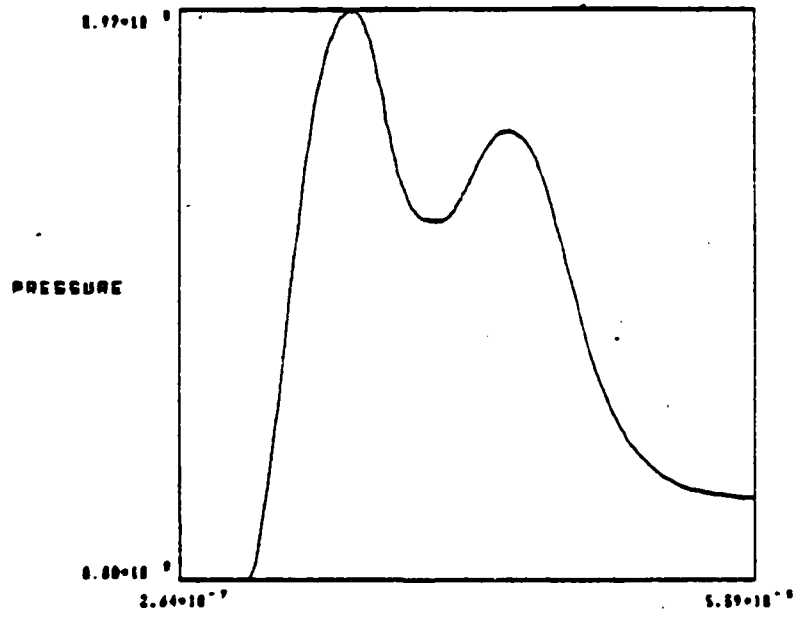


Figure 5

Reproduced from best available copy.

shock facing inward within the detonation products, and a gentle maximum near the origin. Because of this last feature, temperatures are about three orders of magnitude smaller in the fireball than in the nuclear case, and are nowhere divergent.

It follows that the speed of sound in the nuclear fireball is much greater than in the HE fireball. This has two immediate consequences, one physical and one numerical. The first is that shocks propagating through the nuclear fireball travel much faster. The second is that the upper limit on the computational timestep, set by the Courant criterion

$$\max \left( \frac{|v|+c}{\Delta x} \Delta t \right) < 1, \quad (2)$$

which usually is determined by conditions in the fireball, is much smaller relative to the shock time scale  $\tau_s = HOB/v_{\text{shock}}$  in the nuclear case than in the HE case.

As a result, even though the leading shock is well resolved (over  $\sim 2$  zones) in the free-field solution, the process of reflection even at ground zero (where the shock is incident normally) takes hundreds of timesteps. Coupled with the property of FCT (known as "clipping") which makes the points of all sharply-peaked profiles tend to flatten out until they are  $> 3$  zones across, this makes the rise time of the reflected shock quantities  $\sim 10$  times longer than that of the incident shock. This can be seen using a 1D spherical model calculation (Fig. 4), as well as in oblique reflection in 2D. This spreading is a problem only while the shock is in the immediate vicinity of the reflecting boundary. After

the reflected shock has propagated a few zones back into the interior of the mesh, the profiles steepen up and assume their correct forms (this has been shown by rerunning the calculation with a refined mesh and comparing the peak values after reflection with those predicted theoretically).

When the reflected shock begins propagating back to the origin it encounters drastically different conditions in the HE and nuclear cases. In the former, it strikes the contact discontinuity where it is partly transmitted and partly reflected. The reflected shock then proceeds outward until it reaches the ground (the end of the grid in the 1D calculation), producing the second peak in the station history shown in Fig. 5. In contrast, the shock wave reflected from the ground passes unhindered through the fireball at high speed until it reaches the upper boundary of the fireball whereupon it reflects back.

As we shall show, it is primarily through these reverberating shock waves and the wind pattern they set up that the HE and nuclear HOB airblasts differ.

#### Section 4 2D SIMULATION OF AIRBLAST

The yield and HOB (600 tons and 166 ft, respectively) were chosen to equal the values used in the Direct Course experiment, which we are simulating. The Chapman-Jouguet parameters used to initialize the spherical free-field calculation were taken to be those for the  $\text{NH}_4\text{NO}_3$ -fuel oil (ANFO) mixture used as the explosive.

Figures 6(a)-(c) show the contours of HE density and internal energy per unit mass and the velocity arrow plot at  $t=0$ , just before the reflection at ground zero occurs. Figures 6(d)-(f) show the corresponding plots 54 ms later, while Figs. 6(g)-(i) show them after 245 ms. Note the reflected shock proceeding upward, reflecting again off the fireball, and propagating back in a downward and outward direction. The interaction of this shock with the radially inward flow near the ground generates the reverse vortex, which is clearly seen in Fig. 6(i). Note also the positive vortex forming near the top of the grid in the same plot. The latter results when the upward-propagating reflected shock interacts with the radially outward flow near the top of the fireball; it is not produced by the buoyant rise of the fireball, which at these early times has scarcely begun.

To look at the evolution of the fireball at late times, we reinitialized on a larger, coarser grid, representing a cylinder 400 m in radius and 800 m high. The first 300 cycles approximately reproduce the early-time results. The spherical shock breaks away and leaves the mesh. The flows remaining on the grid are now subsonic everywhere. Then the fireball begins to rise and the subsequent development is due to the combination of buoyant rise and the action of the vortices set up by the early shocks.

Figures 7(a)-(b) show the reaction product density and velocities at 0.93 s. Note the "toe" reaching out along the ground and the bulge near the bottom of the HE product density produced by the constructive interference of forward and reverse vortices. These features are accentuated with the passage of time; in Figs. 7(c)-(d) ( $t = 2.70$  s), they are

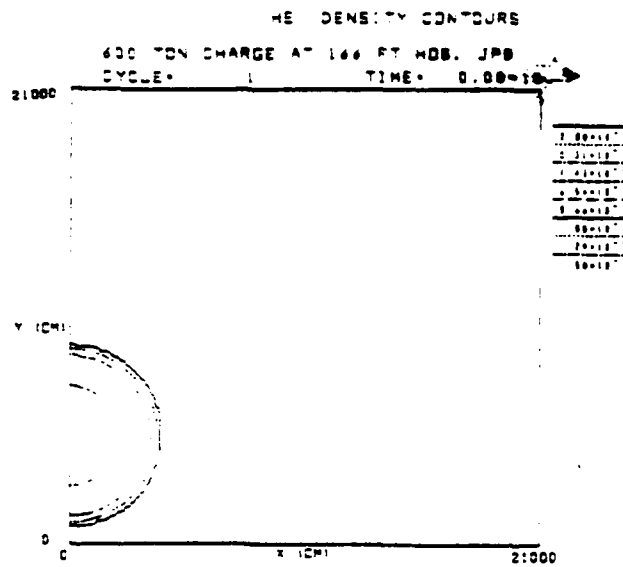


Figure 6a

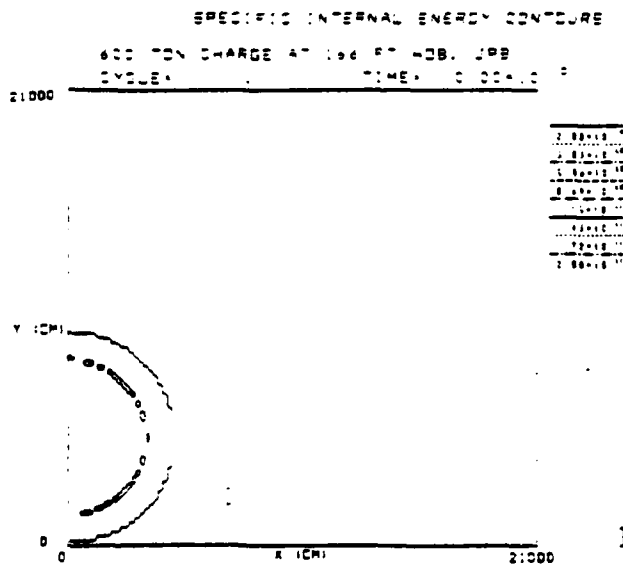


Figure 6b

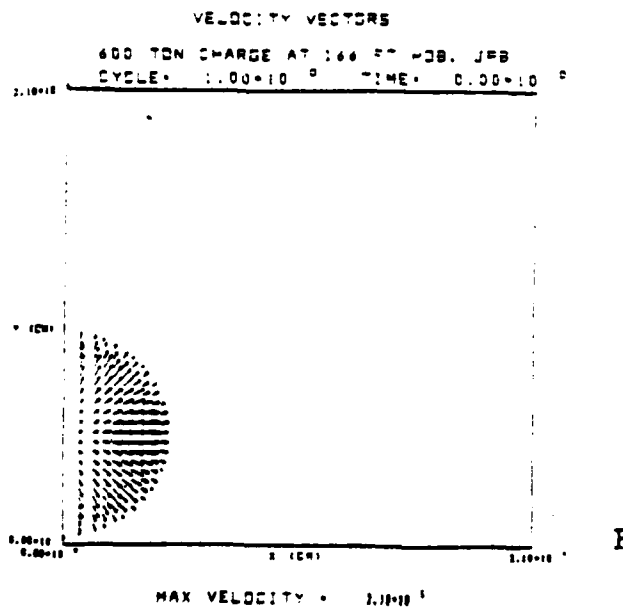
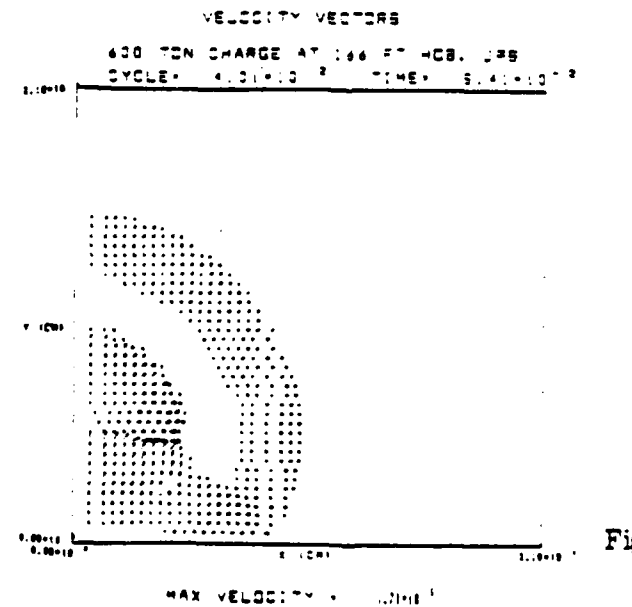
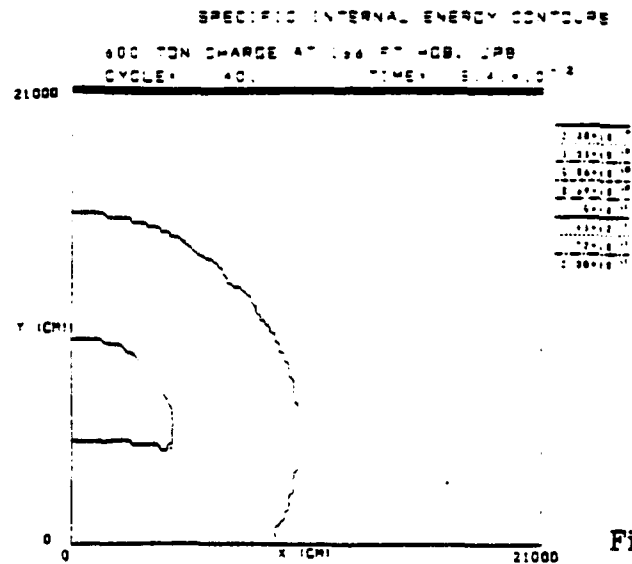
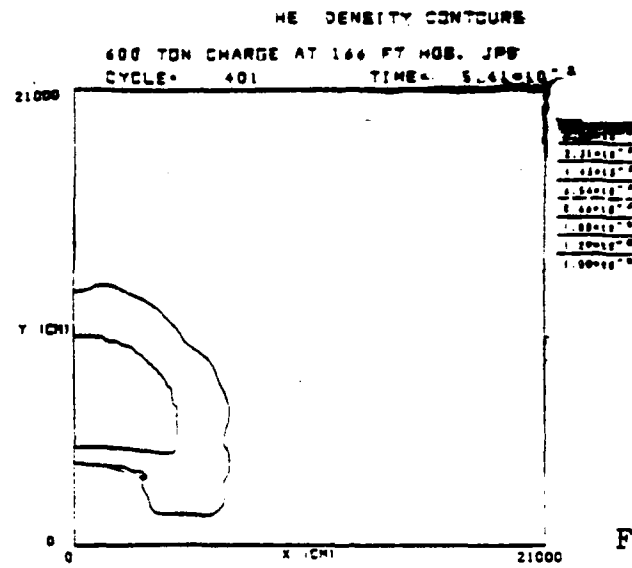
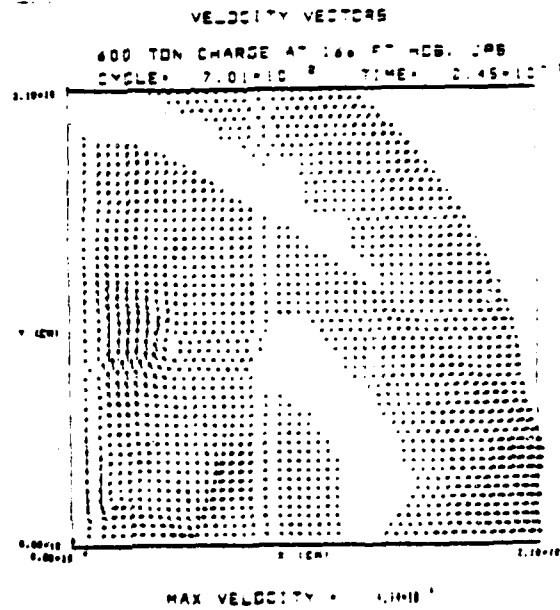
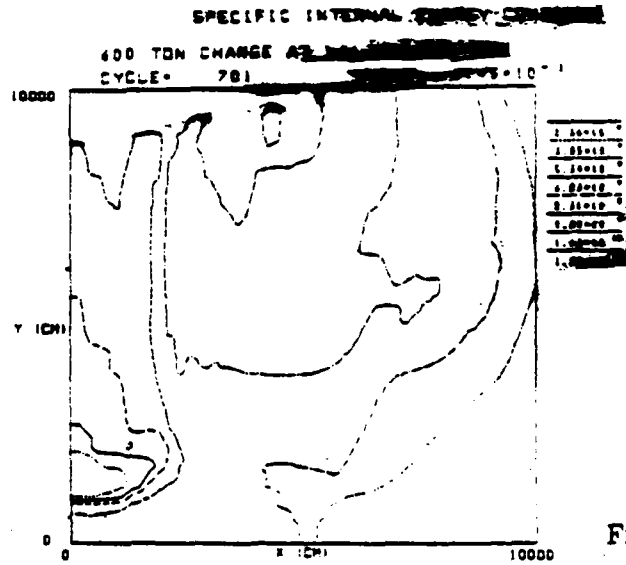
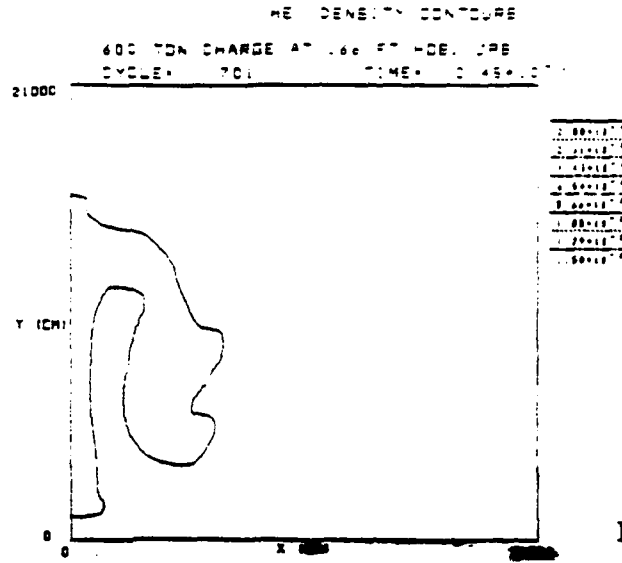


Figure 6c





AD-A138 836

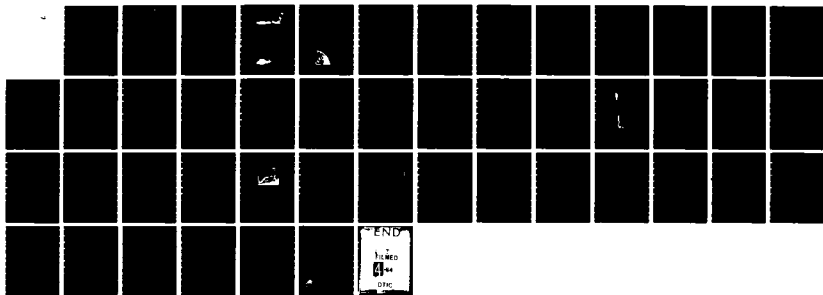
NUCLEAR AND NON-NUCLEAR AIRBLAST EFFECTS(U) SCIENCE  
APPLICATIONS INC MCLEAN VA M FRY 14 FEB 84 SAI-84/1529  
N00014-82-C-2229

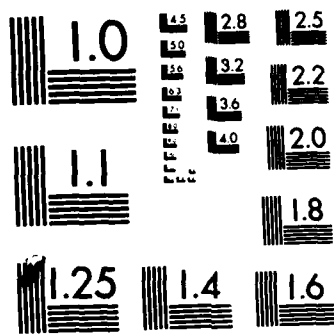
2/2

UNCLASSIFIED

F/G 19/4

NL





MICROCOPY RESOLUTION TEST CHART  
NATIONAL BUREAU OF STANDARDS-1963-A

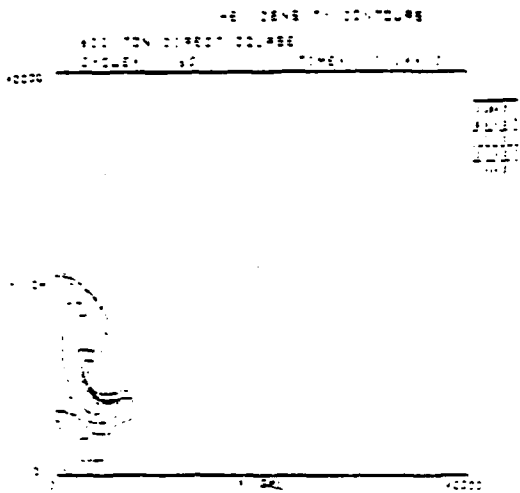


Figure 7a

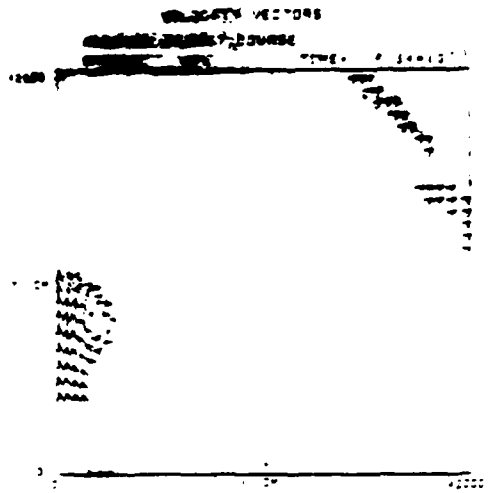


Figure 7b

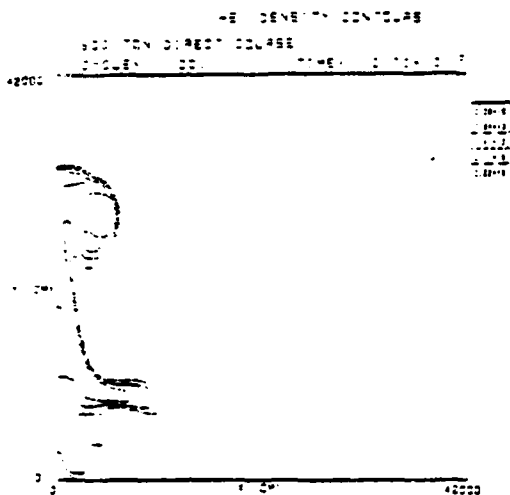


Figure 7c

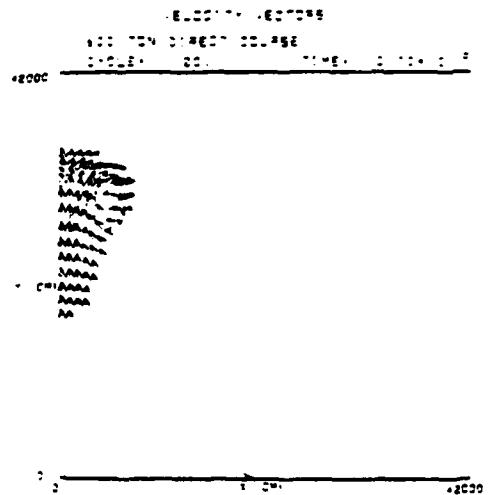


Figure 7d

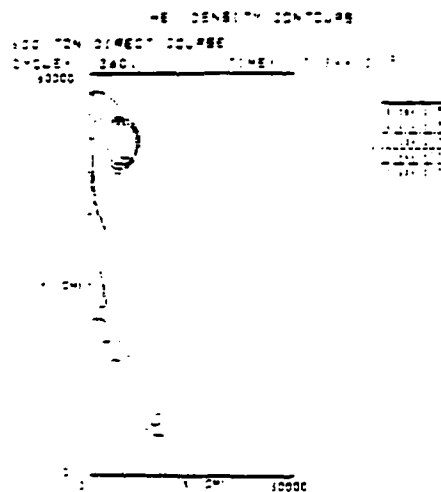


Figure 7e

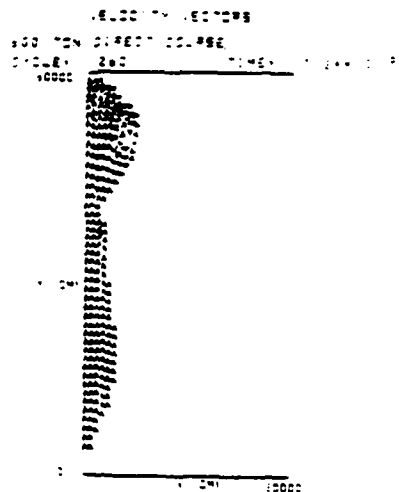


Figure 7f

even clearer. The cloud has become quite elongated vertically and shows a distinct mushroom shape. Development slows as the fireball cools and velocities diminish. By 7.34 s (after 2600 timesteps) the cloud is almost at 600 m. Figures 7(e)-(f) show its form at this time. Note that the maximum velocity is now 145 m/s.

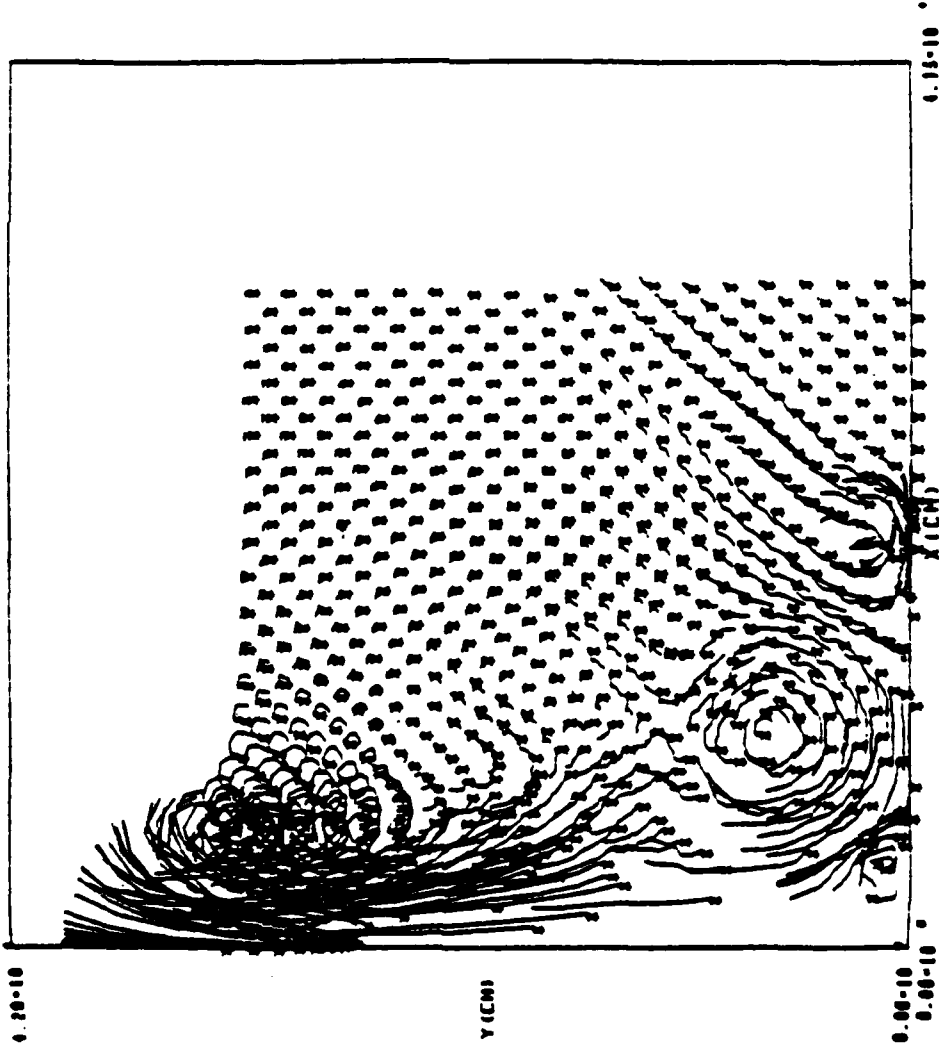
Figure 8a, which shows the trajectories of passively advected tracer particles over the time interval 1.8 sec to 3.97 sec, displays the vortices very clearly. Figure 8b shows the particle paths for the time interval 3.97 sec to 7.34 sec. Notice that there are four vortices visible in the plot: two positive and two reversed. The additional small vortices are apparently a consequence of entrainment by the major ones. As far as we know, their existence has not been noted previously.

When we repeat the calculation with nuclear initial conditions, several differences appear at a very early stage. The reflected shock propagates upward rapidly through the much hotter fireball and reverberates more. The maximum flow speeds (as opposed to sound speeds) are smaller, a difference which persists to late times. Although the shock radius as a function of time is essentially the same, the rarefaction wave moves faster as the deeper density well gets filled in.

Figures 9(a)-(c) show plots analogous to those of Figures 6(g)-(i); by this time it is clear that much of the early difference in the density profiles is washed out as pressure begins to relax to ambient. (The pressure differs from ambient by  $< 5\%$  everywhere, so that pressure contour plots are not very informative.) Note, however, the indentations that appear on the underside of the internal energy

PARTICLE PATH PLOT

600 TON DIRECT COURSE

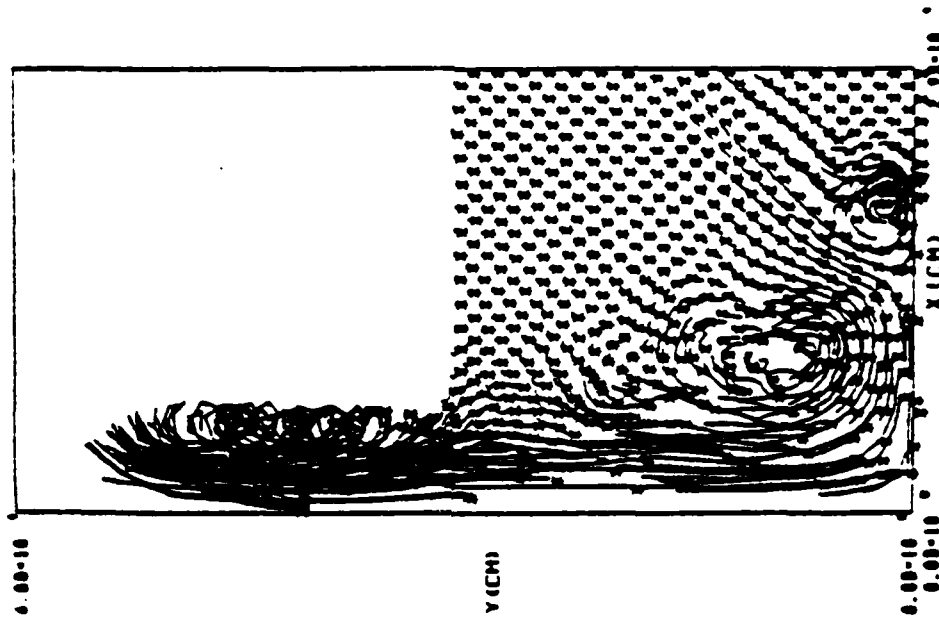


Time Interval  
1.0 sec → 1.97 sec

Figure 8a

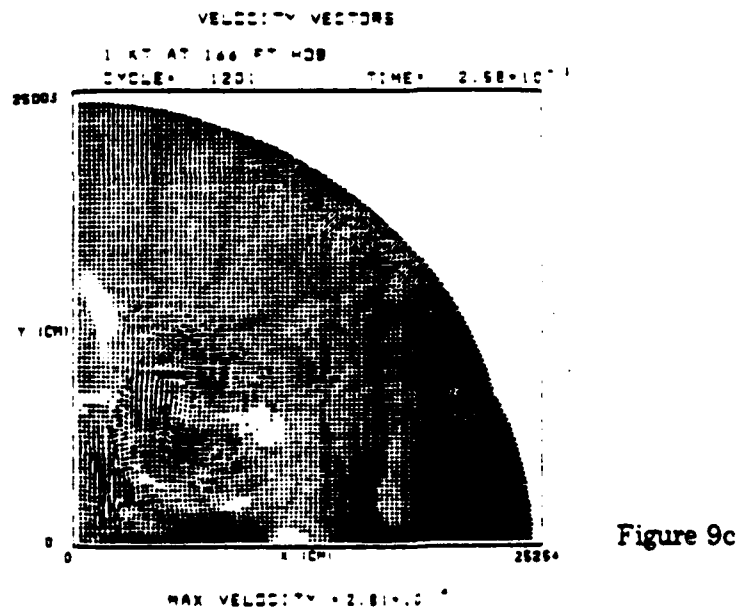
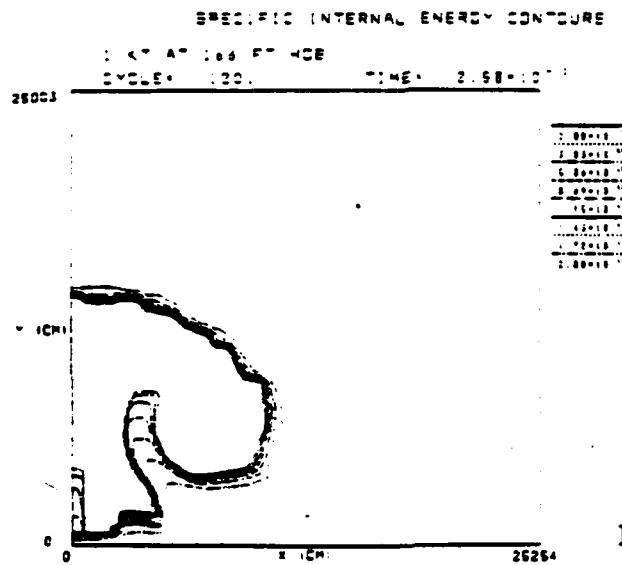
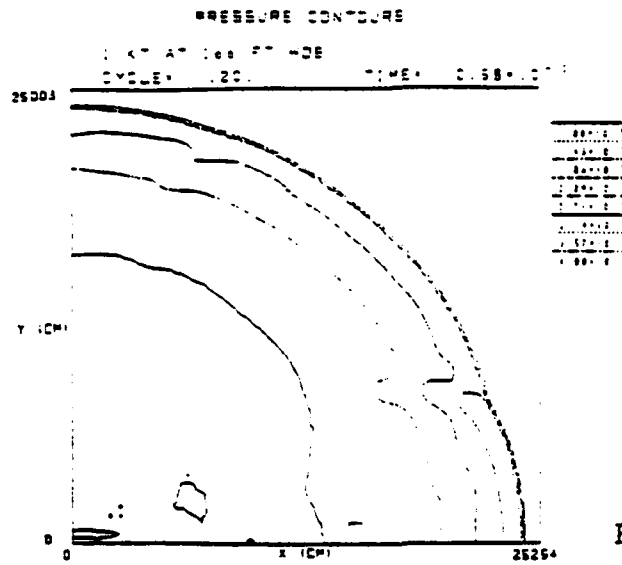
PARTICLE PATH PLOT

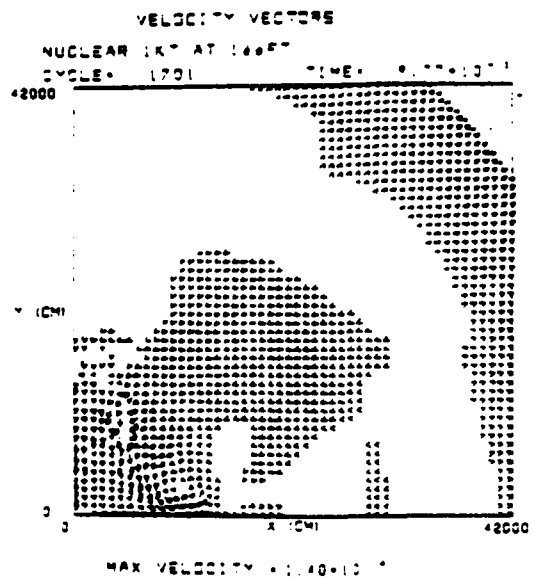
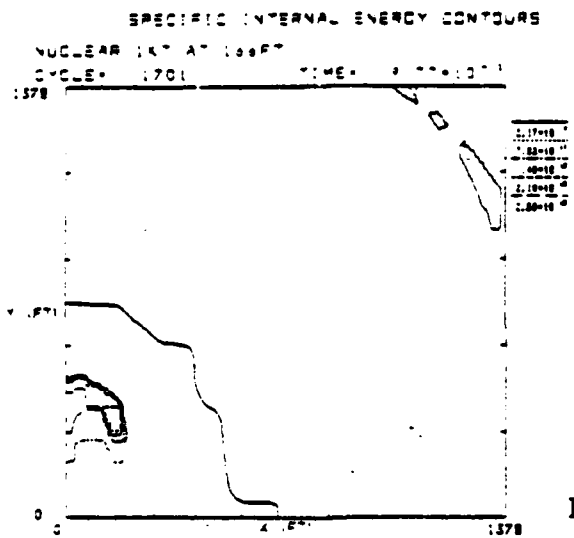
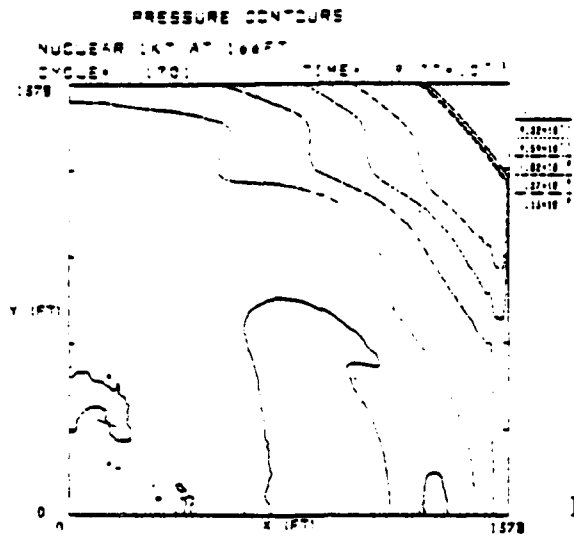
600 TON DIRECT COURSE



Time Interval  
1.97 sec → 7.1 sec

Figure 8b





contours at the base of the stem [Fig. 9(b)]. These are absent in the corresponding HE plot, Fig. 6(g). We conjecture that they are the signature of a fluid instability, possible Rayleigh-Taylor. The idea is that the air sucked in by the (forward) vortex at the bottom of the fireball is much denser than the fireball itself. In running into the latter it sets up the classic condition for Rayleigh-Taylor instability (direction of effective gravity and density gradient are opposed).

It is clear that the major qualitative differences between the HE and nuclear cases persist longest in the velocity plots. This is not surprising, as the circulation patterns represented by the vortices have essentially infinite lifetimes in the absence of viscosity. We have run both nuclear and HE cases out to stabilization (not shown here) and have shown that there are qualitative differences in velocity plots to the very end. At all times  $t > 0$  the peak flow velocity in the HE case exceeds that in the comparable nuclear result. This is a reflection of the fact that the Chapman-Jouguet solution at a radius of 10 m has a pressure peak of 52 kbar, vs 3 kbar for the 1-kton standard at the same radius. This means that the former starts out with much more violent motion, i.e., fluid velocities an order of magnitude larger. In point of fact, the HE case does not closely resemble a point source. At initialization the nuclear profiles have ~ 6% of the yield in kinetic energy. This fraction increases to a maximum of ~ 15%, then decreases. In the HE case the fraction is initially about one-half and decreases monotonically thereafter at about the same rate as in the nuclear case.

## Section 5 CONCLUSIONS

We have described numerical simulations carried out for a 600-ton HE burst and a 1-kton nuclear burst, both at 166 ft. The code, gridding, and method of solution are the same in the two calculations. Although the shock waves in the two cases propagate at roughly the same speed and break away at roughly the same time, and although the pressure fields relax to ambient in similar fashion, we find significant differences, of which the following appear to be the most important.

- (i) The HE flow velocities are systematically larger.
- (ii) In the regular reflection region (underneath and close to the fireball), the HE case exhibits two overpressure peaks at the surface, rather than one, due to re-reflection of the reflected shock from the contact surface between air and detonation products.
- (iii) For the HE case the upper vortex forms first, followed by the reverse vortex near the axis of symmetry and the ground. Adjacent HE products begin to be entrained into a positive vortex over a longer period of time, several seconds. In the nuclear case the negative vortex is the dominant one; it is larger than the HE, persists longer, and

contains larger velocities than the positive vortex at comparable times.

- (iv) The HE flow establishes a pattern of four vortices, two forward and two reversed, instead of one of each.
- (v) The stem of the nuclear fireball appears to exhibit a Rayleigh-Taylor instability, absent in the HE case.

Since the velocities on axis are higher in the HE case (the upper positive vortex is larger), fireball rise is faster than in the nuclear case. The nuclear case, however, probably scours up more dust because the velocities are larger, and the reverse vortex is larger and more persistent. It is difficult to argue conclusively on this point because so much depends on terrain, conditions in the boundary layer, and other physical effects not included in this model (e.g., precursor heating and turbulence). Further study of the tracer particle motions we have calculated is expected to be illuminating in this regard.

#### REFERENCES

1. Boris, J. P. and Book, D. L. in Methods in Computational Physics, J. Killeen Ed., (Academic Press, NY, 1976), Vol. 16, p. 85.
2. Boris, J. P., "Flux-Corrected Transport Modules for Solving Generalized Continuity Equations", NRL Memo Report 3237 (1976). AD-A023-891.

3. Kuhl, A. L., Fry, M. A., Picone, M., Book, D. L., Boris, J. P., "FCT Simulation of HOB AIRBLAST Phenomena", NRL Memo Report No. 4613 (1981). AD-A107-920.
4. Young, T. R., "Table Look-Up: An Effective Tool on Vector Computers", Tenth Conf. on Numerical Simulation of Plasmas, San Diego, CA, January 4-6, 1983.
5. Needham, C. E. and Crepeau, J. E., "The DNA Nuclear Blast Standard (1-KT)", DNA Report 5648T, January 1981.
6. Sedov, L. I., Similarity and Dimensional Methods in Mechanics, Academic Press, NY, 1959.

#### ACKNOWLEDGMENT

This work was supported by the Defense Nuclear Agency under Subtask N99QAXAH Work Unit # 00061, Work Unit Title "Cloud Calculations".

APPENDIX D  
ADAPTATION OF FLUX-CORRECTED TRANSPORT ALGORITHMS  
FOR MODELING DUSTY FLOWS

REPORT DOCUMENTATION PAGE		READ INSTRUCTIONS BEFORE COMPLETING FORM
1. REPORT NUMBER NRL Memorandum Report 5230	2. GOVT ACCESSION NO.	3. RECIPIENT'S CATALOG NUMBER
4. TITLE (and Subtitle) ADAPTATION OF FLUX-CORRECTED TRANSPORT ALGORITHMS FOR MODELING DUSTY FLOWS	5. TYPE OF REPORT & PERIOD COVERED Interim report on a continuing NRL problem.	
7. AUTHOR(s) M.A. Fry* and D.L. Book	6. PERFORMING ORG. REPORT NUMBER	
3. PERFORMING ORGANIZATION NAME AND ADDRESS Naval Research Laboratory Washington, DC 20375	8. CONTRACT OR GRANT NUMBER(s) N00014-82-C-2229	
11. CONTROLLING OFFICE NAME AND ADDRESS Defense Nuclear Agency Washington, DC 20305	10. PROGRAM ELEMENT PROJECT, TASK AREA & WORK UNIT NUMBERS 62715H; 44-07 2-0-3	
14. MONITORING AGENCY NAME & ADDRESS (if different from Controlling Office)	12. REPORT DATE December 2 1983	13. NUMBER OF PAGES 23
	15. SECURITY CLASSIFICATION (of this report) UNCLASSIFIED	
	15a. DECLASSIFICATION/DOWNGRADING SCHEDULE	
16. DISTRIBUTION STATEMENT (of this Report)  Approved for public release; distribution unlimited.		
17. DISTRIBUTION STATEMENT (of the abstract entered in Block 20, if different from Report)		
18. SUPPLEMENTARY NOTES *Present address: Science Applications, Inc., McLean, VA 22102 This work was supported by the Defense Nuclear Agency under Subtask N99QAXAH, work unit 00061, work unit title "Cloud Calculations," and under Subtask Y99QAXSG, work unit 00057, work unit title "Airblast Calculations."		
19. KEY WORDS (Continue on reverse side if necessary and identify by block number) Flux-corrected transport                      Airblast Finite-difference algorithms                 Height-of-burst		
20. ABSTRACT (Continue on reverse side if necessary and identify by block number) Blast wave phenomena include reactive and two phase flows resulting from the motion of chemical explosion products. When the blast wave interacts with structural surfaces (external discontinuities), multiple reflections and refractions occur from both external and internal discontinuities. The most recent version of the Flux-Corrected Transport (FCT) convective- equation solver has been used both in one and two dimensions to simulate chemical explosive blast waves reflecting from planar structures for yields ranging from 8 lbs to 600 tons.  (Continues)		

20. ABSTRACT (Continued)

One can relate the strength of the second reflected peak to the sharpness of the contact discontinuity, and thus measure the capability to predict all the salient features of the blast wave. The flow patterns obtained reveal four different vortices, two forward and two reversed. Their effect on the motion of tracer particles has been studied in order to determine the motion of (1) HE detonation products and (2) dust scoured up from the ground.

CONTENTS

INTRODUCTION ..... 1

NUMERICAL TREATMENT ..... 2

600-TON ANFO EXPLOSION AT 166 FT ..... 5

CONCLUSIONS ..... 6

REFERENCES ..... 11

ACKNOWLEDGMENT ..... 11

# ADAPTATION OF FLUX-CORRECTED TRANSPORT ALGORITHMS FOR MODELING DUSTY FLOWS

M. A. Fry, Science Applications, Inc.

and

D. L. Book, Naval Research Laboratory

## INTRODUCTION

In this paper we describe a series of calculations carried out as part of an ongoing effort aimed at studying blast wave diffraction effects in air. The phenomena of chief interest to us include velocity fields, particularly those associated with the toruses (both forward and reverse) in the neighborhood of the rising fireball, and the distribution of dust lifted off the ground by the winds and the structure of the cloud at the time of stabilization. We are interested in studying the nature of the gas-dynamic discontinuities which appear, the vortices (both forward and reverse), and how the dust content of the air affects the evolution of the blast wave.

The technique we have employed for this purpose is numerical modeling. One- and two-fluid hydrocodes based on the Flux-Corrected Transport (FCT)<sup>1</sup> shock-capturing techniques have been used to simulate airblast phenomena in one and two dimensions. FCT refers to a class of state-of-the-art fluid computational algorithms developed at NRL in the course of the past ten years with supersonic gas-dynamic applications expressly in mind. We have concentrated on modeling the "Direct Course" event, an experiment to be fielded shortly by the Defense Agency: a 600-ton ammonium nitrate + fuel oil (ANFO) charge is detonated at a height of burst (HOB) of 166 ft. The results are most conveniently exhibited in terms of velocity vector plots and tracer particle trajectories. Examples of these are presented to illustrate our results and conclusions.

The plan of the paper is as follows: In the next section we discuss our numerical techniques and validation procedures. In Section 3 we describe the 600-ton 2D HOB calculations. In Section 4 we summarize our conclusions and discuss their domain of validity.

## NUMERICAL TREATMENT

As described by Boris and Book<sup>1</sup>, FCT is a finite-difference technique for solving the fluid equations in problems where sharp discontinuities arise (e.g., shocks, slip surfaces and contact surfaces). It modifies the linear properties of a second- (or higher-) order algorithm by adding a diffusion term during convective transport, and then subtracting it out "almost everywhere" in the antidiffusion phase of each time step. The residual diffusion is just large enough to prevent dispersive ripples from arising at the discontinuity, thus ensuring that all physically positive conserved quantities remain positive. FCT captures shocks accurately over a wide range of parameters. No information about the number or nature of the surfaces of discontinuity need be provided prior to initiating the calculation.

The FCT routine used in the present calculations, called JPBFACT (an advanced version of EIBFACT<sup>2</sup>), consists of a flexible, general transport module which solves 1-D fluid equations in Cartesian, cylindrical, or spherical geometry. It provides a finite-difference approximation to conservation laws in the general form:

$$\frac{\partial}{\partial t} \int_{\delta V(t)} \phi dV = - \int_{\delta A(t)} \phi (\underline{u} - \underline{u}_g) \cdot d\underline{A} + \int_{\delta A(t)} \tau dA, \quad (1)$$

where  $\phi$  represents the mass, momentum, energy or species mass density in cell  $\delta V(t)$ ,  $\underline{u}$  and  $\underline{u}_g$  represent the fluid and grid velocities, respectively, and  $\tau$  represents the pressure/work terms. This formulation allows the grid to slide with respect to the fluid without introducing any additional numerical diffusion. Thus, knowing where the features of greatest interest are located, one can concentrate fine zones where they will resolve these features most effectively as the system evolves.

The same transport routine was employed for both coordinate directions in the 2D r-z code (called FAST2D) via timestep splitting. A Jones-Wilkins-Lee (JWL) equation of state (EOS) was used for the detonation products and a real-air EOS was used outside the HE-air interface<sup>3</sup>. The routine was written in the form of a table lookup, using interpolation with logarithms to the base 16 computed by means

of logical shifts". By thus taking account of the architecture of the machine (in these calculations, a 32-bit-word two-pipe Texas Instruments ASC) it was possible to generate very efficient vector code, decreasing the time required for EOS calculations to a small fraction of that required for the hydro. The EOS specifies pressure as a function of density and internal energy. In mixed cells the combined pressure was calculated according to Dalton's law.

The initial conditions were taken to be the self-similar flow field used by Kuhl, et al.<sup>3</sup>, corresponding to a spherical Chapman-Jouquet detonation at the time the detonation wave reaches the charge radius (Fig. 1). This was propagated with the 1D spherical code until the detonation front attained a radius just smaller than the HOB, at which time the solution was laid down on the 2D mesh (Fig. 2).

The boundary conditions were chosen to enforce perfect reflection on the ground and on the axis of symmetry  $[(d\phi/dn)_{bc} = 0, \text{ where } \phi = \rho, p, v^t, \text{ and } v_{bc}^n = 0]$ , where "t" and "n" denote tangential and normal components, respectively, and outflow on the outer and the top boundaries  $[(d\phi/dn)_{bc} = 0, \text{ where } \phi = \rho, p, v^t, v_{bc}^n]$ .

For the 2D calculations the mesh was typically 200 x 100. Fixed gridding was used to minimize numerical errors. The zone sizes were 2.1 m x 2.1 m, respectively. For the late-time calculations, a fixed mesh with 100 zones in the radial and 200 zones in the vertical direction was used, with all cells of dimension 4.2 m x 4.2 m.

To study the motion of dust particles in the flow field generated by the calculation, the simplest model describes dusty air as a single phase with density and adiabatic index chosen appropriately. This approach ignores the properties associated with the particulate structure of the dust and the process of scouring by which the dust enters the air. A more realistic picture results if we treat the dust as a distinct phase, described by equations of mass, momentum and energy conservation, as has been done in one dimension by Miura and Glass<sup>5</sup>. The dust equations are coupled to those describing the air through drag and heat transfer terms.

It has been pointed out by Kuhl<sup>6</sup> that in such a treatment a dust particle tends to become entrained in the prevailing flow over a distance  $\sim 10^5$  particle diameters. Thus a one-phase description is satisfactory whenever particle sizes are at least a thousand times smaller than the smallest length scale in the hydrodynamics. For the present calculation, this scale is roughly 1 m, so particles smaller than 1 mm can be regarded as totally entrained.

When the mass density of the dust component is small compared with air (or HE product) density, a further simplification is possible. Entrained dust particles can be followed by passive advection. That is, the wind fields  $u_x$ ,  $u_y$  are taken from a dust-free hydrodynamics calculation, and dust is advected in these fields according to

$$\frac{dx}{dt} = u_x, \quad \frac{dy}{dt} = u_y. \quad (2)$$

In this approximation we ignore the effect of the momentum and energy transfer on the air phase. The same approximation can be used for larger (nonentrained) particles also, provided we include inertia and drag by using the force law

$$m \frac{d\vec{v}}{dt} = -mge_z + D(\vec{v} - \vec{V}), \quad (3)$$

where  $\vec{v}$  is the particle velocity,  $g$  is the acceleration due to gravity, and  $D$  is the empirical drag coefficient employed by Miura and Glass<sup>5</sup>.

Equations (2) and (3) apply best in the limits of extremely small and extremely large particles, respectively. Although they restrict the scope of the calculation (by requiring the dust content to be small), they have the computational advantage of allowing us to obtain time-dependent dust distributions for many different choices of dust size spectrum and initial distribution from a single hydrodynamics calculation.

## 600-TON ANFO EXPLOSION AT 166 FT

The yield and HOB (600 tons and 166 ft, respectively) in the calculation were chosen to equal the values used in the Defense Nuclear Agency Direct Course experiment, which we are simulating. The Chapman-Jouguet parameters used to initialize the spherical free-field calculation were taken to be those for the  $\text{NH}_4\text{NO}_3$ -fuel oil (ANFO) mixture used as the explosive.

Figs. 3(a)-(c) show the contours of HE density and internal energy per unit mass and the velocity arrow plot at  $t=0$ , just before the reflection at ground zero occurs. Figs. 3(d)-(f) show the corresponding plots 54 ms later, while Figs. 3(g)-(i) show them after 245 ms. Note the reflected shock proceeding upward, reflecting again off the fireball, and propagating back in a downward and outward direction. The interaction of this shock with the radially inward flow near the ground generates the reverse vortex, which is clearly seen in Fig. 3(i). Note also the positive vortex forming near the top of the grid in the same plot. The latter results when the upward-propagating reflected shock interacts with the radially outward flow near the top of the fireball; it is not produced by the buoyant rise of the fireball, which at these early times has scarcely begun.

To look at the evolution of the fireball at late times, we reinitialized on a larger, coarser grid, representing a cylinder 400 m in radius and 800 m high. The first 300 cycles approximately reproduce the early-time results. The spherical shock breaks away and leaves the mesh. The flows remaining on the grid are now subsonic everywhere. Then the fireball begins to rise and the subsequent development is due to the combination of buoyant rise and the action of the vortices set up by the early shocks.

Figure 4a, which shows the trajectories of passively advected tracer particles over the time interval 1.8 sec to 3.97 sec, displays the vortices very clearly. Fig. 4b shows the particle paths for the time interval 3.97 sec to 7.34 sec. Notice that there are four vortices visible in the plot: two positive and two reversed. The additional small vortices are apparently a consequence of entrainment by the major ones. As far as we know, their existence has not been noted previously.

It is clear that the major qualitative features persist longest in the velocity plots. This is not surprising, as the circulation patterns represented by the vortices have essentially infinite lifetimes in the absence of viscosity. We have run out to stabilization (not shown here) and have found that these features persist in the velocity plots to the very end. At all times  $t > 0$  the peak flow velocity in the HE case exceeds that in the comparable point source solution. This is a reflection of the fact that the Chapman-Jouguet solution at a radius of 10 m has a pressure peak of 52 kbar, vs 3 kbar for the Sedov solution at the same radius. This means that the former starts out with much more violent motion, i.e., fluid velocities an order of magnitude larger. All in all, in many respects the HE case does not closely resemble a point source.

### CONCLUSIONS

We have described a numerical simulation of the Direct Course Event. The code, gridding, and method of solution are the same in the two calculations. The following conclusions appear to be among the most important.

- (i) The flow establishes a pattern of four vortices, two forward and two reversed, instead of one of each.
- (ii) The upper vortex forms first, followed by the reverse vortex near the axis of symmetry and the ground. Adjacent HE products begin to be entrained into a positive vortex over a longer period of time, several seconds.
- (iii) Once picked up (scoured) off the ground, dust is efficiently transported upward by the reverse vortex farther from the axis.

Phenomena neglected in the present model (e.g., terrain, conditions in the boundary layer, turbulence, humidity, etc.) are unlikely to alter the above conclusions, which mainly depend on the characteristics of the solutions in the interior of the mesh and over long periods of time. Further study of the tracer particle motions we have calculated is likely to be illuminating, particularly when we begin to consider the evolution of various initial configurations as a function of particle size. In closing, it is appropriate to emphasize the far-reaching significance of the role played by the HE-air interface in the dynamics of both airblast and cloud rise phenomena, and the importance for numerical simulation of correctly treating this interface.

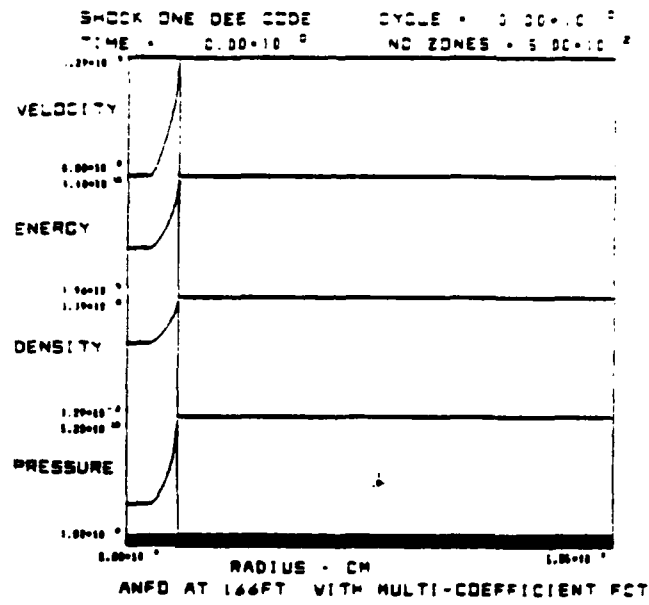


Figure 1

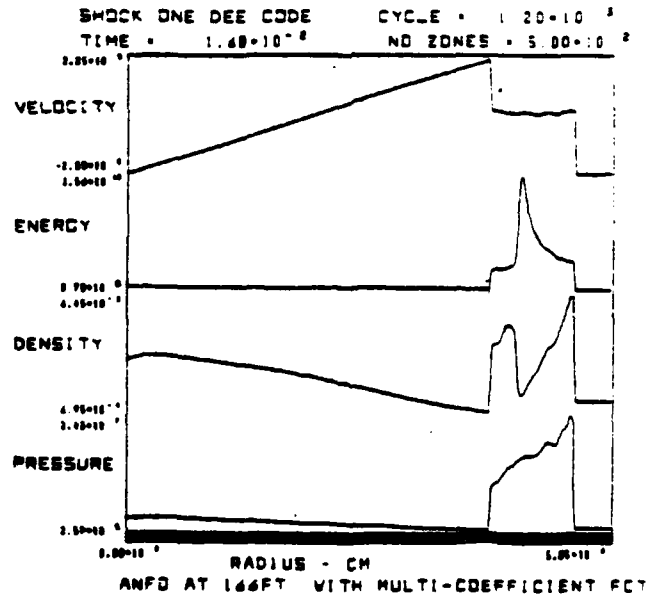


Figure 2

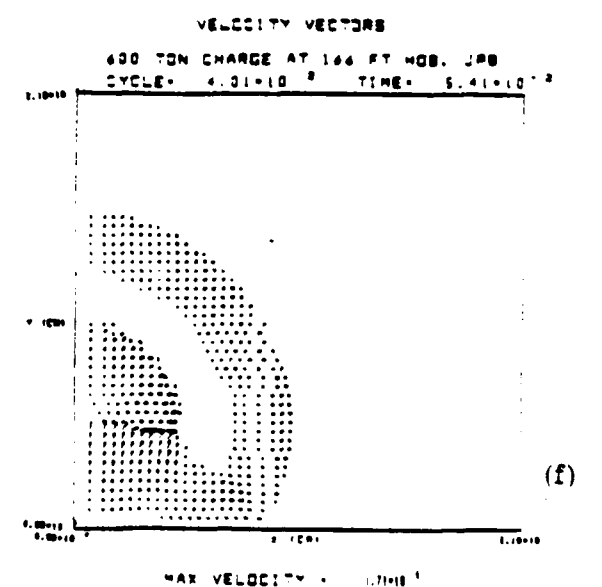
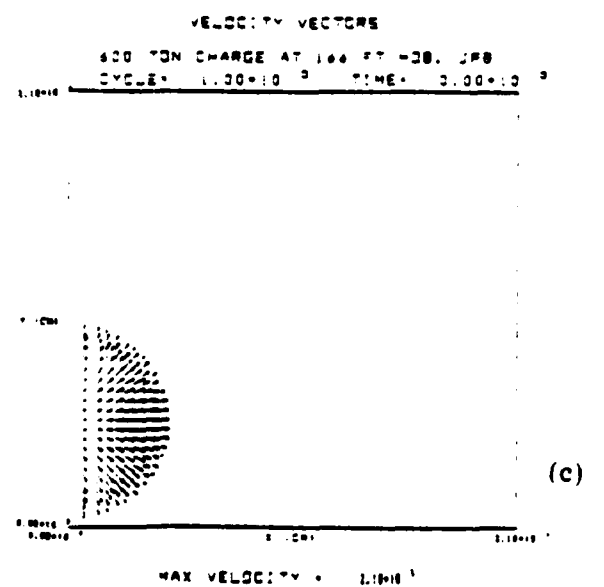
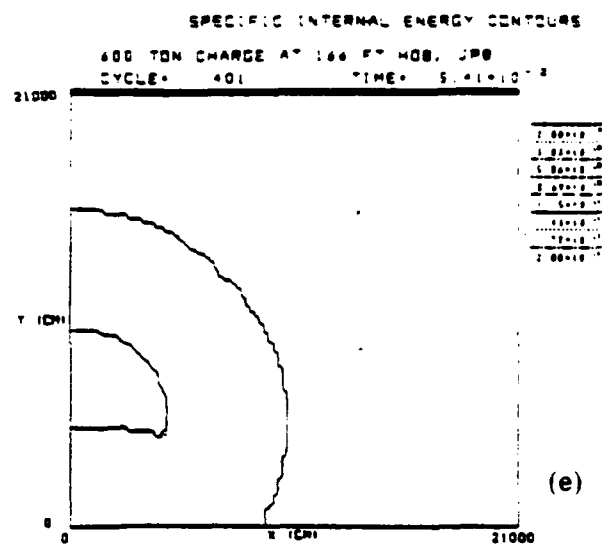
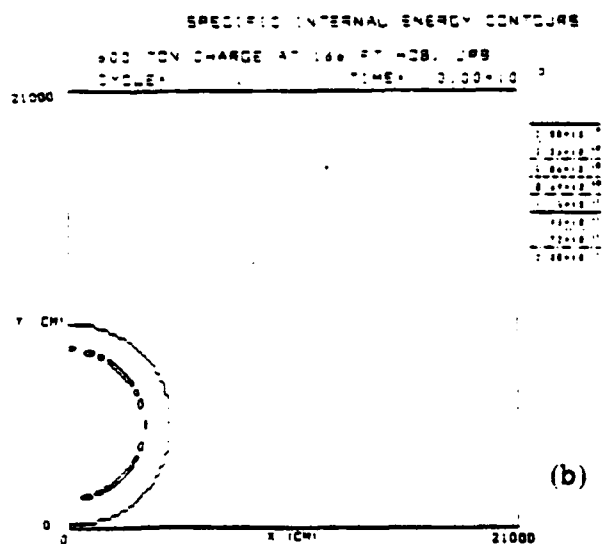
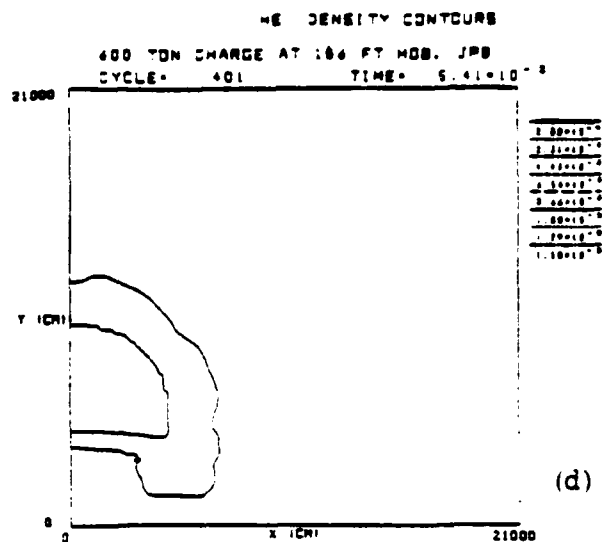
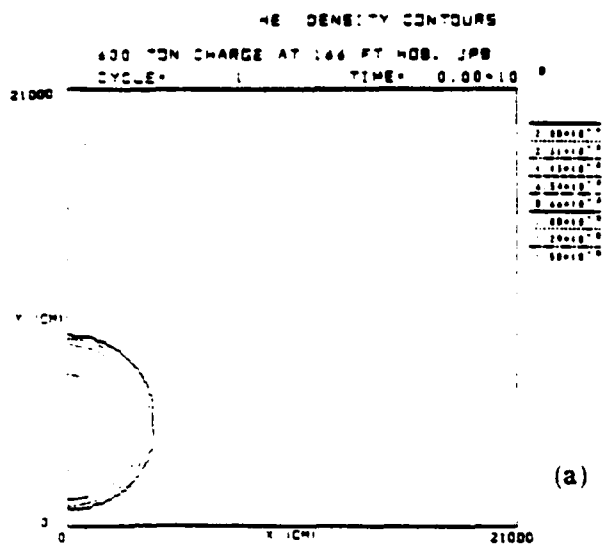


Figure 3

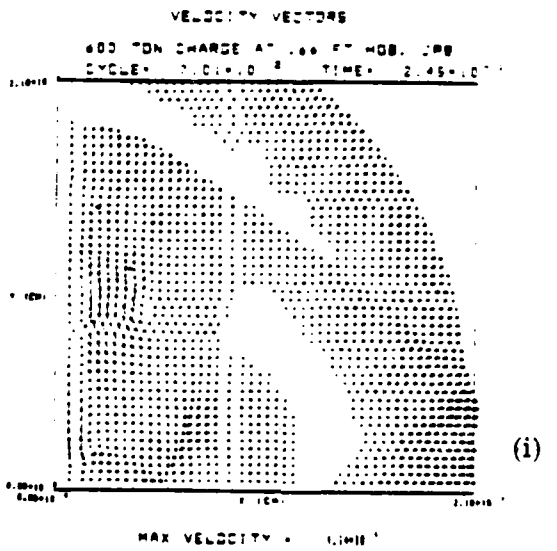
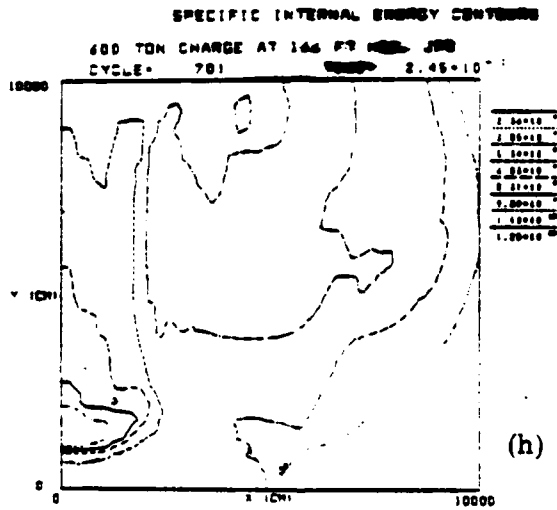
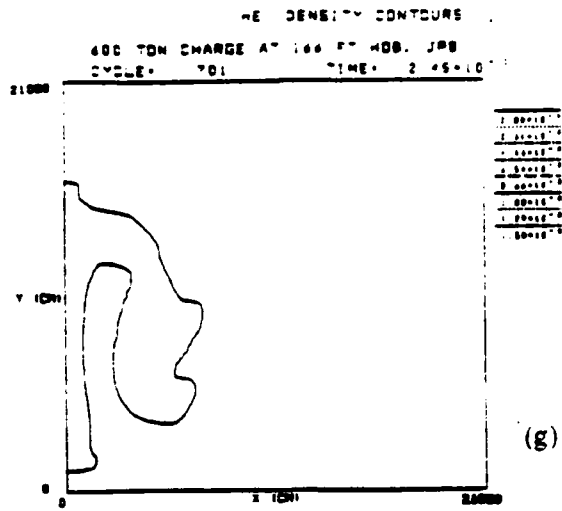
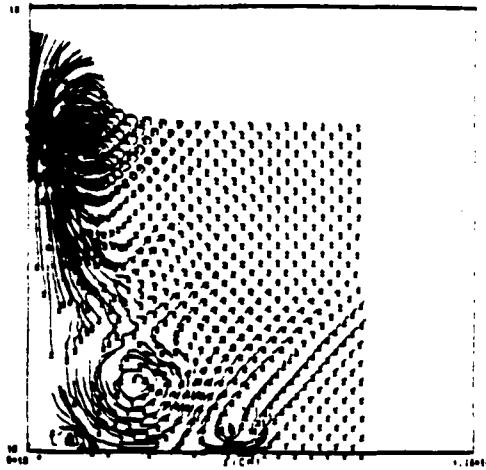


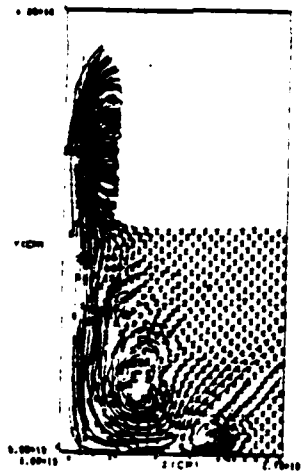
Figure 3 (Cont'd)

PARTICLE PATH PLOT  
400 TON DIRECT COURSE



(a)

PARTICLE PATH PLOT  
400 TON DIRECT COURSE



(b)

Figure 4

## REFERENCES

1. Boris, J. P. and Book, D. L. in Methods in Computational Physics, J. Killeen Ed., (Academic Press, NY, 1976), Vol. 16, p. 85.
2. Boris, J. P., "Flux-Corrected Transport Modules for Solving Generalized Continuity Equations", NRL Memo Report 3237 (1976). (AD-A023 891)
3. Kuhl, A. L., Fry, M. A., Picone, J. M., Book, D. L., Boris, J. P., "FCT Simulation of HOB AIRBLAST Phenomena", NRL Memo Report No. 4613, September 29, 1981. ADA107920
4. Young, T. R., "Table Look-Up: An Effective Tool on Vector Computers", Tenth Conf. on Numerical Simulation of Plasmas, San Diego, CA, January 4-6, 1983.
5. Miura, H. and Glass, I. I., "On the Passage of a Shock Wave through a Dust-Gas Layer", UTIAS Rept. No. 252 (1982). AD-A114-808.
6. Kuhl, A. L., "Comparisons of Shock Waves in Clear and Hot Dusty Air", Rept. RDA-TR-107006-011 (1978).

## ACKNOWLEDGMENT

This work was supported by the Defense Nuclear Agency under Subtask N99QAXAH/ MISSILE SYSTEMS/X-Ray Hardness, Work Unit # 00061, Work Unit Title "Cloud Calculations," and under Subtask Y99QAXSG/AIRBLAST AND THERMAL PREDICTIONS Work Unit #00057, Work Unit Title "Airblast Calculations."

APPENDIX E

POWER-SERIES SOLUTIONS OF THE GASDYNAMIC EQUATIONS  
FOR MACH REFLECTION OF A PLANAR SHOCK BY A WEDGE

REPORT DOCUMENTATION PAGE		READ INSTRUCTIONS BEFORE COMPLETING FORM
1. REPORT NUMBER	2. GOVT ACCESSION NO.	3. RECIPIENT'S CATALOG NUMBER
NRL Memorandum Report 5229		
4. TITLE (and Subtitle)	5. TYPE OF REPORT & PERIOD COVERED	
POWER-SERIES SOLUTIONS OF THE GASDYNAMIC EQUATIONS FOR MACH REFLECTION OF A PLANAR SHOCK BY A WEDGE	Interim report on a continuing NRL problem.	
	6. PERFORMING ORG. REPORT NUMBER	
7. AUTHOR(s)	8. CONTRACT OR GRANT NUMBER(s)	
D.L. Book, J.P. Boris, L.B. Bernstein,* and M.A. Fry**		
9. PERFORMING ORGANIZATION NAME AND ADDRESS		10. PROGRAM ELEMENT PROJECT TASK AREA & WORK UNIT NUMBERS
Naval Research Laboratory Washington, DC 20375		62715H; 44-0578-0-3
11. CONTROLLING OFFICE NAME AND ADDRESS		12. REPORT DATE
Defense Nuclear Agency Washington, DC 20305		December 2, 1983
		13. NUMBER OF PAGES
		29
14. MONITORING AGENCY NAME & ADDRESS (if different from Controlling Office)		15. SECURITY CLASS. (of this report)
		UNCLASSIFIED
		15a. DECLASSIFICATION/DOWNGRADING SCHEDULE
16. DISTRIBUTION STATEMENT (of this Report)		
Approved for public release; distribution unlimited.		
17. DISTRIBUTION STATEMENT (of the abstract entered in Block 20, if different from Report)		
18. SUPPLEMENTARY NOTES		
*Present address: Yale University, New Haven, CT 06520		
**Present address: Science Applications, Inc., McLean, VA 22102		
(Continues)		
19. KEY WORDS (Continue on reverse side if necessary and identify by block number)		
Mach stem	Power series	
Mach reflection	Contact surface	
Shock waves	Slip line	
Shock tubes	Triple point	
20. ABSTRACT (Continue on reverse side if necessary and identify by block number)		
<p>The self-similar solutions to the problem of a planar shock with Mach number <math>M_s</math> reflecting obliquely from a wedge with vertex angle <math>\theta_w</math> are obtained to arbitrary accuracy by expanding the fluid quantities in power series in the scaled variables <math>\xi = x/t</math>, <math>\eta = y/t</math>. For single Mach reflection, there are four distinct regions: (a) the ambient gas ahead of the incident shock; (b) the gas behind the incident shock and outside the reflected (bow) shock; (c) the region bounded by the Mach stem, the wedge, and the contact surface (slip line) extending from the triple point; and (d) the doubly</p>		
(Continues)		

## 18. SUPPLEMENTARY NOTES (Continued)

This work was supported by the Defense Nuclear Agency under Subtask Y99QAXSG, work unit 00057 and work unit title "Airblast Calculations."

## 20. ABSTRACT (Continued)

shocked medium bounded by the contact surface, wedge, and reflected shock. In region (b) the solution is known immediately in terms of  $M_w$ ,  $\theta_w$ , and the conditions in (a). The shapes of the Mach stem, contact surface and bow shock are expressed parametrically as  $\xi = F(s)$ ,  $\eta = G(s)$ . Then  $\rho_c$ ,  $u_c$ ,  $v_c$ ,  $p_c$ , and  $\rho_d$ ,  $u_d$ ,  $v_d$ ,  $p_d$  are obtained by expanding variables in double power series. e.g.,

$$\rho_c(\xi, \eta) = \sum_{i,j} \rho_c^{ij} \xi^i \eta^j,$$

substituting in the ideal fluid equations, and equating coefficients of like powers through some order  $N = \max(i+j)$ . The resulting algebraic equations are solved subject to the additional relations obtained by applying the reflection conditions on the wedge, together with the jump conditions on the boundaries ac and bd, approximated by power series expansions of the F and G functions. Since all these equations are nonlinear, solutions are obtained by iteration with N increasing until convergence is obtained. The Ben-Dor equation for the fluid quantities in regions c, d at the triple point is used to give initial values. Because variation within each region is smooth, effectively exact descriptions of most features of interest can be obtained using series with  $\lesssim 20$  terms. There are thus  $\lesssim 200$  quantities in the discretization of the problem, compared with  $\gtrsim 10^4$  in a conventional finite-difference treatment. The method generalizes readily to complex and double Mach reflections.

## CONTENTS

INTRODUCTION .....	1
DERIVATION OF EQUATIONS .....	6
SOLUTION OF EQUATIONS .....	15
CONCLUSION .....	16
REFERENCES .....	17
ACKNOWLEDGMENTS .....	17

POWER-SERIES SOLUTIONS OF THE GASDYNAMIC EQUATIONS FOR MACH REFLECTION OF A  
PLANAR SHOCK BY A WEDGE

David L. Book and Jay P. Boris

Naval Research Laboratory, Washington, D. C. 20375

Ira B. Bernstein

Yale University, New Haven, Conn. 06520

Mark A. Fry

Science Applications, Inc., McLean, Virginia 22102

INTRODUCTION

The problem of a planar shock reflecting from an oblique surface goes back over a hundred years to Ernst Mach. Although this problem is important in its own right, much of the interest in it arises because of the need for better understanding of Mach reflection in more complicated situations. The field has been the object of particular interest during the last thirty years; the experimental and theoretical research carried out during this period have been reviewed by Ben-Dor.<sup>1</sup>

A constant planar shock propagating into a uniform ambient gas gives rise in the absence of reflection to a second medium with uniform thermodynamic properties in the region behind the shock. If it propagates in a shock

---

Manuscript approved September 13, 1983.

tube whose walls are not parallel to the direction of propagation (because a wedge has been inserted along the side), a reflected shock wave propagates back into the interior of the shock tube. When the wedge angle is large, so that the primary shock is incident nearly normally on it, the reflected shock is also planar and no other gasdynamic discontinuities appear near the reflection point. As the wedge angle decreases, so that the incident shock becomes more and more nearly glancing, it becomes impossible for a fluid particle to traverse both incident and reflected shocks and still "turn the corner" enough to end up moving parallel to the wedge surface. At least one additional shock (the Mach stem) must appear (Fig. 1), intersecting the others at a so-called triple point. Because some of the material in the zone between the Mach stem and the reflected wave has been shocked once and some twice, another gasdynamic discontinuity (a contact surface) must also extend from the triple point into this region, terminating somewhere on the wedge surface. The reflected shock may terminate at the corner of the wedge (attached shock), or upstream from this point (detached shock), or may run into a second triple point between the first one and the corner (double Mach reflection). The latter case occurs in general for smaller wedge angles than does single Mach reflection; an intermediate case (complex Mach reflection) is also observed.

One would like to derive a theoretical description of Mach reflection which would complement the experimental results and address some of the questions the latter leave unanswered, such as the structure of the contact surface near the wedge surface, and whether a "triple Mach" regime exists. An analytical solution is out of the question, though pieces of the problem (e.g., the flow in the neighborhood of the triple point<sup>1</sup>) can be solved. Recourse must therefore be had to numerical methods.

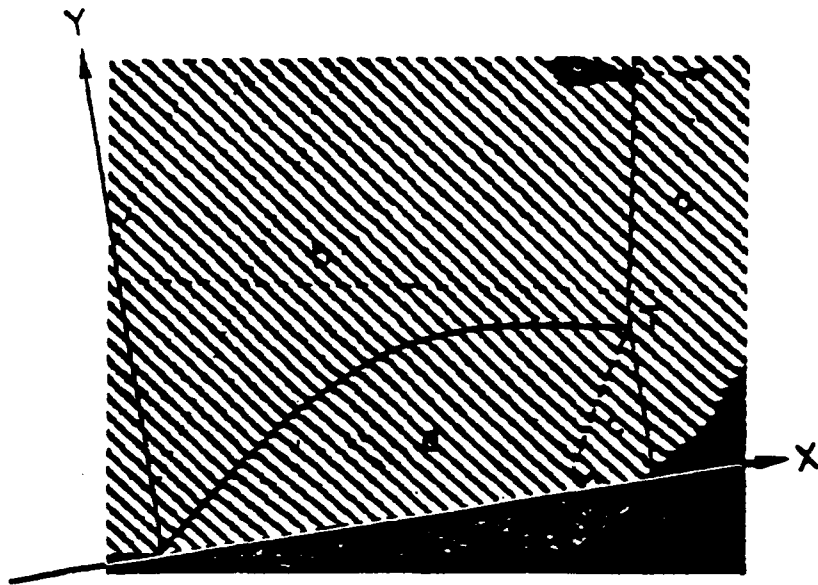


Figure 1. Interferogram of single Mach reflection in  $N_2$  ( $M_s = 4.72$ ,  $\theta_w = 10^\circ$ ,  $P_a = 15$  torr) after Ben-Dor<sup>1</sup>, with X and Y axes and gasdynamic discontinuities drawn in, and regions labeled with a, b, c, d.

Straightforward differencing of the fluid equations (using either an ideal or realistic equation of state) has been carried out with considerable success<sup>1,2</sup>. A rectilinear Eulerian mesh with ~100 - 200 zones along each axis, possibly varying in size as a function of position to improve resolution near the Mach stem, is used. The conditions ahead of and behind the incident shock are used as boundary conditions, along with a reflection condition on the wedge. State-of-the art shock capturing techniques such as Flux-Corrected Transport (FCT)<sup>3</sup> resolve the envelope (reflected) waveform accurately and permit almost all the other gasdynamic discontinuities in the problem to be distinguished (Fig. 2). To date, however, such numerical solutions have not surpassed experimental interferometric data in accuracy, nor have they succeeded in answering any of the outstanding questions associated with Mach reflection.

Moreover, such calculations leave a distinct impression of brute force. Advancing the four fluid equation  $10^3 - 10^4$  timesteps on  $10^4$  or more zones seems profligate, particularly in view of the smoothness of most of the gasdynamic discontinuities and the gentle variation of the fluid quantities in the regions they bound. In much of the domain of the calculation the solution is known a priori and does not change in time.

Furthermore, the desired solution is actually self-similar. In the scaled variables  $\xi = x/t$ ,  $\eta = y/t$ , where  $t$  is time and the origin of the coordinate system is fixed at the wedge corner, the observed wave forms are stationary. It is thus natural to seek a solution to the ideal fluid equations in terms of these similarity variables.

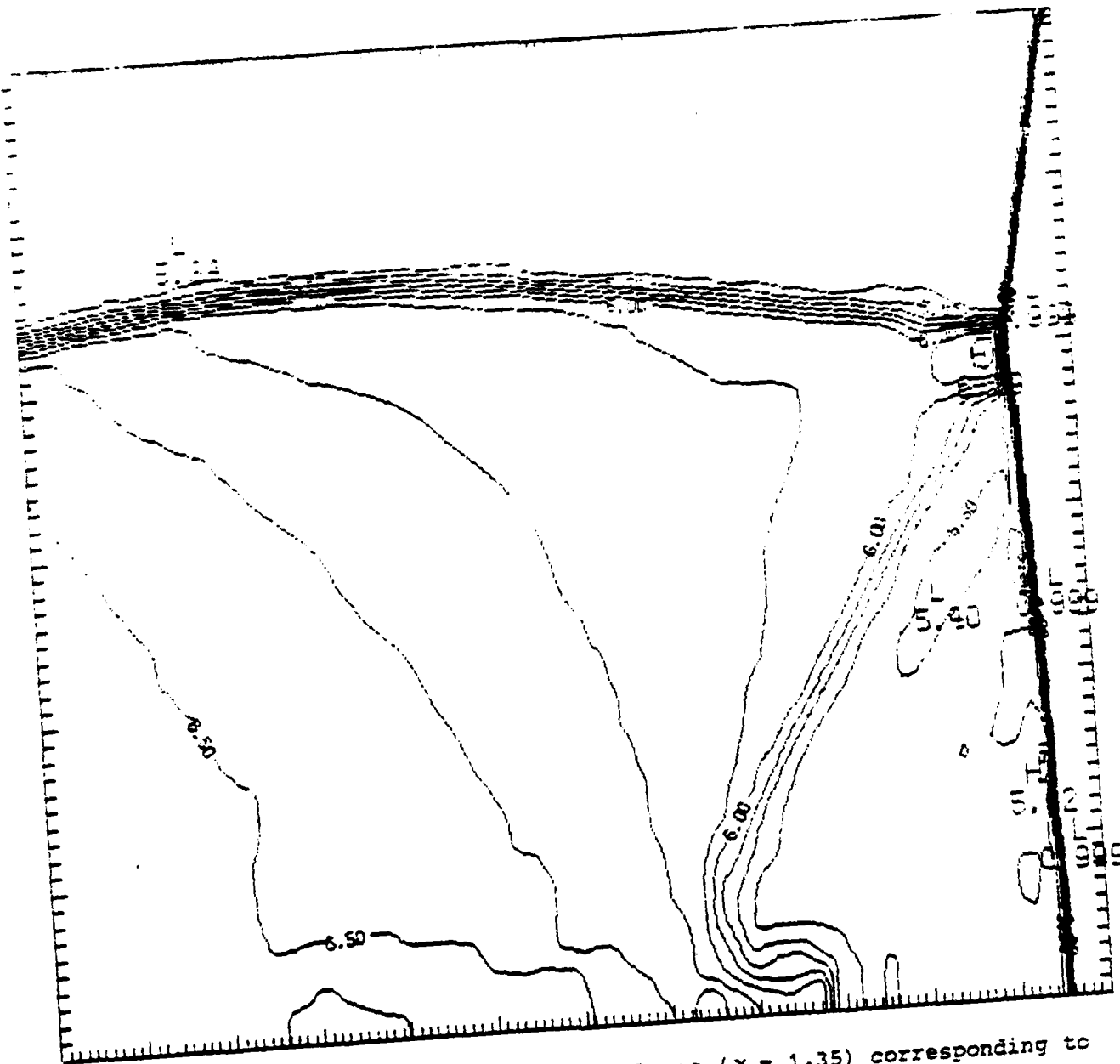


Figure 2. Triple-point region in ideal gas ( $\gamma = 1.35$ ) corresponding to Fig. 1, calculated using FCT code FAST2D.

In the present paper we treat the shock-on-wedge problem by expanding the fluid variables and the functional forms of the boundaries in power series in  $\xi$  and  $\eta$ . The expansion coefficients are found by imposing the boundary conditions (Rankine-Hugoniot conditions on the shock, perfect reflection on the wedge surface).

Numerous fluid dynamics problems have been solved by power series techniques, as described by Van Dyke.<sup>4</sup> Here we follow the general approach he advocates: first do the lowest-order terms "by hand," then afterward automate the procedure, finally using sophisticated mathematical techniques to find the limiting values of critical numbers (e.g., boundaries between two reflection regimes). Unlike most of the problems described by Van Dyke, the algebraic equations determining the power series coefficients here are highly nonlinear and need to be solved by iteration; the proper iteration scheme is not obvious, but must be found by experimentation.

In the following section we derive the equations to be solved. The next section describes the iteration procedure, the program implementing it, and the display. The final section summarizes our conclusions and discusses extension of the calculation to higher order and to the more complicated Mach reflection cases.

#### DERIVATION OF EQUATIONS

In what follows we use the label "a" for quantities in the ambient gas (ahead of the incident shock); "b" behind the incident shock; "c" between the contact surface and the Mach stem; and "d" for the doubly shocked region between the reflected shock and the contact surface. Surfaces of gasdynamic discontinuities are labelled by the two regions they separate, e.g. "cd" for the contact surface. The triple point is labeled by the subscript "T," and the origin is at the point of attachment (the wedge corner).

In terms of the similarity variables  $\xi$ ,  $\eta$ , the fluid equations become

$$(u-\xi) \frac{\partial \rho}{\partial \xi} + (v-\eta) \frac{\partial \rho}{\partial \eta} - \rho \left( \frac{\partial u}{\partial \xi} + \frac{\partial v}{\partial \eta} \right) = 0; \quad (1)$$

$$\rho \left[ (u-\xi) \frac{\partial u}{\partial \xi} + (v-\eta) \frac{\partial u}{\partial \eta} \right] + \frac{\partial \rho}{\partial \xi} = 0; \quad (2)$$

$$\rho \left[ (u-\xi) \frac{\partial v}{\partial \xi} + (v-\eta) \frac{\partial v}{\partial \eta} \right] + \frac{\partial \rho}{\partial \eta} = 0; \quad (3)$$

$$(u-\xi) \frac{\partial p}{\partial \xi} + (v-\eta) \frac{\partial p}{\partial \eta} + \gamma p \left( \frac{\partial u}{\partial \xi} + \frac{\partial v}{\partial \eta} \right) = 0, \quad (4)$$

where  $\gamma$  is the adiabatic index.

If we define dimensionless variables by

$$X = \xi/c, \quad Y = \eta/c; \quad (5)$$

$$U = (u-\xi)c^{-1}, \quad V = (v-\eta)c^{-1}, \quad (6)$$

$$R = \rho/\rho_a, \quad P = p/p_a, \quad (7)$$

where

$$c^2 = p_a/\rho_a, \quad (8)$$

then the fluid equations become

$$U \frac{\partial R}{\partial X} + V \frac{\partial R}{\partial Y} + R \left( \frac{\partial U}{\partial X} + \frac{\partial V}{\partial Y} + 2 \right) = 0; \quad (9)$$

$$R \left( U \frac{\partial U}{\partial X} + V \frac{\partial U}{\partial Y} + U \right) + \frac{\partial P}{\partial X} = 0; \quad (10)$$

$$R \left( U \frac{\partial V}{\partial X} + V \frac{\partial V}{\partial Y} + V \right) + \frac{\partial P}{\partial Y} = 0; \quad (11)$$

$$U \frac{\partial P}{\partial X} + V \frac{\partial P}{\partial Y} + \gamma P \left( \frac{\partial U}{\partial X} + \frac{\partial V}{\partial Y} + 2 \right) = 0. \quad (12)$$

In each of regions c and d we expand R, U, V, P in double power series,

$$R(X, Y) = R_{00} + R_{10}X + R_{01}Y + R_{20}X^2 + R_{11}XY + R_{02}Y^2 + \quad (13)$$

$$+ R_{30}X^3 + R_{21}X^2Y + R_{12}XY^2 + R_{03}Y^3 + \dots$$

$$U(X, Y) = U_{00} + U_{10}X + U_{01}Y + U_{20}X^2 + U_{11}XY + U_{02}Y^2 + \quad (14)$$

$$+ U_{30}X^3 + U_{21}X^2Y + U_{12}XY^2 + U_{03}Y^3 + \dots$$

$$V(X, Y) = V_{00} + V_{10}X + V_{01}Y + V_{20}X^2 + V_{11}XY + V_{02}Y^2 + \quad (15)$$

$$+ V_{30}X^3 + V_{21}X^2Y + V_{12}XY^2 + V_{03}Y^3 + \dots$$

$$P(X, Y) = P_{00} + P_{10}X + P_{01}Y + P_{20}X^2 + P_{11}XY + P_{02}Y^2 + \quad (16)$$

$$+ P_{30}X^3 + P_{21}X^2Y + P_{12}XY^2 + P_{03}Y^3 + \dots$$

To apply the reflection boundary condition, we set

$$\frac{\partial p}{\partial n} = \frac{\partial u}{\partial n} = \frac{\partial v}{\partial n} = v = 0 \quad (17)$$

at  $\eta = 0$  for all  $\xi$ . It follows that we must have

$$R_{01} = R_{11} = R_{21} = R_{31} = \dots = 0; \quad (18)$$

$$U_{01} = U_{11} = U_{21} = U_{31} = \dots = 0; \quad (19)$$

$$P_{01} = P_{11} = P_{21} = P_{31} = \dots = 0; \quad (20)$$

and

$$V_{00} = V_{10} = V_{20} = V_{30} = \dots = 0. \quad (21)$$

To proceed further, we substitute Eqs. (13)-(16) in Eqs. (9)-(12) and collect terms of like powers  $X^i Y^j$ , equating their coefficients to zero order by order. The task of doing this by conventional methods rapidly becomes hopeless, but it can readily be automated. To see what is going on in the lowest orders of our "hand" calculation, we expand using MACSYMA, the symbolic manipulation program developed at the Mathlab of MIT. This works up to about order  $N = 6$ , where we define the order of the expansion by  $N = \max(i+j)$ . Beyond that point storage limitations make it necessary to use "tricks," and eventually terminate the process entirely.

When this is done, certain patterns emerge. We find that we must have

$$V_{02} = V_{12} = V_{22} = \dots = 0, \quad (22)$$

$$P_{03} = P_{13} = P_{23} = \dots = 0. \quad (23)$$

Some of the equations then vanish identically. In each of regions c and d there are more variables than nontrivial equations, as shown by the following table:

Order	<u>Equations</u>					<u>Variables</u>				
	R	U	V	P	Total	R	U	V	P	Total
0	1	1	0	1	3	2	2	1	2	7
1	1	1	1	1	4	2	2	1	2	7
2	2	2	1	2	7	3	3	2	2	10
3	3	3	2	3	11	4	4	3	3	14
4	4	4	3	4	15	5	5	4	4	18
5	5	5	4	5	19	6	6	5	5	22
.										
.										
.										

Table 1

Table 1 shows that in each region there are three more unknowns than equations in each order, except for  $N = 0$ , where the number is four. The additional equations are supplied by the jump conditions, imposed on surfaces ac and bd for regions c and d, respectively.

If we represent a shock boundary parametrically by  $X = F(s)$ ,  $Y = G(s)$ , then the Rankine-Hugoniot conditions become

$$X' (U - \bar{U}) + Y' (V - \bar{V}) = 0; \quad (24)$$

$$Y' (R U - \bar{R} \bar{U}) = X' (R V - \bar{R} \bar{V}); \quad (25)$$

$$P + R (U^2 + V^2) = \bar{P} + \bar{R} (\bar{U}^2 + \bar{V}^2); \quad (26)$$

$$U^2 + V^2 + \frac{2Y\bar{P}}{Y-1} = \bar{U}^2 + \bar{V}^2 + \frac{2Y\bar{P}}{Y-1}, \quad (27)$$

while on a contact surface

$$P = \bar{P}; \quad (28)$$

$$Y' U = X' V; \quad (29)$$

$$Y' \bar{U} = X' \bar{V}. \quad (30)$$

Here the variables in front of and behind the discontinuity are denoted by unbarred and barred symbols, respectively.

We know that  $ac$  is nearly a straight line normal to the wall, so the representation

$$X = X_0 + X_1 Y + X_2 Y^2 + X_3 Y^3 + \dots \quad (31)$$

is valid. Substituting Eq. (31) and the ambient conditions  $u^a = v^a = 0$  in Eq. (24), the condition for continuity of parallel velocities at  $ac$ , which takes the form

$$X' (U^c - U^a) + V^c - V^a = 0, \quad (32)$$

we find

$$X_1 = 0; \quad (33)$$

$$X_2 = \frac{1 + V_{01}^c + V_{11}^c X_0 + V_{21}^c X_0^2 + \dots}{2 (X_0 + U_{00}^c + U_{10}^c X_0 + U_{20}^c X_0^2 + \dots)}, \quad (34)$$

etc. When the coefficients of Eq. (31) are known, substitution of Eq. (31) in Eqs. (25)-(27) (with  $Y' = 1$ ) yields three conditions in each order on  $R_{ij}^c, U_{ij}^c, v_{ij}^c, P_{ij}^c$ .

Analogously, we write the equation for the reflected shock bd as

$$Y = Y_1 X + Y_2 X^2 + Y_3 X^3 + \dots \quad (35)$$

Substitution in the condition for continuity of the parallel velocities at bd,

$$U^d - U^b + Y' (V^d - V^b) = 0, \quad (36)$$

yields

$$y_1 = - \frac{u^b - u_{c0}^d}{v^b} ; \quad (37)$$

$$y_2 = \frac{(v_{01}^d + 1) y_1^2 + u_{10}^d + 1}{2v^b} , \quad (38)$$

$$y_3 = \frac{3(v_{01}^d + 1) y_1 y_2 + (v_{11}^d + u_{02}^d) y_1^2 + u_{20}^d}{3v^b} , \quad (39)$$

etc. (Note that  $u^b$  and  $v^b$ , like  $u^a$  and  $v^a$ , are constants, whereas  $u^b$ ,  $v^b$ ,  $u^a$ ,  $v^a$  are not.) Substitution of Eq. (35) in Eqs. (25)-(27) with  $X' = 1$  then yields three conditions per order on the "d" variables.

At this point we need three more conditions: two for the remaining variables in order zero, and another to determine  $X_0$ . For this purpose we use Eqs. (28)-(30). Note that to apply these conditions everywhere on  $cd$  would overdetermine the system. This is equivalent to asserting the impossibility of continuing the solution across  $ab$  from  $a$  to  $b$ , across  $ac$  from  $a$  to  $c$ , across  $bd$  from  $b$  to  $d$ , and then across  $cd$  from  $c$  back to  $d$ , where it is already known. The only freedom we have is to impose Eqs. (28)-(30) at the triple point.

First we define  $X_T, Y_T$  by setting

$$Y_T = Y_1 X_T + Y_2 X_T^2 + Y_3 X_T^3 + \dots \quad (40)$$

$$X_T = X_0 + X_1 Y_T + X_2 Y_T^2 + X_3 Y_T^3 + \dots \quad (41)$$

Then we require

$$P^C(X_T, Y_T) = P^d(X_T, Y_T); \quad (42)$$

$$U^C(X_T, Y_T) \Delta Y_T = V^C(X_T, Y_T) \Delta X_T; \quad (43)$$

$$U^d(X_T, Y_T) \Delta Y_T = V^d(X_T, Y_T) \Delta X_T, \quad (44)$$

where

$$0 = P^C(X, Y) - P^d(X, Y) = P^C(X_T, Y_T) - P^d(X_T, Y_T) \quad (45)$$

$$+ \Delta X_T \left( \frac{\partial P^C}{\partial X} - \frac{\partial P^d}{\partial X} \right)_T + \Delta Y_T \left( \frac{\partial P^C}{\partial Y} - \frac{\partial P^d}{\partial Y} \right)_T$$

determines the ratio  $\Delta X_T / \Delta Y_T$ .

For our trial calculation we work to order  $N = 5$ . Including the quantities which vanish identically, we then have 183 equations in 183 unknowns, which are to be solved simultaneously.

#### SOLUTION OF EQUATIONS

The solution is obtained by iteration. Several points are important in the design of a satisfactory iteration scheme:

- (i) Good values of the quantities  $X_0$ ,  $X_T$ ,  $Y_T$ , etc., can be obtained from the experimental data (Fig. 1) and used as initial guesses.
- (ii) The system can be made quasilinear if we solve order by order, starting with  $N = 0$ , and using in any given order the previously obtained values of all variables not being solved for in that order.
- (iii) To reduce the effect of possible instability in parts of the scheme, all variables are updated using some form of (under)relaxation, e.g.,  
new value = old value + relaxation factor  $\times$  corrections.

The current version of the code works as follows:

- (i) For  $N = 0$ , use the X- and Y- independent terms of Eqs. (9)-(12), together with the zeroth-order form of Eqs. (25)-(27) and Eq. (43) to update  $R_{00}^c$ ,  $R_{10}^c$ ,  $U_{00}^c$ ,  $U_{10}^c$ ,  $V_{01}^c$ ,  $P_{00}^c$ ,  $P_{10}^c$ ;
- (ii) Do the same thing [using Eq. (44) instead of (43)] for  $R_{00}^d$ ,  
..,  $P_{10}^d$ ;
- (iii) Solve Eqs. (9)-(12) and Eqs. (25)-(27) on ac order by order for  $N = 1$  to 5 to obtain the region-c variables;
- (iv) Solve Eqs. (9)-(12) and Eqs. (24)-(27) on bd order by order for  $N = 1$  to 5 to obtain the region-d variables plus  $Y_{N+1}$ ;
- (v) Iterate Eqs. (40)-(42) together with the successive orders of Eq. (32) [e.g., Eq. (34) for  $X_2$ ] to solve for  $X_T$ ,  $Y_T$ , and  $X_i$ ,  $i = 0, 1, \dots, 6$ . (To a good approximation,  $X_i = 0$  for all  $i \neq 0, 2$ .)

This scheme is repeated until no further change (to some preset tolerance) in the variables occurs. The program, written in Fortran, runs on a VAX 11/780 at about one second per iteration.

Results are most conveniently displayed as contour plots in pressure (or density). Although it is possible to drive the plotting pen directly using the exact formula  $P(X,Y)$ , it is easier to declare a very large array (e.g.,  $500 \times 500$ ), fill it with pressures calculated at every  $X, Y$ , and use a standard contour plotting package on this.

#### CONCLUSION

The program described above is still under development, and no results have yet been generated. For this sample problem, it seems straightforward to carry the method to a successful solution. We have encountered, and apparently overcome, two types of difficulties: determining the formulation for the problem, and solving the resulting set of equations. Only if both stages are handled correctly will useful answers result. There remains the (programming) task of automating the solution, so as to work to arbitrarily high order  $N$ . This is of interest chiefly in connection with studying the behavior of the roll-up in the contact surface.

Finally, extension to other forms of Mach reflection is of interest. Attached double (or triple) Mach reflection presents no problem in principle, and can be handled using the techniques described here. Complex Mach reflection and detached shocks are less clear. At present we do not know how to formulate the problem in either situation so as to make it well-posed. This will be addressed in future work.

## REFERENCES

1. Ben-Dor, G., "Regions and Transitions of Nonstationary Oblique Shock-Wave Diffractions in Perfect and Imperfect Gases," UTIAS Rept. No. 232 (1978), AFOSR-TR-0063 AD-A064-967.
2. Book, D., Boris, J., Kuhl, A., Oran, E., Picone, M., and Zalesak, S., "Simulation of Complex Shock reflections from Wedges in Inert and Reactive Gaseous Mixtures," Proc. 7th International Conf. Numer. Methods in Fluid Dynamics (Springer-Verlag, Berlin, 1981), p. 84.
3. Boris, J.P., and Book, D.L., in Methods in Computational Physics, Vol. 16, J. Killeen, Ed. (Academic Press, 1975), p. 85.
4. Van Dyke, M., "Computer Extension of Perturbation Series in Fluid Mechanics," SIAM J. Appl. Math 28, 720 (1975).

## ACKNOWLEDGMENTS

This work was supported by the Defense Nuclear Agency under Subtask Y99QAXSG/Airblast and Thermal Predictions, Work Unit #00057, Work Unit Title "Airblast Calculations."

NUCLEAR AND NON-NUCLEAR  
AIRBLAST EFFECTS  
FINAL REPORT NO. SAI-84/1529  
MARK FRY  
February 14, 1984



**SCIENCE APPLICATIONS, INC.**

Post Office Box 1303, 1710 Goodridge Drive, McLean, Virginia 22102, (703) 821-4300

END

FILMED

4-84

DTIC